

Hypatia Colloquium

EARLY CAREER
ASTRONOMER SERIES
AT ESO 2022



PROCEEDINGS

G. Beccari
H. M. J. Boffin
Editors

Contents

Xavier Barcons - <i>Preface</i>	5
Giacomo Beccari and Henri M.J. Boffin - <i>Introduction</i>	6

COSMOLOGY

Leindert Boogaard - <i>Cold gas in distant galaxies</i>	10
Nicola Borghi - <i>Toward an independent reconstruction of the expansion history of the Universe</i>	12
Andrea Botteon - <i>The most giant radio structures in the Universe</i>	14
Giovanni Granata - <i>Improved strong lensing modelling of galaxy clusters using the Fundamental Plane: detailed mapping of the baryonic and dark matter mass distribution of Abell S1063</i>	16
Carlos Gómez-Guijarro - <i>GOODS-ALMA 2.0: Understanding the role of compact star formation in galaxy evolution</i>	18
Kasper Elm Heintz - <i>Measuring the H₁ gas mass of galaxies in the early universe with cosmic explosions</i>	20
Paulina Karczmarek - <i>The impact of classical Cepheids' companions on the extragalactic distance scale</i>	22
Sofía Rojas-Ruiz - <i>The Role of Powerful Radio Jets in the Host Galaxy of a Quasar in the First Gyr of the Universe</i>	24
Laura Sommovigo - <i>The dust temperature REBELS</i>	26

GALAXIES AND GALACTIC NUCLEI

Riccardo Arcodia - <i>X-ray blasts from awakening massive black holes</i>	30
Stefania Barsanti - <i>An observed link between spin-filament alignment flips and bulge formation</i>	32
Tirna Deb - <i>An H₁ story of galaxies in A2626 and beyond</i>	34
Victoria A. Fawcett - <i>Why is colour special? Fundamental differences between red and blue quasars</i>	36
Aishwarya Girdhar - <i>Quasar Feedback Survey – the impact of jets and multi-phase outflows on their host galaxies</i>	38
Luca Ighina - <i>The Impact of the CMB on high-<i>z</i> AGNs jets</i>	40
Geray S. Karademir - <i>The Galaxy Luminosity Function via Clustering Based Redshift Inference: can we find the bottom of the galaxy population?</i>	42
Nandini Sahu - <i>Non-linear (Black Hole Mass)—Spheroid Scaling Laws & The Role of Galaxy Morphology</i>	44

INTERSTELLAR MEDIUM, STAR FORMATION and PLANETARY SYSTEMS

Victor Almindros-Abad - <i>Is brown dwarf formation environment-dependent? A case study in NGC 2244</i>	48
Stefano Bellotti - <i>Mitigating stellar activity using line selections for Least-Squares Deconvolution</i>	50
Alice S. Booth - <i>Sublimating Ices Feeding Forming Planets</i>	52
Emma Bordier - <i>The formation of massive close binaries: is the migration scenario viable?</i>	54
Rubén Fedriani - <i>Revealing a clustered region of massive star formation through NIR jets using VLT instruments</i>	56
Eleonora Fiorellino - <i>The Mass of Young Stars likes to play Hide & Seek</i>	58
Clémence Fontanive - <i>Strength In Numbers: How Do Stellar Companions Affect Giant Planet Formation?</i>	60

Chiara Eleonora Scardoni - <i>The effect of the streaming instability on protoplanetary disc dust emission</i>	62
Vito Squicciarini - <i>Can a massive star possess its own planetary system?</i>	64
Sebastiano D. von Fellenberg - <i>Young Stars in the Galactic Center</i>	66

STELLAR POPULATIONS AND EVOLUTION, AND TECHNOLOGY

Kevin Barjot - <i>First light of the FIRST visible fibered interferometer upgrade at the Subaru telescope</i>	70
Emma R. Beasor - <i>The impact of realistic red supergiant mass-loss on stellar evolution</i>	72
Cristobal Bordiu - <i>A molecular window into the mass loss history of Luminous Blue Variables</i>	74
Alfred Castro-Ginard - <i>Gaia keeps on delivering: expanding the open cluster population with EDR3</i>	76
Danny Horta - <i>Unveiling the mass assembly history of the Milky Way via its stellar halo</i>	78
Kateryna Kravchenko - <i>Tomography of evolved star atmospheres</i>	80
Linda Lombardo - <i>A close look at young intermediate mass giant stars: clues of rotation and mixing</i>	82
Ramya M Anche - <i>Determination of polarimetric capabilities of the Thirty Meter Telescope</i>	84
Feliciano Sapio - <i>General Relativity with the two Galileo satellites DORESA and MILENA</i>	86
Paulina Sowicka - <i>GW Vir instability strip in the light of new observations of PG 1159 stars</i>	88
Hypatia	90

Preface



Dear colleagues,

I am among those who think that the COVID-19 pandemic brought very little good to humankind: death, suffering and reduced opportunities to remain social. But novel and good things were also developed in the last two years out of neces-

sity, and the ESO Hypatia colloquium is a shiny example. This is the second year that my colleagues Giacomo Beccari and Henri Boffin organise these colloquia, aiming at having a selection of brilliant early career scientists presenting on-line their research work to colleagues and

potentially interested employers. This was devised as an initiative to replace the opportunities for these early career colleagues to show their science at conferences or even at prospective new work places. But the reality in the new phases of COVID-19 is that the Hypatia colloquia have become a much valued and complementary tool. I honestly believe that this initiative has a long life ahead, if only by looking at the quality and excitement of the presentations

Having new initiatives requires a lot of thinking, bringing them to reality needs a lot of effort. Sustaining these initiatives needs in addition a lot of conviction and very strong commitment. This is what Giacomo and Henri have achieved. Thank you so much for this and long life to the Hypatia colloquia.

Garching, 21 September 2022

Xavier Barcons
ESO Director-General

Introduction

Giacomo Beccari and Henri M.J. Boffin

European Southern Observatory, Karl-Schwarzschild-Strasse 2, 85748 Garching bei München

The Office for Science (OfS) in Garching (Germany) at the European Southern Observatory (ESO) organised the second edition of the Hypatia Colloquium Series. Announced for the first time in November 2020 [1], the Hypatia colloquia foresees a series of 20 min talks given by early career astronomers (up to 3 years from the PhD). In a few words, the Hypatia Colloquium Series is meant as a channel to allow excellent young researchers to show the results of their scientific work to a broad audience.

The call for applications for the 2022 Series was released in November 2021. ESO received almost 200 applications out of which an ad-hoc committee, composed by Fellows and staff astronomers both from ESO Germany and Chile, selected the 44 speakers of the new Series. The program was released in January 2022 and is available on the Hypatia pages*.

The programme page is meant as a resource to discover the scientific profile of the speakers. By clicking on the title of the talk, the visitor of the page has access to the abstract and the Curriculum Vitae of the speaker. Moreover, for each talk, we add a link to the YouTube video where the talk is recorded.

As done in the Hypatia 2021 book [1], we show on Figure 1 the distribution in terms of gender and year of PhD of the speakers of the Hypatia 2022 Series. We achieved a solid balance in terms of both gender and seniority of the speakers. Moreover, as can be appreciated in this booklet, the Series offers a fair coverage of most of the scientific research topics of modern astrophysics.

The Hypatia 2022 Series

The talks were scheduled on Tuesdays at 3pm Garching (Germany) time from January 18 to June 22, 2022 (except one week, when there was the ESO ASTRO2022 conference [2]). The format of this Series foresees two 20 min-long talks, each followed by questions and discussion. Most of the seminars were co-chaired by an ESO Student and an ESO Fellow.

The seminars were entirely hosted online using the video conferencing tool Zoom and live-streamed on the Hypatia Colloquium YouTube channel†. Attendees could register to the Series using a web form. Registered participants were able to attend the seminars and interact with the speakers via the Zoom meeting. Alternatively, the community was invited to attend the live events on the dedicated YouTube page. All YouTube attendees could ask questions during the live event using the Live Chat on YouTube or using a web form or by email if they preferred to not have a YouTube account. All the video recordings of the live events, including the content of the live chat, are available on the “Hypatia Colloquium 2022” playlist

accessible on the Hypatia YouTube page.

We show on Figure 2 the analytics of the Hypatia YouTube channel. In particular, the plot shows the number of views of the videos of the talks as a function of time for the year 2022. The numerous peaks of the views’ distribution corresponds to the time when the talks were broadcast live on YouTube. While the number of view does not exactly indicates the number of attendees of each event, on average each live event was followed by a total of 20 to 40 participants, with peaks of more than 60 participants.

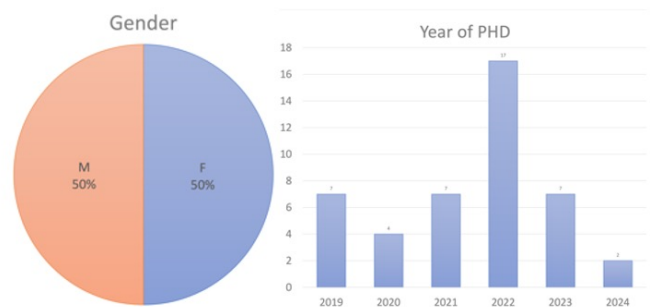


Figure 1: Distribution in terms of gender and (expected) year of PhD completion (left and right plots, respectively) of the speakers of the Hypatia Colloquium Series.

The return to in-person events

We noted that the number of live attendees dropped towards the end of the series in June 2022. Starting with the months of March/April 2022, we witnessed a slow but constant return to the “normality” of our social and professional life. The number of congresses and workshops foreseeing an in-person participation flourished in 2022. Understandably, the drive to re-establish a contact with the astronomical community and colleagues via in-person meetings has affected the participation to online events. This might be particularly true for the youngest generation of astronomers who lived a very significant fraction of their young career under the severe circumstances imposed by the restrictions due to the COVID19 pandemic. Despite this, we are sure that with the Hypatia series, ESO has achieved the important goal to create a friendly and professional platform to allow the young generation of astronomers to show their scientific results. The booklet of proceedings and the collection of videos represent a snapshot of the astronomical research done today and a solid legacy for a predictably bright future of the speakers.

*<https://www.eso.org/sci/meetings/garching/hypatia-colloquium/program2022.html>

†<https://www.youtube.com/c/HypatiaColloquium>

Your videos got 3,878 views in 2022

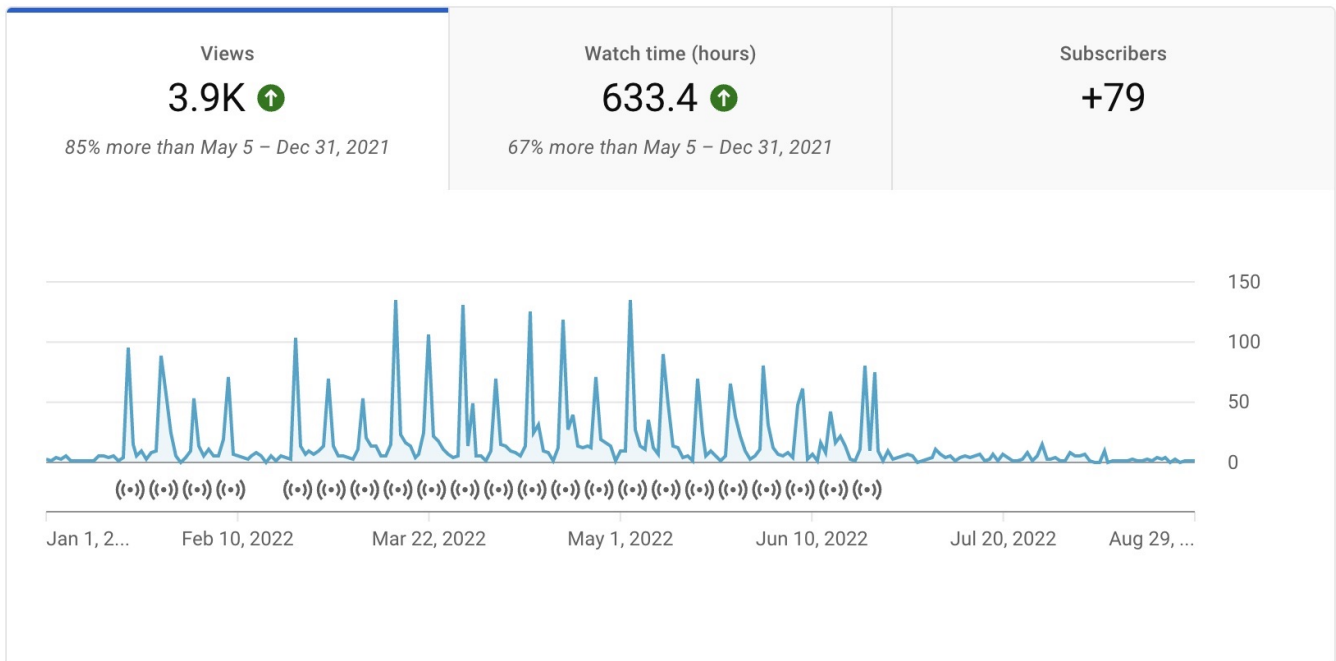


Figure 2: Snapshot of the Hypatia YouTube channel analytics for the year 2022. The peaks of views correspond to the time when each event was broadcast live.

Supporting early career astronomers sustainably

Among its top values, ESO strives for excellence through innovation and to provide outstanding services to the community while fostering diversity and inclusion[‡]. In this context the ESO OfS maintains a number of programmes (e.g., Fellowship, Studentship, Early Career Visitor Programme) whose primary goal is to offer to early career scientists the opportunity to perform astronomical research in an enjoyable, professional and international environment. Along the same line, the Hypatia Colloquium Series was specifically designed to offer further support to the researchers at their early stages during a particularly challenging time (the COVID19 pandemic). In this context, online series of seminars, such as the Hypatia Colloquium one, was a valuable opportunity to maintain a solid level of scientific interaction within the community.

The reality of conferences and workshops in astronomy has recently returned to the in-person participation. While it is desirable that the near future will allow the community to maintain stable channels of communication and fruitful exchanges, the uncertainties related to the future impact of COVID19, the economical instability and the climate crisis call for a careful revision of the way the scientific community interacts. Moreover, the necessity of hosting scientific events able to include the most diverse plethora of attendees is a factor that should not

be ignored.

In this context, online events are an important resource to fulfill the described requirements in a sustainable way. It is a fact that some of the aspects of the in-person events (the most obvious being the possibility of unexpected encounters and the empathy implicit in the face-2-face discussions) are irreplaceable. Still, online events can and must be fully considered when planning an event. It is somehow clear that all the basic logic/scheme of a classic in-person meeting (a series of talks followed by questions) can not work for an online event. Hence, it is now important that researchers at all stages of career share their effort and creativity to design online meetings where the critical goals (e.g., foster productive discussions around major scientific questions, allow a fruitful interaction between senior astronomers and early career researchers) are not only preserved but possibly re-discovered as the core of our scientific life.

Acknowledgements

We are thankful to Nelma Silva, the Office for Science Assistant in Garching for the kind and professional support received in the organisation of the Hypatia 2023 Series.

References

- [1] Beccari, G., & Boffin, H.M.J., 2021, The Messenger 185, 23
- [2] Beccari, G., et al. 2022, The Messenger 187, 33

[‡]<https://www.eso.org/public/about-eso/vision-mission/>



Road to the stars

A unique opportunity to conduct part of
your PhD research at the
European Southern Observatory

#ESOJOBS
eso.org/studentship

ESO Headquarters, Garching near Munich, Germany
ESO Vitacura, Santiago, Chile

Application deadline: 31 May and 30 November, each year

COSMOLOGY

Cold gas in distant galaxies

Leindert Boogaard

Max Planck Institute for Astronomy, Königstuhl 17, 69117 Heidelberg, Germany

The formation and evolution of galaxies over cosmic time is a complex process that involves physics on a vast range of different scales: from the accretion of gas from the cosmic web onto galaxies, down to the formation of stars deep inside cold clouds of molecular gas. The cycle of matter flowing in-and-out of galaxies and stars is called the baryon cycle. Constraining the total amount of material that is captured in the different phases of the baryon cycle at different cosmic epochs is critical for our understanding of galaxy formation. Great progress has been made on this front observationally and the cosmic evolution of the mass density in stars and atomic hydrogen, as well as the star formation rate density are now broadly known out to $z \sim 4$ (e.g., [1]). One of the main missing pieces of this puzzle, however, is the cosmic density of cold molecular (H_2) gas. This phase is key, being most directly connected to the star formation. Constraining the cosmic molecular gas density has been a major effort in recent years on large interferometers (NOEMA, VLA and ALMA) and have recently culminated in the ALMA Spectroscopic Survey of the Hubble Ultra Deep Field (ASPECS).

ALMA Spectroscopic Survey of the HUDF

ASPECS is a three dimensional survey of the deepest region of the Hubble Ultra Deep Field (HUDF; [2, 3]). It is the first extragalactic large programme with ALMA and designed to provide a flux-limited census of the cosmic molecular gas and dust. This is achieved by scanning the complete ALMA 3.0 mm and 1.2 mm bands for the emission from carbon monoxide (CO) and other tracers of the molecular gas (e.g., [C I]) as well as the dust continuum emission. The main data products from ASPECS are two datacubes that contain the line and continuum emission. The depth and wide frequency coverage result in a very high continuum sensitivity and the dust continuum map at 1.2 mm reaches an unprecedented $9.3 \mu\text{Jy beam}^{-1}$, revealing dozens of dust-rich galaxies in the HUDF ([4]). The ASPECS survey is complete and the reduced and calibrated data products and catalogs have been released[§].

Gas mass-selected galaxies

Here, we focus on the gas emission and start by answering what is perhaps the most simple question that one can ask given a survey like ASPECS: which galaxies harbour the cold molecular gas? All the bright emission lines that are detected in the ASPECS data can be uniquely associated with galaxies at $z = 1 - 4$ that are detected in the Hubble Space Telescope and multi-wavelength imaging. Instrumental for the identification are also the deep VLT/MUSE observations from the MUSE GTO survey ([5]), that provide redshifts and metallicities for many galaxies. The galaxies show a variety of morphologies, ranging from compact and/or clumpy structures, to more

extended disks. The star formation rates of the galaxies place them above, on and also, interestingly, below the typical star formation rates at a given stellar mass and redshift (the so-called ‘galaxy main sequence’). The latter sources are particularly important, as these galaxies would not normally be selected for follow-up observations in targeted surveys, but are key to get a complete census of the molecular gas. Overall, we find that ASPECS detects roughly half of all the galaxies in the HUDF above a stellar mass of $10^{10} M_{\odot}$ at $1 < z < 2$ and $10^{10.5} M_{\odot}$ at $2 < z < 3$ ([6]).

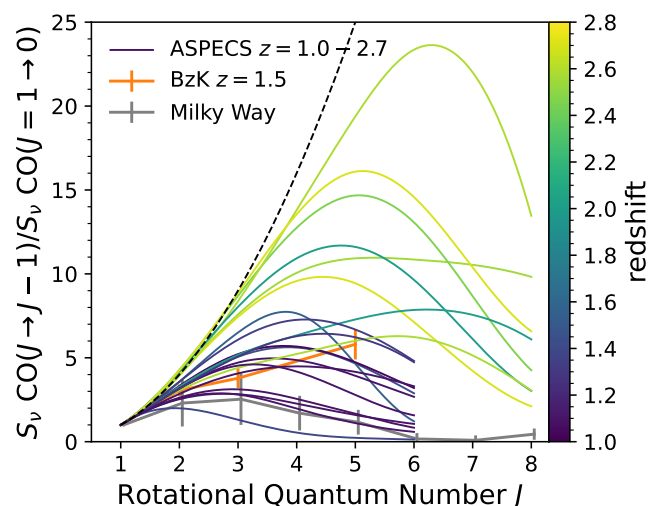


Figure 1: Modelled CO excitation ladders (normalised and colored by redshift) for the gas mass-selected galaxies from the ASPECS survey ([7]). The galaxies at $2 < z < 3$ show on-average higher gas excitation than those at $1 < z < 2$, suggesting an intrinsic evolution in the ISM conditions with redshift. Understanding the variations in the gas excitation conditions with galaxy properties is essential to infer the total mass in cold gas and the boundary conditions for star formation.

Conditions in the cold interstellar medium

The conditions in the cold interstellar medium of the galaxies are important, because they set the boundary conditions for the fragmentation of the molecular clouds and the onset of star formation. Furthermore, they impact the conversion factors required to convert the observed line emission to a total molecular gas mass, especially when only excited states of CO are observable (which is common at higher redshifts). On average, the MUSE spectra show the sources at $1 < z < 2$ have roughly solar metallicity, motivating the choice of a galactic CO-to- H_2 conversion factor. By modeling the multi-line CO, [C I] and dust continuum measurements for all the ASPECS sources using radiative transfer models, the overall excitation of the sources can be constrained (see Figure 1). We find that the ASPECS galaxies at $z = 1 - 2$ show

[§]<https://www.aspecs.info> and <https://almascience.org/alma-data/lp/ASPECS>

a range in excitation in their mid- J lines that on-average lies above that of the Milky Way, but below that of earlier sub-millimeter-selected sources at similar redshifts (that have higher IR luminosities). The sources at $2 < z < 3$ show more highly excited gas than those at lower redshift. Interestingly, none of the lower redshift sources show excitation as high as the average of the galaxies at $2 < z < 3$, even though the cosmic volume probed is similar to within a factor of 2. This suggests there is an intrinsic evolution in the excitation conditions, where galaxies at higher redshift have on-average more highly excited gas, potentially due to their higher (surface) densities of star formation rate and molecular gas ([7]).

Pushing to higher redshifts

The large number of redshifts from Lyman- α at $z \geq 3$ from the MUSE HUDF Survey provides a unique opportunity to push the sensitivity of ASPECS at $z = 3-4$ through stacking. To this end, we performed a survey of all the brightest ($H < 26$ AB magnitude) star-forming galaxies in the MUSE HUDF at these redshifts with VLT/KMOS and Keck/MOSFIRE, to get their systemic redshifts (as Ly α itself is typically seen offset from the systemic velocity). We do not detect emission from CO, [C I] or dust in the stacks, which is consistent with the expected gas fractions from scaling relations, but only for a substantially higher gas and dust mass-to-light ratios than seen in the Milky Way. Such conversion factors are in agreement with the significantly sub-solar metallicity of the galaxies on average ($12 + \log(O/H) \approx 7.8$; median $\log M_* [M_\odot] = 10^{9.1}$), but emphasise that it may become increasingly challenging to detect cold gas with classical tracers in typical star-forming galaxies at $z > 3$ ([8]).

Cosmic molecular gas density and the baryon cycle

Through a statistical analysis of all the molecular line emission in the datacubes, ASPECS provides unprecedented constraints on the cosmic evolution of the molecular gas density. The density of molecular gas increases from high redshift up to a peak at $z \sim 1.5$, followed by a decline of a factor ~ 6 to the present. This evolution is overall similar to the evolution of the cosmic star formation rate density and suggests that the evolution of the star formation rate is to first order driven by the availability of molecular gas ([9]).

The evolution of the cosmic molecular gas (H_2) density can be combined with the evolution of the stellar

mass, star formation rate and HI density, to constrain the evolution of baryons associated with galaxies averaged over time and space. Interesting results that arises from this are that the stellar mass density increases over time and exceeds the total gas density in HI and H_2 by $z \sim 1.5$. As the subsequent decline in the molecular gas density between $z \sim 1.5$ and the present is insufficient to account for the growth in stellar mass over the same time period, this implies that additional accretion of gas into the cold molecular medium has to take place ([1]).

Future directions

ASPECS provides unprecedented constraints on the overall molecular gas and dust content of galaxies averaged over space and time, and follow-up work is ongoing to refine and dissect the measurements in different ways. This includes enlarging the cosmic volume that is probed to further constrain cosmic variance (cf. WIDE ASPECS). The constraints on the cold gas masses are only as good as our understanding of the conditions inside the cold interstellar medium. To date, there is still a limited understanding of the CO excitation in typical star-forming galaxies around cosmic noon and future multi-frequency studies observations of different tracers will better anchor the gas mass measurements. Apart from this, ASPECS was designed to maximise the sensitivity for molecular gas and the observations are therefore unresolved. Now that the gas-rich galaxies in the HUDF are pinpointed, resolved follow-up observations will be able to further constrain the gas dynamics in the galaxies. In all these cases, facilities such as ALMA, NOEMA and (later) the ngVLA will play a key role. Together with the upcoming extensive observations of the HUDF from the the James Webb Space Telescope, these will soon provide an even more detailed picture of the evolution of the cosmic gas fractions in galaxies out to cosmic noon and beyond.

References

- [1] Walter, F., *et al.*, 2020, ApJ, 902, 111
- [2] Walter, F., *et al.*, 2016, ApJ, 833, 67
- [3] Decarli, R., *et al.*, 2019, ApJ, 882, 138
- [4] González-López J., *et al.*, 2020, ApJ, 897, 91
- [5] Bacon, R., *et al.*, 2017, A&A, 608, A1
- [6] Boogaard, L.A., *et al.*, 2019, ApJ, 882, 140
- [7] Boogaard, L.A., *et al.*, 2020, ApJ, 902, 109
- [8] Boogaard, L.A., *et al.*, 2021, ApJ, 916, 12
- [9] Decarli, R., *et al.*, 2020, ApJ, 902, 110

Short CV



2016: MSc in Astronomy, Leiden University, Leiden, The Netherlands
 2016-2021: PhD in Astronomy, Leiden University, Leiden, The Netherlands
 2021-present: Postdoc, Max Planck Institute for Astronomy, Heidelberg, Germany

Toward an independent reconstruction of the expansion history of the Universe

Nicola Borghi

Department of Physics and Astronomy “Augusto Righi”, University of Bologna, Italy
 INAF–Astrophysics and Space Science Observatory of Bologna, Italy

The current tensions in cosmology, in particular the emerging discrepancy between the Hubble constant H_0 measured in the local universe with type-Ia supernovae and the one inferred from the CMB by assuming a Λ CDM model, require a deep understanding of the involved systematics and/or new physics, as well as the study of new and independent cosmological probes to better understand the expansion history of the Universe [1, 2].

In this context, *cosmic chronometers* (CC) have proven to be very promising probes to obtain *direct* measurements of the Hubble parameter $H(z)$ up to $z \sim 2$. The method, firstly introduced by Jimenez [3], consists in using massive and passive galaxies as tracers of the aging of the universe dt_U as a function of z under the minimal assumption of a FLRW metric, $H(z) = -(1+z)^{-1} dz/dt_U$. Provided that an accurate selection of CCs is performed, their aging dt can take the place of dt_U in the equation above. This method does not depend on the assumption of a specific cosmological model (e.g., Λ CDM), relies on differential – not absolute – age estimates, and makes use of a class of galaxies that is relatively simpler to model. However, accurate measurements require deep spectroscopic observations to break internal degeneracies between stellar population parameters (e.g., age and chemical content; for an updated review see [2]).

Cosmic chronometers in the LEGA-C survey

The Large Early Galaxy Census Astrophysics (LEGA-C, ESO programs 194.A-2005, 1100.A-0949) in an ESO public spectroscopic survey carried out at VLT/VIMOS targeting ~ 3000 K_s -band-selected galaxies at $0.6 < z < 1$ with typical continuum $S/N \sim 17$ and spectral resolution of $R \sim 3500$.

In Borghi [5], we select 350 cosmic chronometers in LEGA-C by crossing multiple observational criteria to maximize the purity of the sample: photometric $NUVrJ$ selection, spectroscopic $EW[OII]$ cut, and visual inspection of OII and OIII regions to further reduce galaxies with potential residual or recent star formation. With these criteria we obtain galaxies with a typical stellar velocity dispersion $\sigma_* \sim 206$ km s^{-1} , stellar mass $\log M_*/M_\odot \sim 11$, and specific star formation rates $\log sSFR/\text{yr} \sim -12$, typical of very massive and passive systems at this redshift.

We also study the H/K , a new diagnostic based on the Ca II H and K features measured as Lick indices. In passive systems, K is deeper than H, i.e. $H/K < 1$, but even the presence of a small fraction ($< 5\%$) of young (< 1 Gyr) stars, can invert the ratio. This is because A- and B-type stars have a strong $H\epsilon$ Balmer absorption line which overlaps the Ca II H line. In our passive

sample we measure, $\langle H/K \rangle = 0.96 \pm 0.08(1\sigma)$, which is an independent confirmation that our sample of cosmic chronometers is compatible with no or negligible star forming contaminants (for more details see Borghi [5]).

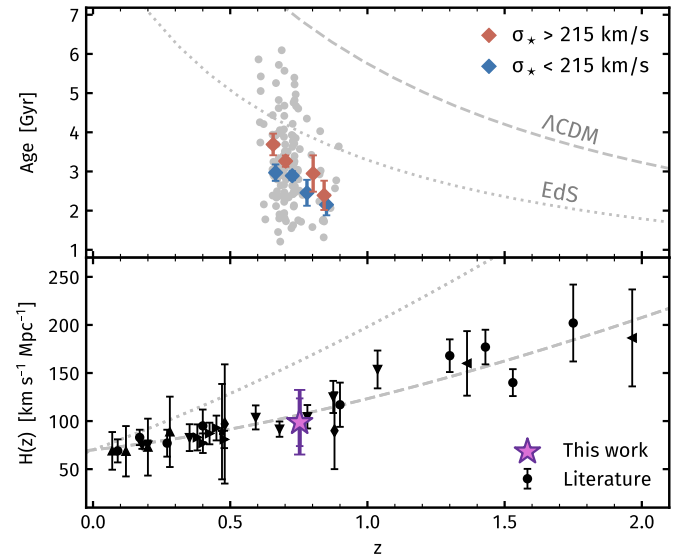


Figure 1: *Upper panel:* age–redshift relation for cosmic chronometers selected in the LEGA-C survey (gray points) binned into higher (red) and lower (blue) σ_* regimes. *Lower panel:* $H(z)$ measurement (violet star) with statistical (inner error bar) and total (outer error bar) uncertainties. Black points are literature data (see [2]). Figure from [7].

Analysis of the stellar populations properties

To better understand the physical properties (in particular the age) of the selected CCs, we measure informative spectral features (Lick indices) on each galaxy’s spectrum using `PyLick` (available at <https://gitlab.com/mmoresco/pylick>). An optimized set of indices is compared to the Thomas [6] simple stellar population models to constrain the mean age, $[Z/H]$, and $[\alpha/H]$. Extra care has been taken not to introduce cosmological assumptions which would invalidate the subsequent analysis. In particular, we do not set cosmological upper priors on the maximum allowed age.

We find that the parameter space covered by the CCs at $z \sim 0.7$ is comparable to the one of the local massive early type galaxies, with positive trends in stellar velocity dispersion, confirming the mass-downsizing scenario (i.e., more massive galaxies evolved earlier and faster). Within $0.6 < z < 0.9$ we observe no significant $[Z/H]$ and $[\alpha/H]$ evolution (typical values are $\langle [Z/H] \rangle = 0.08 \pm 0.18$ and $\langle [\alpha/Fe] \rangle = 0.13 \pm 0.11$), but a visible $age(z)$ trend (Figure 1, *upper panel*).

A new $H(z)$ measurement

In Borghi [7], we analyze the cosmological implications and, by applying the cosmic chronometer method, we obtain a new $H(z)$ measurement. We bin the LEGA-C CCs into two σ_* regimes (with a threshold of 215 km/s) and four z bins. This allows us to trace the underlying cosmological aging with sufficient resolution, while minimizing the scatter due to individual galaxies' formation pathways. We find two parallel median $\text{age}(z)$ relations with a difference of $\Delta \text{age} \approx 0.5$ Gyr that can be interpreted as a delay in formation time, with earlier formation epochs for more massive galaxies (Figure 1, *upper panel*). By measuring $\Delta z/\Delta \text{age}$ between each two non-consecutive bins, we derive four $H(z)$ measurements, that we average obtaining, $H(z) = 98.8 \pm 24.8$ (*stat*).

What are the main sources of systematic uncertainties? Previous efforts by Moresco [9] have demonstrated that the choice of the stellar population model plays a major role in the overall systematics of the CC approach, with an average contribution of about 7% on the final $H(z)$ value. We repeat the full analysis by changing: the assumed stellar population model and prescriptions, the choice of the Lick indices combination, and the binning method, obtaining a final value of $H(z) = 98.8 \pm 33.6$ (*stat + syst*) (Figure 1, *lower panel*). This is the first time the CC approach is applied with the Lick indices method, demonstrating that with high quality spectroscopy it is possible not only to study the properties of individual galaxies, but also to constrain their underlying cosmology.

Recently, Jiao [8] extended this work by using the full-spectrum fitting approach. Despite the completely different method, stellar population synthesis models and prescription (e.g. extended star formation history), the final $H(z)$ values are consistent within 0.2σ .

Future perspectives

A dedicated observing program targeting cosmic chronometers and a meticulous and detailed improvement of stellar population synthesis models, are the ideal pathways to reach the precision of other standard cosmological probes. In the near future, the combination of a BOSS-like and a EUCLID-like survey would already significantly improve our knowledge on $H(z)$ (Figure 2).

Already today, gravitational waves (GW) can provide an independent $H(z)$ hook at $z = 0$ for CCs. In fact, the GW signal from a compact binary coalescence is a direct tracer of its luminosity distance d_L [4], requiring no further

calibration other than the general relativity (unlike e.g., supernovae). By complementing this information with a z measurement (e.g., from an electromagnetic counterpart) or a statistical inference based on the distribution of potential hosts, it is therefore possible to obtain a local measurement of $H_0 \approx cz/d_L + \mathcal{O}(z^2)$. Moreover, with third generation GW detectors and upgrades of the existing ones it will be possible to study $d_L(z)$ and then infer the expansion history at higher redshift (Figure 2).

In conclusion, the synergy between cosmic chronometers and gravitational waves has a high potential to pave the way toward an independent reconstruction of the expansion history of the Universe.

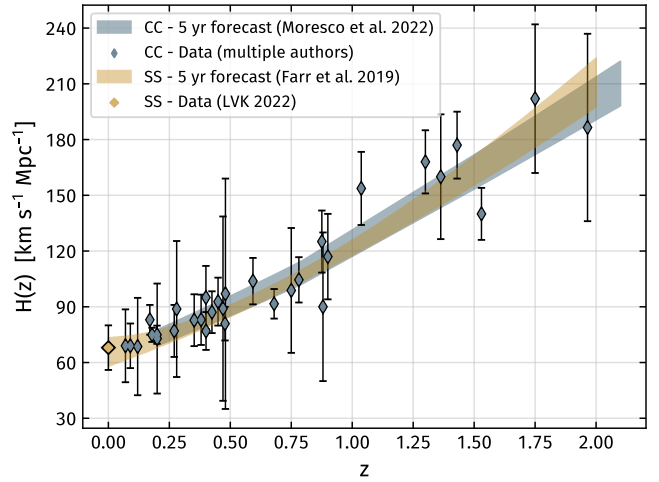


Figure 2: Current and future constraints to the cosmic expansion history $H(z)$ using cosmic chronometers (CC; blue, see [2]) and gravitational wave events as standard sirens (SS; gold, see [10]).

References

- [1] Abdalla, E., et al. 2022, JHEAp, 2204, 002
- [2] Moresco, M., et al. 2022, arXiv:2201.07241
- [3] Jimenez, R., & Loeb, A. 2022, ApJ, 573, 37
- [4] Schutz, B., F., 1986, Nat, 323, 310
- [5] Borghi, N., et al. 2022a, ApJ, 927, 164
- [6] Thomas, D., et al. 2011, MNRAS, 412, 4
- [7] Borghi, N., et al. 2022b, ApJL, 928, L4
- [8] Jiao, K., et al. 2022, arXiv:2205.05701
- [9] Moresco, M., et al. 2020, ApJ, 898, 82
- [10] Farr, W., et al. 2019, ApJL, 883, L42

Short CV



2020: Master in Astrophysics and Cosmology, University of Bologna, Italy
2020–present: PhD in Astrophysics, University of Bologna, Italy

The most giant radio structures in the Universe

Andrea Botteon

Leiden Observatory, Leiden University, Niels Bohrweg 2, 2300 RA Leiden, The Netherlands

Galaxy clusters are the largest and most massive gravitationally bound systems in the Universe, reaching linear sizes of a few Mpc and masses up to $10^{15} M_{\odot}$. Although the richest clusters may contain thousands of galaxies in their volume, galaxies account only for $\sim 5\%$ of the cluster total mass which is instead dominated for about $\sim 80\%$ by dark matter. The remaining $\sim 15\%$ is in form of intra-cluster medium (ICM), a tenuous ($n_e \sim 10^{-3} - 10^{-4} \text{ cm}^{-3}$) and hot ($T \sim 10^7 - 10^8 \text{ K}$) plasma whose thermal bremsstrahlung emission is detectable in the X-rays.

Clusters of galaxies form hierarchically via energetic merger events. During these cosmic collisions, shocks and turbulence are injected in the ICM, and often generate cluster-wide synchrotron sources with steep spectrum ($\alpha > 1$, with $S_{\nu} \propto \nu^{-\alpha}$, where S_{ν} is the flux density at frequency ν and α is the spectral index). These sources are called radio halos and relics, and are currently observed in a fraction of massive clusters [1]. The existence of diffuse Mpc-scale synchrotron emission in clusters challenges our understanding of cluster astrophysics as it probes a complex hierarchy of (novel) mechanisms in the ICM that are essentially able to turn gravitational energy into particle acceleration and magnetic field amplification [2]. It is currently thought that radio halos trace turbulent regions where relativistic particles are trapped and re-accelerated through scattering with magnetohydrodynamics turbulence. Instead, radio relics originate as a consequence of the particle acceleration and magnetic field amplification undergoing at merger shocks located in cluster outskirts.

Despite the observed connection between mergers and radio halos and relics, little is known about the generation of synchrotron emission in the very early phase of a merger (Figure 1). Systems in this merging phase are referred to as pre-merging clusters. Until recently, it was still unclear if a significant fraction of the energy of gas dynamics can be channelled into non-thermal components during the pre-merger phase becoming detectable in the radio band.

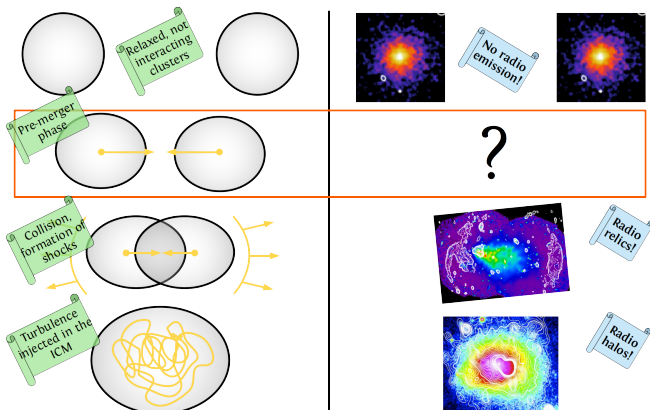


Figure 1: Schematic view of a binary cluster merger.

The ongoing progress in radio instrumentation has recently made possible to enter into a new regime in which non-thermal phenomena can be studied in large-scale structures. In particular, the LOw Frequency ARray (LOFAR) enabled the first detailed observations of galaxy clusters at frequencies of $< 200 \text{ MHz}$ thanks to the unprecedented high sensitivity and high resolution in its operational frequency range.

The discovery of radio bridges

Pairs of galaxy clusters are rare systems composed of two close-by clusters that are bound together by gravity. Their observation gives us the chance to study the phases of the merger closer to the epoch of the collision and to understand the impact of mergers on cluster evolution. In particular, Abell 1758 is a system located at $z = 0.279$ composed of two massive galaxy clusters separated by a projected distance of $\sim 2 \text{ Mpc}$: Abell 1758N (in the north, the most massive one) and Abell 1758S (in the south). X-ray observations suggest that the two clusters are gravitationally bound but have not interacted yet, that is, they are in a pre-merger phase. In addition, complex cluster dynamics and multiple sub-substructures are observed both in Abell 1758N and Abell 1758S, indicating that each of the two clusters is undergoing its own merger. In Botteon et al. [3], we used an 8 h observation at 144 MHz from the LOFAR Two-meter Sky Survey (LoTSS) to study the well-known radio halo in Abell 1758N and also discovered a new radio halo and a candidate radio relic in Abell 1758S. More importantly, at low resolution we found a hint (2σ) of a bridge of radio emission connecting the two clusters which required a further study with more sensitive observations. With the deep and multi-frequency follow-up observations of the cluster we were able to firmly claim the presence of a giant radio bridge at 144 MHz that fills the volume between the two clusters (Figure 2, left), while only hints of radio emission were observed at 53 and 383 MHz [4].

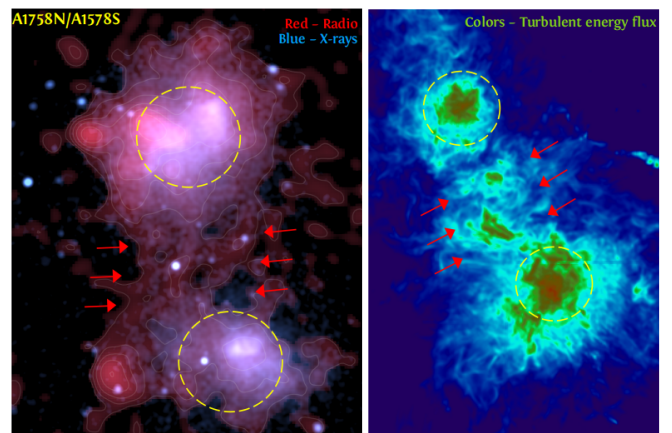


Figure 2: Radio bridges in Abell 1758N-1758S (left, [3, 4]) and in simulations (right, [6]). Dashed yellow circles have a diameter of $\sim 1 \text{ Mpc}$.

The detection of radio emission from the region between pre-merging galaxy clusters demonstrates, for the first time, that even in environments where the average particle energy is much lower than within a cluster, particles can be (re)accelerated by shocks and/or turbulence at meaningful levels. These regions are in fact at the crossroads between the denser and hotter ICM regions and the colder and rarefied cosmic web and thus allow us to study particle acceleration mechanisms in new regimes, still poorly constrained from theory.

Presently, the pre-merging cluster pairs Abell 1758N-1758S (at $z = 0.279$) and Abell 399-401 (at $z = 0.07$, [5]) are the only two cases where a bridge of radio emission between two clusters has been observed. The two systems show remarkable similarities. First of all, each of the two main components of the pairs is a massive cluster, with $M_{500} > 5 \times 10^{14} M_{\odot}$. Secondly, both are pairs of dynamically disturbed clusters, with all four clusters undergoing mergers and hosting a radio halo. Thirdly, the diffuse radio emission from the bridges connecting the two pairs (detected in both cases with LOFAR 144 MHz observations) spans a scale of ~ 2 -3 Mpc and has similar mean radio emissivity.

Two models have been proposed to explain the acceleration of relativistic electrons and amplification of magnetic fields in the compressed region between clusters: one involves the presence of weak shocks [5], the other of turbulent motions [6]. According to the latter, turbulence may produce steep spectrum ($\alpha > 1.3$) and volume filling synchrotron emission in the entire bridge region (Figure 2, right). The analysis of radio and X-ray observations of Abell 1758N-1758S are in agreement with these predictions [4]. However, deeper data on this system as well as observations of other cluster pairs are still required to firmly determine the origin of radio bridges.

LOFAR observations of other cluster pairs

LOFAR observations at 144 MHz have been used to search for radio emission between clusters in other complex systems with multiple components. For example, in the spectacular cluster chain Abell 781 we did not find any diffuse emission [7], while in the pair Abell 1430 we found an atypical diffuse radio emission in a low-density environment that was dubbed “Pillow” [8]. The Lyra complex is another interesting pre-merging cluster pair that we observed recently [9]. Despite the absence of a radio bridge between the two clusters, we discovered a new radio halo in the main cluster component (Figure 3). This halo has a low-surface brightness extension towards the SW, leading to a maximum linear extent of the diffuse radio emission up to ~ 1.8 Mpc. As for the case of radio bridges, the presence of an extension of a radio halo probes the existence of non-thermal components at large

distances from the cluster center. In particular, we speculated that the emission in this system is a consequence of the energy dissipated on small scales due to the interaction between the main cluster of the pair and another galaxy group present in the complex (Figure 3).

Compared to the radio bridge pairs Abell 1758N-1758S and Abell 399-401, the other systems observed with LOFAR are less massive, possibly suggesting a role of the mass in the generation of observable levels of synchrotron emission between pre-merging clusters.

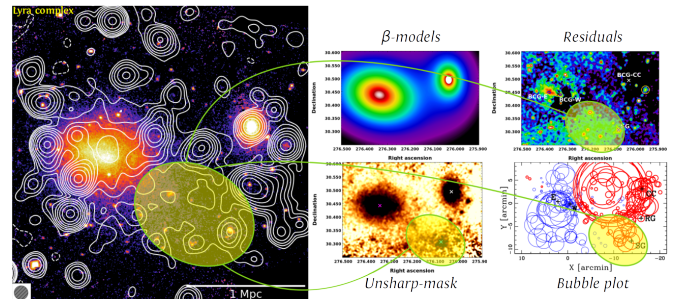


Figure 3: LOFAR (contour) and XMM-Newton (color) overlay of the Lyra complex (left). The SW low-surface brightness extension of the newly discovered radio halo is highlighted in the figure. Optical and X-ray observations indicate the presence of substructure in this region (right).

Conclusions

The detection of radio bridges and extensions of radio halos demonstrates the existence of magnetic fields and particle acceleration mechanisms at large distance from the cluster center. Particularly, the discovery of radio bridges in pre-merging cluster pairs probed for the first time that non-thermal phenomena can be generated by mechanisms that are not necessarily related to the energy dissipated as a consequence of cluster mergers. Future radio (e.g. LOFAR2.0 and SKA) and X-ray (e.g. Athena) instruments will play a crucial role to efficiently study cluster outskirts and determine how common are gigantic radio sources in clusters, what are the physical processes that generate them, and what is their connection with the large-scale structure of the Universe.

References

- [1] van Weeren R., et al. 2019, Space Sci. Rev., 215, 16
- [2] Brunetti G., & Jones T., 2014, IJMPD, 23, 30007
- [3] Botteon, A., et al. 2018, MNRAS, 478, 885
- [4] Botteon, A., et al. 2020, MNRAS, 499, L11
- [5] Govoni, F., et al. 2019, Science, 364, 981
- [6] Brunetti, G., & Vazza, F. 2020, PRL, 124, 051101
- [7] Botteon, A., et al. 2019, A&A, 622, A19
- [8] Hoeft, M., et al. 2021, A&A, 654, A68
- [9] Botteon, A., et al. 2019, A&A, 630, A77

Short CV



- 2013: Bachelor in Astronomy, University of Bologna, Italy
- 2015: Master in Astrophysics and Cosmology, University of Bologna, Italy
- 2018: PhD in Astrophysics, University of Bologna and INAF-IRA, Italy
- 2018–2019: Postdoc Researcher, University of Bologna and INAF-IRA, Italy
- 2019–present: Postdoc Researcher, University of Leiden, The Netherlands

Improved strong lensing modelling of galaxy clusters using the Fundamental Plane: detailed mapping of the baryonic and dark matter mass distribution of Abell S1063

Giovanni Granata

Dipartimento di Fisica, Università degli Studi di Milano, Via Celoria 16, I-20133 Milano, Italy

Galaxy clusters are the most massive gravitationally bound structures in the Universe, and around 85 – 90% of their total mass is under the form of dark matter (DM). As a consequence, they are excellent astrophysical laboratories to test our hypotheses on the nature of DM itself. Thanks to several dedicated photometric and spectroscopic surveys, strong gravitational lensing (SL) has become the most accurate probe of the total mass distribution in the cores (out to a few hundreds of kiloparsecs from the centre) of massive galaxy clusters. SL can be combined with baryonic mass diagnostics to disentangle the mass distribution of cluster- and galaxy-scale DM haloes from the total mass distribution of the cluster. The resulting DM mass profiles can be compared to the predictions of high-resolution cosmological simulations, based on the Λ cold dark matter (CDM) Cosmological Model.

The remarkable improvement in the accuracy of SL models, driven by recent observational campaigns, has allowed us to map robustly the mass distribution of the DM haloes hosting the member galaxies (usually referred to as sub-haloes). On this scale, a significant discrepancy between the predictions of SL models and high-resolution simulations has recently emerged: at a fixed galaxy total mass, sub-haloes extracted from SL models are more compact than their simulated counterparts [2].

The accuracy in the description of the cluster members in SL models is limited by the degeneracies between the parameters defining their mass distribution. These degeneracies have been reduced with the introduction of measured priors on the velocity dispersion of the cluster galaxies. However, the usual choice of adopting power-law scaling relations, with no scatter, to link the total mass of members with their luminosity is still a simplified approach. To obtain a more complex description of the cluster galaxies, we take advantage of measured kinematics and structural parameters of the cluster galaxies to calibrate the Fundamental Plane (FP) for the members of the massive galaxy cluster Abell S1063 (AS1063). Our results are presented in [1]

Building the strong lensing model of Abell S1063

AS1063 is one of the six massive clusters included in the Hubble Frontier Fields (HFF, [3]) photometric survey. We build a SL model of its total mass distribution using the recent work by [4] as a starting point and reference. Like [4], we model the diffuse DM and hot-gas mass distribution with isothermal cored haloes. The parameters

of the hot-gas mass distribution are fixed from observations [5]. The parameters of the cluster-scale DM mass distribution are optimised comparing the observed and model-predicted positions of the same multiply-imaged background sources. Likewise, we model the cluster galaxies with spherical, isothermal, truncated total mass distributions. The total mass profile of each member is entirely defined by two parameters: its velocity dispersion and its truncation radius. While in [4] their values are derived with fixed power-law relations with respect to their observed total luminosity, we choose to consider the FP, a more accurate scaling law, which involves the magnitude, the half-light radius, and the central velocity dispersion of early-type galaxies.

We use HFF images in the F814W band to measure the values of the magnitude and of the half-light radius of all cluster members. Furthermore, for a sizeable subset of them, MUSE-VLT integral field spectroscopy allows us to determine the values of the line-of-sight central velocity dispersion. We calibrate the FP relation, and then use it to obtain the values of the velocity dispersion of all cluster members from their measured structural parameters. This procedure allows for a more accurate determination of the velocity dispersion values compared to the power-law approach. As for the truncation radii of the galaxies, we calibrate a proportionality relation with their observed half-light radii and use it to determine their values. Thanks to this procedure, we can thus fix the total mass distribution of all member galaxies in a new SL model of the cluster.

The more stringent constraints on the the mass distribution of the members compared to previous works result in a reduction of the statistical uncertainty on the parameters of the cluster-scale DM component, and in particular on the value of the core radius of the main DM halo of the cluster. The new procedure also allows for more realistic scaling laws between the observables that describe the physical properties of the cluster members. For instance, the relation between the values of their total mass and their velocity dispersion is no longer a fixed power-law and now shows a significant scatter and a shallower slope.

Mass profile decomposition

We decompose the total mass profile of the cluster derived from our new best-fit SL model into all its baryonic and DM components. As anticipated, the hot-gas mass profile is derived from X-ray observations. Combining

instead the measured stellar mass values of the cluster members, presented in [6], with their surface brightness profile in the HST F814W band, we derive the stellar mass profile of the cluster. We can thus disentangle the mass profiles of the various cluster- and galaxy-scale DM haloes by subtracting the baryonic component to the total mass distribution. This also allows us to derive the cumulative projected gas-, stellar-, and baryonic-to-total mass fractions out to a projected distance of 350 kpc from the cluster centre: at this radius, we find a baryonic mass fraction of 0.147 ± 0.002 . The profiles are presented in Figure 1.

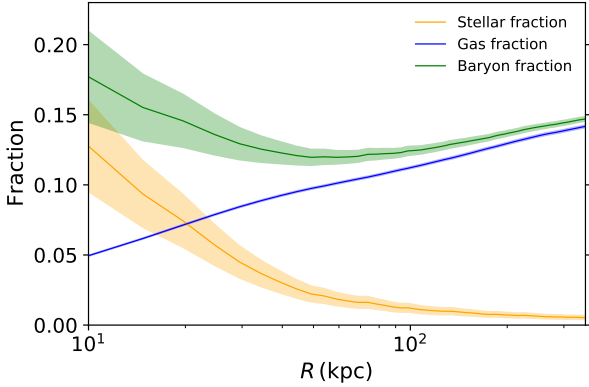


Figure 1: Cumulative stellar-, gas-, and baryonic-to-total mass fractions from the model presented in [1]. Error bars are derived from the observations.

Comparison with cosmological simulations

As anticipated, comparing the physical properties of the DM sub-haloes as predicted by SL models to the most recent cosmological simulations is a test of the foundations of the Λ CDM cosmological model on which the simulations are based, and of the micro-physics of DM. We first compare the stellar-to-total mass fractions of the cluster members with the predictions of recent HOD studies based on DM-only N -body simulations [7]. We find a significant discrepancy: the stellar mass fraction values predicted by SL models are almost an order of magnitude higher than those predicted by the HOD procedure. This discrepancy is resolved if one considers, instead, hydrodynamical simulations, which include gas particles and stars, as well as the effects of the interaction between baryons and DM during the formation of clusters. We consider high-resolution simulations of clusters with a mass similar to that of AS1063 from [8]. We perform two-dimensional projections to simulate the lensing observational conditions. In this case, we find compatible

stellar mass fraction values from the SL model and the simulation suite.

Secondly, we examine how sub-haloes extracted from lensing models compare to their simulated counterparts in terms of maximum circular velocity, which is a proxy for their compactness. [2] recently found that hydrodynamical simulations predict high-mass sub-haloes (total mass $M > 10^{10} M_{\odot}$) to be significantly less compact than forecast by a sample of state-of-the-art SL models, including the model of Abell S1063 presented in [4]. The new technique we adopt significantly impacts the relation between the total mass and the maximum circular velocity of the sub-haloes, obtaining again a different slope compared to [4] and allowing for the inclusion of a scatter. However, as shown in Figure 2, our results agree with those from [4] in the mass range considered, thus confirming the reported discrepancy. Several tests to infer the origin of this discrepancy are being performed, focusing both on SL modelling and on the implementation of the cosmological simulations. However, no conclusive answer has been obtained so far. This leaves several open questions, and could point towards a new fundamental challenge for the Λ CDM paradigm.

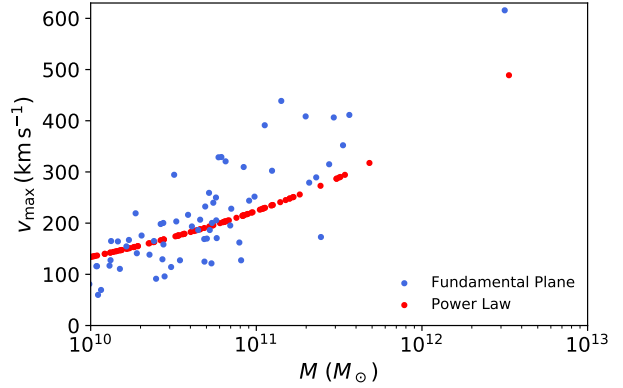


Figure 2: Maximum circular velocity of the cluster members as a function of their total mass. The values predicted by the models presented in [1] and [4] are shown in blue and in red, respectively. Only members with $M > 10^{10} M_{\odot}$ are shown.

References

- [1] Granata, G., et al., 2022, A&A, 659, A24
- [2] Meneghetti, M., et al., 2020, Science, 369, 1347
- [3] Lotz, J. M., et al., 2017, ApJ, 837, 97
- [4] Bergamini, P., et al., 2019, A&A, 631, A130
- [5] Bonamigo, M., et al., 2018, ApJ, 864, 98
- [6] Mercurio, A., et al., 2021, A&A, 656, A147
- [7] Girelli, G., et al., 2020, A&A, 634, A135
- [8] Planelles S., et al., 2014, MNRAS, 438, 195

Short CV



2018: BSc in Physics, University of Milan
 2020: MSc in Physics, University of Milan
 2020–present: PhD in Physics, Astrophysics and applied Physics, University of Milan

GOODS-ALMA 2.0: Understanding the role of compact star formation in galaxy evolution

Carlos Gómez-Guijarro

CEA, Université Paris-Saclay, Université Paris Diderot, Sorbonne Paris Cité, 91191, Gif-sur-Yvette, France

Massive elliptical galaxies in the local universe appear to have their high redshift analogs in the form of extremely compact quiescent galaxies. Therefore, it seems that compact star formation appears to play a pivotal role in the evolutionary pathways of massive galaxies across cosmic history. However, there are fundamental unresolved questions debated in the literature: How systematic is compact star formation in star-forming galaxies (SFGs) at high redshift? What is its role in the broader picture of the scaling relations in galaxy evolution? The results here presented shed light into these fundamental questions.

Compact star formation appears to be the norm in massive galaxies at high redshift and it unveils as a physical driver of the behaviour of massive galaxies in the scaling relations. Together, compact star formation appears to be fundamental in keeping galaxies as star forming systems even when their gas to fuel star formation is very low and they are presumably on their way to quiescence.

In this text the main results from Gómez-Guijarro [3, 4] are outlined, to which the reader is referred for further details.

ALMA 1.1 mm galaxy survey in GOODS-South

GOODS-ALMA is a 1.1 mm galaxy survey carried out with ALMA Band 6 in the GOODS-South field. It covers a continuous area of 72.42 arcmin^2 centered at $\alpha = 3^{\text{h}}32^{\text{m}}30^{\text{s}}$, $\delta = -27^{\circ}48'00''$ at a homogeneous sensitivity with two different array configurations, in order to include both small and large angular scales. The high resolution dataset was presented in Franco [2]. In this 2.0 version, we present the low resolution dataset and its combination with the high resolution dataset (combined dataset), reaching an average sensitivity of $\sigma = 68.4 \mu\text{Jy beam}^{-1}$ at an average angular resolution of $0.447'' \times 0.418''$. In Gómez-Guijarro [3], we construct a source catalog, derive number counts, and dust continuum sizes at 1.1 mm.

A total of 88 galaxies are detected in a blind search, compared to 35 in the high resolution dataset alone. We find 44 sources with a detection $S/N^{\text{peak}} \geq 5$ associated to a purity $p = 1$. Using a prior-based methodology we find another 44 sources with a detection $3.5 \leq S/N^{\text{peak}} < 5$. These galaxies span mostly $0.25 < S_{1.1\text{mm}} < 3 \text{ mJy}$, $1 < z < 4$, $\log(M_*/M_{\odot}) > 10$.

Among these galaxies, 13 out of the 88 are optically dark/faint sources, a new population of galaxies currently undetected or very faint in all optical and near-infrared bands up to and including the H -band (H -band dropouts) in the deepest cosmological fields ($H > 27 \text{ mag}$; 5σ point source), but bright at longer near-infrared bands ($[4.5] < 24 \text{ mag}$) [e.g., 10].

Prevailing compact dust continuum sizes

Dust continuum sizes at 1.1 mm are generally compact within the sample [see also e.g., 6, 5], with a median effective radius of $R_e = 0.10'' \pm 0.05''$ (physical size of $R_e = 0.73 \pm 0.29 \text{ kpc}$, at the redshift of each source). They are found to evolve with redshift and stellar mass resembling the trends of the stellar sizes measured at optical wavelengths, albeit a lower normalization compared to those of late-type galaxies [see 3, for details].

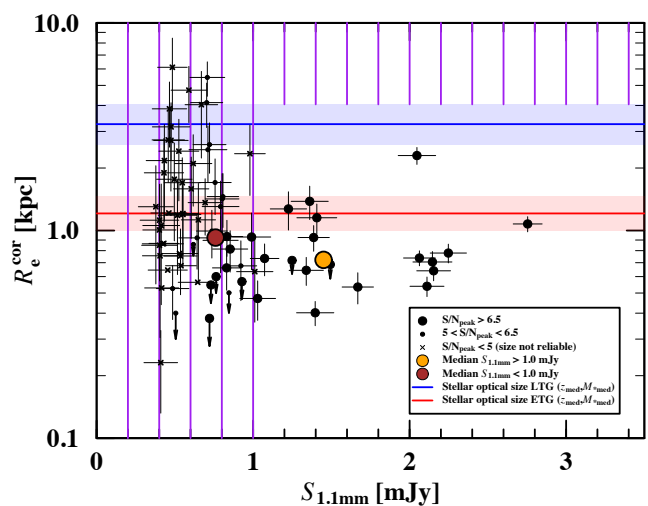


Figure 1: Physical dust continuum size at 1.1 mm scaled to the median redshift and stellar mass of the sample versus 1.1 mm flux density. The typical size of the stellar distribution measured at optical wavelengths for both early and late-type galaxies from van der Wel [9] are also shown. The grid of purple lines shows the region where the survey is no longer $\sim 100\%$ complete.

Compact dust continuum emission at 1.1 mm prevails for sources with flux densities $S_{1.1\text{mm}} > 1 \text{ mJy}$. Sizes as extended as typical star-forming stellar disks are rare (see Figure 1). At $S_{1.1\text{mm}} < 1 \text{ mJy}$, dust continuum emission at 1.1 mm appears slightly more extended, although they are still generally compact below the sizes of typical star-forming stellar disks. A larger scatter in the sizes in this flux regime is also seen, with some of the sources possibly entering the regime of the typical size of star-forming stellar disk, but the lower S/N and completeness associated to this flux regime would require further data to evaluate such sources (see Figure 1).

After covering a large contiguous area using two array configurations at a similar and homogeneous depth providing both small and large spatial scales, our findings indicate that dust continuum emission occurring in compact regions smaller than the stellar distribution appears to be a norm in dusty SFGs.

Compact star formation regulating galaxy evolution prequenching

In Gómez-Guijarro [4], we derive physical properties, such as star formation rates, gas fractions ($f_{\text{gas}} = M_{\text{gas}}/(M_{\text{gas}} + M_*)$), depletion timescales ($\tau_{\text{dep}} = M_{\text{gas}}/\text{SFR}$), and dust temperatures for the galaxy sample built from the survey and study them in the framework set by the scaling relations in galaxy evolution.

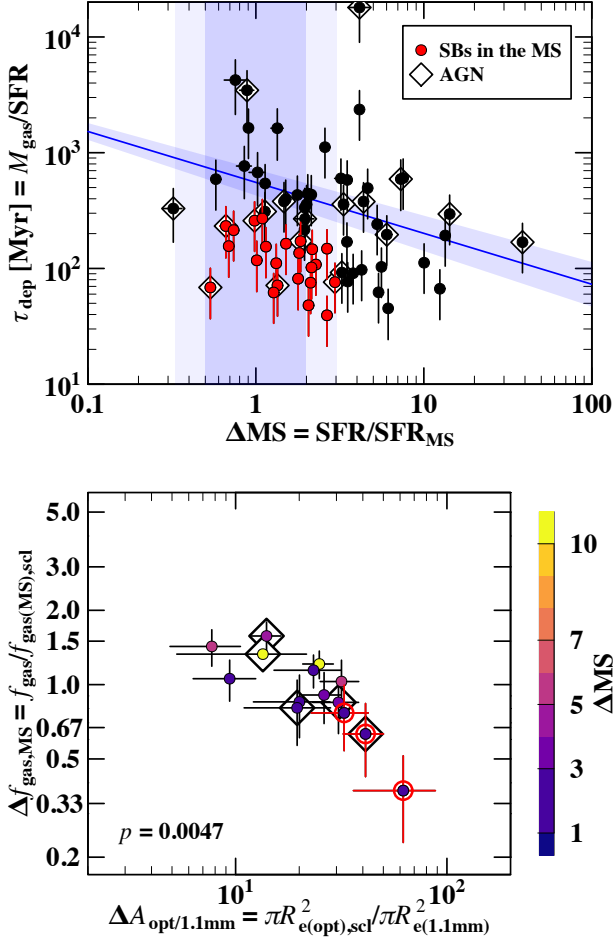


Figure 2: Top panel: Depletion timescale as a function of the distance to the main sequence of SFGs from Schreiber [7] with the scaling relation for $\tau_{\text{dep}}(z, M_*, \Delta_{\text{MS}})$ from Tacconi [8] in blue. Bottom panel: As star formation regions become more compact compared to the sizes of typical main sequence SFGs stellar disks at the same stellar mass and redshift (increasing X-axis), the gas fraction become lower compared to typical gas fraction of typical main sequence SFGs at the same stellar mass and redshift (decreasing Y-axis). Star formation regions shrink with decreasing gas content. Starburst in the main sequence are located at the extreme (highlighted in red) with the most compact star formation regions and the lowest gas content.

Our galaxy sample is located above and within the main sequence of SFGs [e.g., 7]: 42% above the main sequence ($\Delta_{\text{MS}} = \text{SFR}/\text{SFR}_{\text{MS}} > 3$) and 58% are in the main sequence within a factor 3 ($0.33 < \Delta_{\text{MS}} = \text{SFR}/\text{SFR}_{\text{MS}} < 3$, 0.5 dex).

There exist a subset of galaxies that exhibit short depletion timescales compared to typical SFGs at the same redshift, stellar mass, and distance to the main sequence. At the same time, these galaxies are located within the scatter of the main sequence. Therefore, we dubbed them as “starbursts in the main sequence” [see also 1] (see Figure 2, top panel). They also exhibit low gas fractions and high dust temperatures in comparison with typical main sequence SFGs at the same stellar mass and redshift. Besides, they account for $\sim 60\%$ of the most massive galaxies in the sample ($\log(M_*/M_{\odot}) > 11.0$).

We find that as galaxies become more compact compared to typical SFGs stellar disks, depletion timescales and gas fractions become lower, and dust temperatures higher, compared to typical main sequence SFGs, at the same stellar mass and redshift [see 4, for details]. These trends manifest a direct link between a geometrical property like the sizes of the ongoing star formation regions and other physical properties of the galaxies. Starbursts in the main sequence appear to be located at the extremes of the trends (see Figure 2, bottom panel).

Our findings suggest that the star formation rate is somehow sustained in very massive SFGs, keeping them within the main sequence even when their gas fractions are low and they are presumably on their way to quiescence. It seems that gas and star formation compression allows to hold their star formation rate.

References

- [1] Elbaz, D., 2018, A&A, 616, A110
- [2] Franco, M., 2018, A&A, 620, A152
- [3] Gómez-Guijarro, C., 2022, A&A, 658, A43
- [4] Gómez-Guijarro, C., 2022, A&A, 659, A196
- [5] Hodge, J. A., 2016, ApJ, 833, 103
- [6] Ikarashi, S., 2015, ApJ, 810, 133
- [7] Schreiber, C., 2015, A&A, 575, A74
- [8] Tacconi, L. J., 2018, ApJ, 853, 179
- [9] van der Wel, A., 2014, ApJ, 788, 28
- [10] Wang, T., 2019, Nature, 572, 211

Short CV



2013: BSc in Physics and Astrophysics, Universidad Complutense de Madrid, Spain
 2014: MSc in Astrophysics, Universidad Complutense de Madrid, Spain
 2015–2019: PhD in Astrophysics, University of Copenhagen, Denmark
 2019–present: CNRS postdoctoral researcher at UMR AIM (DAP) - CEA Saclay, France

Measuring the H I gas mass of galaxies in the early universe with cosmic explosions

Kasper Elm Heintz

The Cosmic Dawn Center (DAWN), Niels Bohr Institute, University of Copenhagen, Jagtvej 128, DK-2200 Copenhagen N, Denmark

Neutral atomic hydrogen (H I) is one of the most fundamental and dominant baryonic components of the first generation of galaxies. However, due to the weakness of the hyperfine 21-cm transition, the study of H I has been limited to the most nearby galaxies at $z \lesssim 0.3$ [1]. Even with next-generation radio facilities such as the Square Kilometre Array (SKA), this transition can only be detected from individual galaxies out to $z \approx 1.7$ [2]. This greatly motivates the use of a *proxy* to infer the H I content of the most distant galaxies. Here we present a new approach to link and calibrate the amount of H I to the bright fine-structure transition of singly-ionized carbon [C II]–158 μm in galaxies from $z \approx 1.5 - 6.5$, as presented in [3], using the optical afterglows of gamma-ray bursts (GRBs).

GRB afterglow sample

GRBs are known tracers of the dense, star-forming regions of high-redshift galaxies. Their short-lived optical afterglows further enables detailed studies of the interstellar medium (ISM) of their hosts (e.g. [4]). In this work, we analyse a set of carefully selected bursts detected by the Neil Gehrels Swift Observatory (*Swift*) over the last decade as part the X-shooter GRB (XS-GRB) afterglow legacy survey [5]. The sample criteria are constructed such that the observed sample provides an unbiased representation of the underlying population of *Swift*-detected bursts, while simultaneously optimizing the observability. We consider all GRB afterglows suitable to measure the column densities of the H I Lyman- α and the C II* $\lambda 1335.7$ transitions, which results in a sample of 15 bursts at $z \sim 1.5 - 6.3$ from which we can derive the relative abundance between H I and C II* in absorption. Figure 1 presents an example of the absorption-line modelling for one of the GRB afterglows in the sample. For each bursts, we can further measure the gas-phase metallicity, corrected by the amount of metals depleted onto dust grains.

The [C II]-to-H I conversion factor

The line transition C II* $\lambda 1335.7$ observed in GRB absorption spectra arises from the $^2P_{3/2}$ level in the ground state of ionized carbon (C⁺). The population in this state gives rise to the [C II]–158 μm transition ($^2P_{3/2} - ^2P_{1/2}$). From the column density of this particular feature, N_{CII^*} , we can thus determine the equivalent line luminosity based on the spontaneous decay rate as $L_{[\text{CII}]}$ = $h\nu_{\text{ul}}A_{\text{ul}}N_{\text{CII}^*}$ in the line of sight, where $\nu_{\text{ul}} = 1900.5 \text{ GHz}$ and $A_{\text{ul}} = 2.4 \times 10^{-6} \text{ s}^{-1}$ for [C II]–158 μm . Similarly, we measure the line-of-sight H I column mass density $M_{\text{HI}} = m_{\text{HI}}N_{\text{HI}}$, with m_{HI} the mass of the H atom and N_{HI} the H I column density. From these two quantities, we derive

the relative [C II]-to-H I abundance ratio, $M_{\text{HI}}/L_{[\text{CII}]} = m_{\text{HI}}N_{\text{HI}}/h\nu_{\text{ul}}A_{\text{ul}}N_{\text{CII}^*}$, which we here denote $\beta_{[\text{CII}]}$. Assuming that the ratio of the derived column densities for each sightline is representative of the mean of the relative total population, $N_{\text{HI}}/L_{[\text{CII}]} = \Sigma_{\text{HI}}/\Sigma_{[\text{CII}]}$, the $\beta_{[\text{CII}]}$ calibration derived per unit column is equal to the global [C II]-to-H I conversion factor of the galaxy. This scaling is derived for each GRB in the sample and converted to solar units, M_{\odot}/L_{\odot} .

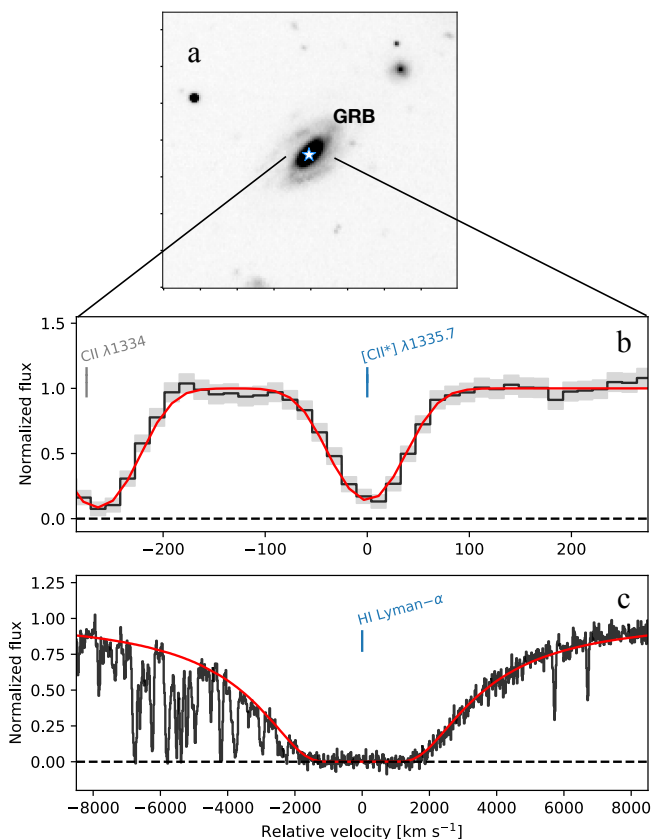


Figure 1: Illustration of GRBs as probes of the ISM in their hosts. Panel a shows the typical explosion sites of GRBs, and panels b and c show examples of absorption features from C II* $\lambda 1335.7$ and H I Lyman- α .

Figure 2 presents the $\beta_{[\text{CII}]}$ conversion factor derived for each GRB as a function of metallicity, including the best-fit scaling relation between the two. The $\beta_{[\text{CII}]}$ conversion factor is found to log-linearly scale with the metallicity, described by the following relation

$$\log(M_{\text{HI}}/L_{[\text{CII}]}) = (-0.87 \pm 0.09) \times \log(Z/Z_{\odot}) + 1.48 \pm 0.21 \quad (1)$$

where Z/Z_{\odot} is the relative solar abundance (with $12 + \log(\text{O}/\text{H}) = 8.69$ for $\log Z/Z_{\odot} = 0$), and M_{HI} and $L_{[\text{CII}]}$

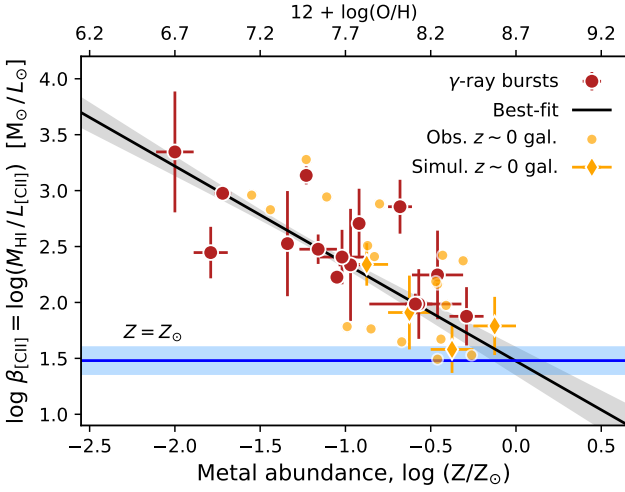


Figure 2: GRB absorption-line measurements of the relative [C II]-to-H I abundance ratio as a function of metallicity. The black solid line and gray shaded region represent the best-fit linear relation and associated uncertainty. Observations and simulations of galaxies at $z \approx 0$ are shown for comparison.

are in units of M_\odot and L_\odot , respectively. For comparison, the sample of galaxies at $z \sim 0$ from the *Herschel* Dwarf Galaxy Survey, for which [C II] luminosities and H I gas masses from direct 21-cm observations have been inferred [6], are shown as well, in addition to the average values of a set of simulated galaxies at the same epoch [7]. These theoretical predictions and the local galaxy sample are observed to match well with the empirical relation of $\beta_{[\text{C II}]}$ observed for the GRB sample at $z > 2$, indicating a strong universal connection.

Results

To infer the H I gas mass of high-redshift galaxies, we compile a set of galaxy samples from the literature surveyed for [C II] emission, for which we can apply the $\beta_{[\text{C II}]}$ conversion factor. For the compiled set of [C II]-emitting galaxies at $z = 2 - 6$ presented in Figure 3, we infer H I gas masses in the range of $M_{\text{HI}} = 3 \times 10^9 - 2 \times 10^{11} M_\odot$. At red-shifts $z \gtrsim 1$, all galaxies are observed to have H I gas masses in excess of their stellar mass M_* , reaching an average of $M_{\text{HI}}/M_* \approx 3$ at $z \approx 5$, contrasting the low H I content of nearby galaxies. This is the first indication that H I dominates the total ISM mass and baryonic matter content of galaxies at $z \approx 5$.

With the $\beta_{[\text{C II}]}$ conversion factor, we further make predictions for the cosmic H I gas mass density in galaxies, ρ_{HI} , at $z \approx 5$. Adopting the relevant [C II] luminosity function

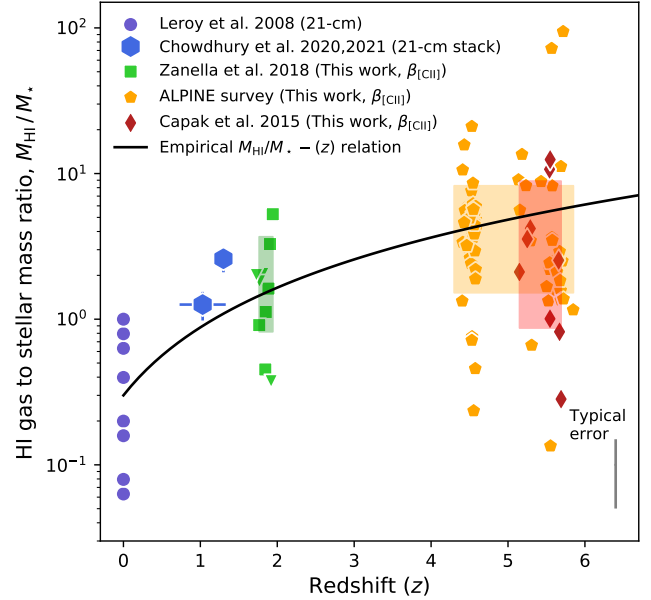


Figure 3: The H I gas mass excess, M_{HI}/M_* , of star-forming galaxies as a function of redshift. The galaxy samples surveyed for [C II] at $z \gtrsim 2$ are color-coded according to the specific reference they are adopted from. Colored boxes mark the 16th–84th confidence interval of M_{HI}/M_* for each sample.

at this redshift, we derive a [C II] luminosity density of $\mathcal{L}_{[\text{C II}]} = 2.8 \times 10^6 L_\odot \text{Mpc}^{-3}$. Assuming an average metallicity of $12 + \log(\text{O}/\text{H}) = 8.4$ (i.e., $\log(Z/Z_\odot) = -0.3$), we can convert this into ρ_{HI} using the $\beta_{[\text{C II}]}$ conversion factor, which yields $\rho_{\text{HI}} = 1.6^{+0.5}_{-0.4} \times 10^8 M_\odot \text{Mpc}^{-3}$ at $z \approx 5$. This estimate is in remarkable agreement with measurements of ρ_{HI} from damped Lyman- α absorbers (DLAs) at similar red-shifts (see [8] for a review).

We conclude that using [C II] as a proxy for H I, similar to how previous studies have relied on e.g. CO to infer the molecular content, is the current best alternative to probe the neutral atomic gas-phase in galaxies beyond the local Universe and out to the epoch of reionization.

References

- [1] Fernández, X., et al. 2016, *ApJL*, 824, L1
- [2] Blyth, S., et al. 2015, *Advancing Astrophysics with the Square Kilometre Array (AASKA14)*, 128
- [3] Heintz, K. E., et al. 2021, *ApJ*, 922, 147
- [4] Jakobsson, P., et al. 2004, *A&A*, 427, 785
- [5] Selsing, J., et al. 2019, *A&A*, 623, A92
- [6] Cormier, D., et al. 2015, *A&A*, 578, A53
- [7] Olsen, K. P., et al. 2021, *ApJ*, 922, 88
- [8] Péroux, C., & Howk, J. C., 2020, *ARA&A*, 58, 363

Short CV



2016: MSc in Astrophysics, Niels Bohr Institute, University of Copenhagen, Denmark
 2016–2019: PhD in Astrophysics, Science Institute, University of Iceland, Iceland
 2019–2022: Post-doctoral Fellow, University of Iceland, Iceland
 2022–present: Assistant Professor, Niels Bohr Institute, University of Copenhagen, Denmark

The impact of classical Cepheids' companions on the extragalactic distance scale

Paulina Karczmarek

Departamento de Astronomía, Universidad de Concepción, Avenida Esteban Iturra s/n, Casilla 160-C, Concepción, Chile

The extragalactic distance scale (also known as the cosmic distance ladder) is built up by a set of interlocked methods of distance determinations. Every method has its usefulness range and therefore must be calibrated with a preceding method in order to construct a homogeneous distance scale. For example, a large-distance method (e.g. Supernovae type Ia) has to be calibrated with a mid-distance method (e.g. classical Cepheids), and a mid-distance method with a short-distance method (e.g. parallax). Only then can the long-distance method be used to determine the Hubble constant: the value that holds the information about the age, size, content, and fate of our Universe, and that has recently been reported to be $H_0 = 73.04 \pm 1.04 \text{ km s}^{-1} \text{ Mpc}^{-1}$ [1]. The uncertainty on H_0 has accumulated from systematic and statistical errors associated with all the methods constituting previous rungs of the distance ladder, and can only be minimized by reducing these contributory errors.

Classical Cepheids in binary systems

Classical Cepheids (hereafter referred to as Cepheids) are the most famous mid-range distance indicators: they are abundant in the Milky Way (MW) and other galaxies, and the period-luminosity relation (PLR) they follow is considered universal and of superior accuracy to that offered by other types of radial pulsators. Still, the accuracy of the PLR can be improved with the better understanding of the factors that affect the intrinsic or apparent brightness of Cepheids, e.g. the effect of metallicity [2], or the effect of binarity [3]. Unlike the effect of metallicity, the effect of binarity has so far been only described in a qualitative way and lacked quantification.

The effect of binarity predicts that Cepheids with unresolved companions appear brighter than their single counterparts, due to the extra – and unaccounted for – light of their companions. Consequently, the PLR contaminated with binary Cepheids is *shifted upwards*, i.e. the zero point of the PLR moves towards more negative magnitudes, and as a consequence the distance measured using the PLR becomes smaller than its true value, and H_0 – larger.

$$\begin{aligned} \mu &\Rightarrow d = 10^{0.2(\mu+5)} \Rightarrow H_0 = v/d \\ \text{smaller} &\Rightarrow \text{smaller} \Rightarrow \text{larger} \end{aligned}$$

Theoretical and empirical studies agree that binary Cepheids constitute 60-80% of all MW Cepheids [e.g. 4, 5]; a similarly high percentage is expected in the Small and Large Magellanic Clouds (SMC, LMC, respectively.) However, up-to-date only about 6% of MW Cepheids, and less than 1% of LMC and SMC Cepheids are identified as binaries [6, and references therein]. This means that

the sample of binary Cepheids suffers from tremendous completeness bias, and renders impossible the estimation of the shift of the PLR due to Cepheids' companions from the observational data. This shift can, however, be estimated using synthetic data.

Synthetic population of binary Cepheids

A synthetic sample of binary Cepheids was created using a binary population synthesis code, *StarTrack*, which was designed to execute approximate evolution and binary interaction of 2×10^5 binary systems, and adjusted to classify as Cepheids stars that fulfill all the requirements of the filtering algorithm [6]. The resulting sample is free from the selection and completeness biases, and can be further subjected to statistical analysis. The effect of binaries is controlled by the *binarity percentage*, f_{bin} , which is a free parameter that can range from 0% (only single Cepheids) to 100% (only binary Cepheids.)

Synthetic single Cepheids accurately reproduce the slope of the PLR of the real Cepheids reported in the literature [see 6, their Tab. 2 and Fig. 6], while synthetic binary Cepheids accurately reproduce the “outliers” above the PLR, which are identified as binary Cepheids with giant companions [7]. Figure 3 shows the outliers and can be directly compared with Figure 3 from [7]. The agreement between real and synthetic data endorses the synthetic population of binary Cepheids as a reliable tool to investigate the effect of the Cepheids' companions on the PLR.

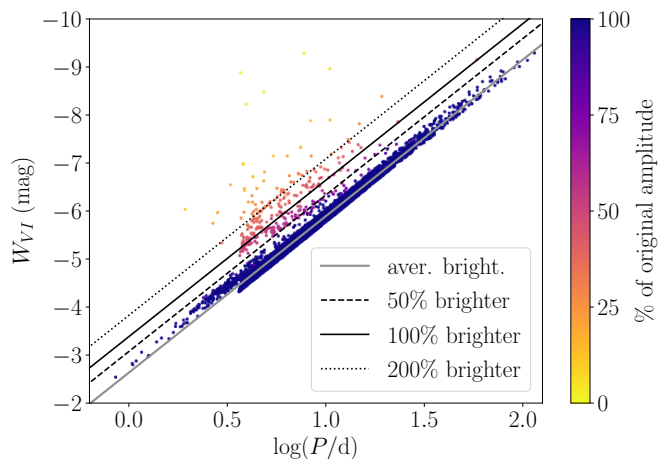


Figure 1: Period-luminosity relation for synthetic Cepheids in the LMC with $f_{\text{bin}} = 100\%$. Y-axis denotes the observed brightness in the Wesenheit index. Outliers (above 50% threshold) are binary Cepheids with giant companions, while the rest of binary Cepheids have main sequence stars as companions. Excerpted from [6].

Apart from the outliers, Figure 3 also shows binary Cepheids with main sequence companions (navy blue data points). Their contribution to the total brightness of individual systems seems negligible, since they all lie very close to the PLR. However, their cumulative brightness causes the PLR zero point to shift upwards. This shift scales linearly with the binarity percentage and is the largest in the visual domain (~ 0.05 mag for $f_{\text{bin}} = 100\%$) and the smallest in the near-infrared and the Wesenheit index ($\lesssim 0.01$ mag for $f_{\text{bin}} = 100\%$).

Implications for the extragalactic distance scale

In order to determine distance (more precisely, *distance modulus*, μ) from a reference galaxy (e.g. MW) to a target galaxy (e.g. LMC), one can simply calculate the difference between the zero points of the Cepheid PLRs in both galaxies. When calculating the distance modulus between two galaxies with unknown percentage of binary Cepheids, one needs to take into account three possibilities, depicted in Figure 1:

- (i) the reference (MW) and target (LMC) galaxies have only single Cepheids, resulting in the distance modulus μ_0 ,
- (ii) the reference galaxy has a larger binarity percentage than the target galaxy, resulting in $\mu_1 > \mu_0$,
- (iii) the reference galaxy has a smaller binarity percentage than the target galaxy, resulting in $\mu_2 < \mu_0$.

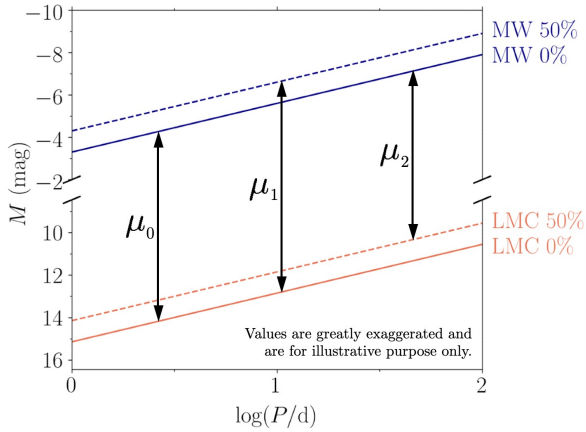


Figure 2: Visualization of three distance moduli (μ) between the Cepheid PLRs in the MW (navy blue) and the LMC (orange). μ_0 is the distance modulus between the PLRs constructed with single Cepheids only (solid lines). μ_1 and μ_2 show how distance moduli would change if the PLRs were constructed with 50% of binary Cepheids (dashed line). Values are greatly exaggerated and are for illustrative purpose only.

The shift in the distance modulus, $\Delta\mu$, is the difference between the distance modulus from the reference

to target galaxy, relative to μ_0 , i.e. $\Delta\mu = \mu - \mu_0$. Since binarity percentages for the reference and target galaxies do not have to be equal, $\Delta\mu$ can be either a positive or negative value. A grid of all possible $\Delta\mu$ values as a function of f_{bin} is shown in Figure 2. Two most extreme values in the top and bottom cells of the diagonal (0.002 and -0.003 mag, respectively) show the *maximum systematic error* of the distance modulus, i.e. the maximum value by which the distance modulus is shifted if the “assumed” binarity percentage is 0% while the “true” one is 100%, and vice versa. A full analysis for other passbands (BVIJHK and Wesenheit index) is beyond the scope of this paper and will be presented in the future (Karczmarek et al., in prep.)

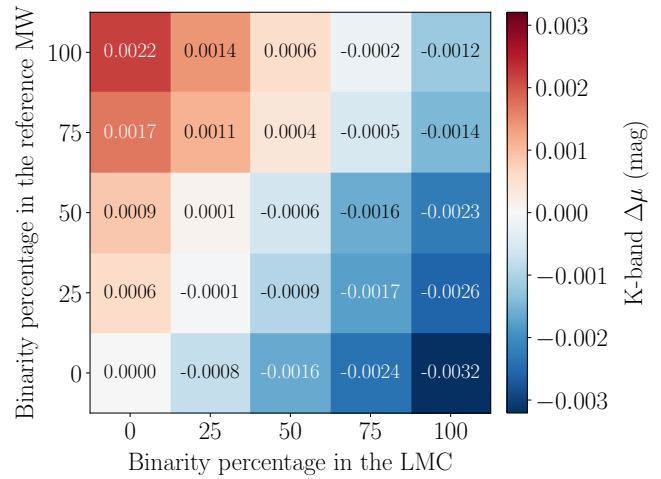


Figure 3: A grid of possible values of distance modulus shifts, $\Delta\mu$, as a function of binarity percentage in the reference and target galaxies, in the K-band.

The maximum systematic error of the distance modulus in the K-band due to binary Cepheids, $\Delta\mu_K = \pm 0.003$ mag, changes H_0 by only $0.025 \text{ km s}^{-1} \text{ Mpc}^{-1}$ (or 0.035%), which remains well within the 1σ uncertainty range of H_0 . This value indicates that the effect of Cepheid binarity in the K-band on the extragalactic distance scale and the Hubble constant is in fact negligible.

References

- [1] Riess, A., et al. 2021, arXiv:2112.04510
- [2] Breuval, L., 2021, Hypatia Colloquium: Early Career Astronomer series at ESO, 28, doi:10.5281/zenodo.5607445
- [3] Szabados, L., & Klagyivik, P. 2012, Ap&SS, 341, 99
- [4] Mor, R., et al. 2017, A&A, 599, A17
- [5] Kervella, P., et al. 2019, A&A, 623, A116
- [6] Karczmarek, P., et al. 2022, ApJ, 930, 65
- [7] Pilecki, B., et al. 2021, ApJ, 910, 118

Short CV



2006–2012: Master in Astronomy, Nicolaus Copernicus University, Toruń, Poland
 2012–2019: PhD in Astronomy, Astronomical Observatory of the University of Warsaw, Poland
 2019–present: Postdoctoral researcher, Universidad de Concepción, Chile

The Role of Powerful Radio Jets in the Host Galaxy of a Quasar in the First Gyr of the Universe

Sofía Rojas-Ruiz

Max-Planck-Institut für Astronomie, Königstuhl 17, D-69117, Heidelberg, Germany

High-redshift quasars can shed light on the co-evolution of central supermassive black holes and their host galaxies in the very early Universe. This can be tested by studying the first quasars within 1 Gyr after the Big Bang (or at redshift $z > 6$) emerging during the Epoch of Reionization [1]. Multiple studies searching for quasars during this epoch have shown a population of > 300 quasars with supermassive black hole masses ranging from $10^8 - 10^9 M_\odot$ (e.g., [2, 3]). However, only 10% of these quasars are bright at radio wavelengths [4]. The radio-loudness depends on the ratio of the brightness of the source at rest-frame optical and radio emission using the following definitions $R_{4400} = f_{\nu, 5 \text{ GHz}} / f_{\nu, 4400} > 10$ [5] or $R_{2500} = f_{\nu, 5 \text{ GHz}} / f_{\nu, 2500 \text{ \AA}} > 10$ [6]. In order to understand why the high-redshift radio-loud population fraction is much lower, it is necessary to make comparative studies with the radio-quiet population. The following research presents the first attempt at investigating the host galaxies of a radio-loud quasar in the rest-frame Far-Infrared and observe whether there are indications of the jet affecting the cold dust from the galaxy [see also 7].

We investigate quasar P352–15 near the end of Reionization at $z = 5.832 \pm 0.001$ and one of the most powerful radio sources with $R_{4400} \& R_{2500} > 1,000$ [8]. High-resolution VLBA imaging of the quasar (Figure 1) reveals radio hot spots indicating evidence of a kpc-scale radio jet (~ 1.6 kpc) at this high redshift [9]. This makes P352–15 the ideal laboratory to study for the first time the influence of jets in the host galaxy and also the timescales for black hole accretion and jet launch.

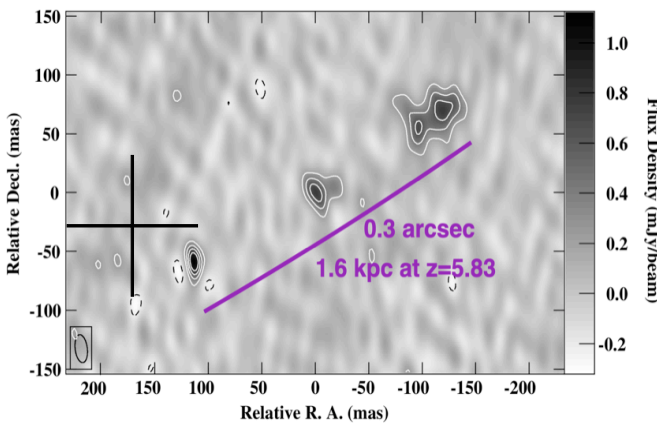


Figure 1: VLBA high-resolution image of P352–15. The black cross is centered at the quasar optical position: R.A. (J2000) = $23^{\text{h}}29^{\text{m}}36^{\text{s}}.8363$, DEC. (J2000) = $-15^{\circ}20'14''.460$. The extent among the hot spots is $0''.3$, corresponding to 1.62 kpc at $z = 5.83$. Figure adapted (See [9]).

The SED in rest-frame FIR and Radio Emission

We study the spectral energy distribution of this quasar at millimeter (far-infrared in the rest-frame) and radio observations. The millimeter continuum emission for radio-quiet quasars at these redshifts has usually been interpreted as cold dust and is modeled as a modified black body (MBB) [10]. This model depends on the temperature of the cold dust (T) and an emissivity spectral index (β) that describes e.g. the size of dust grains. Typical values in the literature of radio-quiet quasars assume $T = 30 \text{ K} - 100 \text{ K}$, and $\beta = 1.6$ or 1.95 (e.g., [11, 12]). We use two mm-continuum measurements of P352–15 from ALMA 290 GHz and NOEMA 100 GHz observations to fit the MBB. However, the analysis shows that it is not possible to model these millimeter measurements as cold dust alone, see Figure 2. The emission at 100 GHz is an order of magnitude higher than the one predicted by any of the MBB models. Therefore at this frequency we are observing emission from another source, the next suspect being synchrotron emission.

The radio emission observed in the SED is produced by the jets, more specifically by synchrotron emission generated from relativistic electrons spiralling around the magnetic field produced from the accreting black hole. The synchrotron radiation is well described as a simple power law of the form $S_\nu \propto \nu^\alpha$, where S_ν is the observed flux density at the frequency ν and α is the radio spectral index. P352–15 has radio observations with GMRT at 215 MHz, and with the VLA at 1.4 GHz and 3 GHz. Using these measurements it is possible to calculate spectral index $\alpha_3^{0.215} = -0.88$. However, when extrapolating this slope to the millimeter measurements, the synchrotron emission at 100 GHz is about three times brighter than the observed with NOEMA (Figure 2). This suggests evidence of the strong synchrotron emission in P352–15 affecting the dust-dominated continuum emission. Furthermore, this implies a break in the synchrotron spectrum.

Timescale for Jet Aging

Finding the frequency at which the power-law from synchrotron emission breaks is crucial to calculate spectral aging of the jet. This steepening occurs because the higher energy electrons lose energy faster ($rate \propto E^2$) and as they cool down from recent re-acceleration in the jet caused by shocks, this steepening effect is seen at the higher frequencies (see yellow arrows in Figure 2). Synchrotron aging t_{syn} thus depends on the magnetic field strength B and frequency break ν_b [13]. For the case of P352–15, the analysis of high-resolution VLBA observations presents a powerful magnetic field of $B \sim 3.5 \text{ mG}$

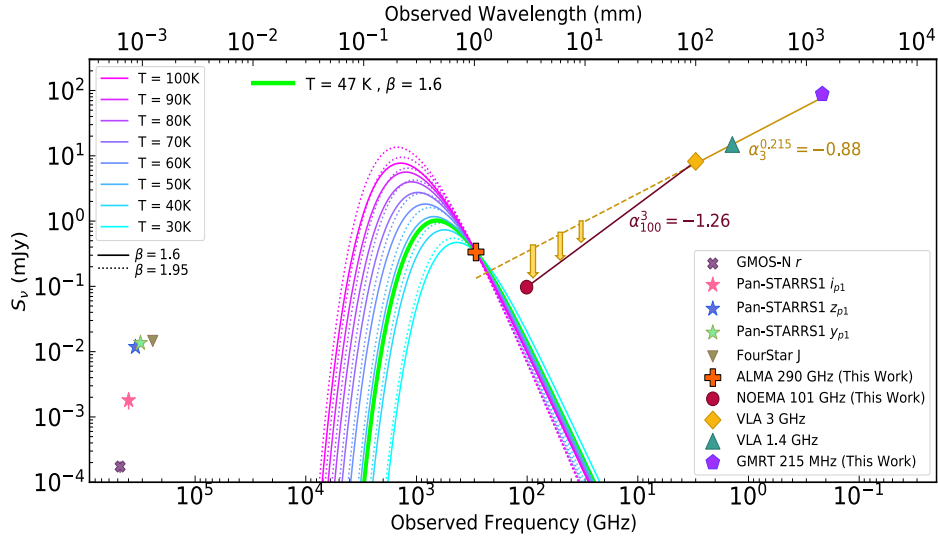


Figure 2: Spectral energy distribution (SED) of P352–15, adapted from [8]. The millimeter ALMA and NOEMA measurements are inconsistent with a MBB modeled at different dust temperatures and dust emissivity spectral indexes. The radio data at 215 MHz–3 GHz are well described by synchrotron emission. However, extrapolating that power law (dashed line) would be inconsistent with the millimeter data. To explain this SED, the synchrotron emission must steepen or break at high frequencies as denoted by the yellow arrows.

[9]. The missing ingredient is the frequency break ν_b , for which we have performed VLA observations (PI: Rojas-Ruiz) in all available bands from 1.5 GHz – 45 GHz and are currently under analysis.

Timescale for Black Hole Accretion

The surrounding neutral intergalactic medium (IGM) of a quasar in the Epoch of Reionization begins to be ionized by UV radiation produced from the supermassive black hole (SMBH) accretion. It is therefore possible to calculate the timescale for quasar activity t_Q by measuring the size of the ionizing bubble (e.g., [14, 15]). A bigger bubble implies that the SMBH has been accreting for longer time and there is more flux transmission blueward of the Ly- α . We are analyzing available X-Shooter spectra of P352–15 covering the rest-frame UV/Optical emission showing this flux enhancement. Therefore, we will be able to constrain t_Q and compare this timescale to that of the jet from synchrotron aging t_{syn} . We would thus be able to discern among the possible scenarios presented in Figure 3 where a) the jet is launched soon after the SMBH turns on, b) the jet takes a longer time to form after the SMBH begins accreting, or c) the SMBH has intermittent accretion allowing time for IGM recombination but the jet from earlier activity is still present. The future timescale studies of P352–15 will be a pioneering work on understanding better the black hole – host galaxy formation and jet ejection mechanisms for quasars within the first Gyr of the Universe.

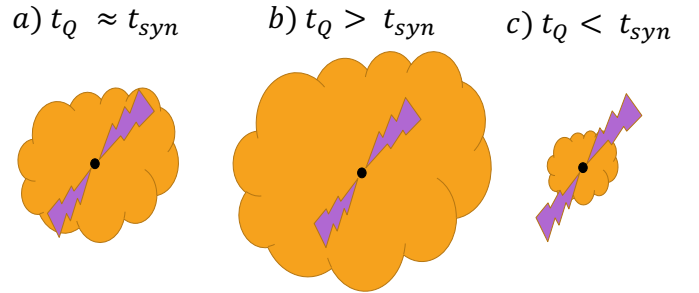


Figure 3: Scenarios of the possible comparison timescales between black hole accretion (black circle) determined by t_Q (orange bubble growth) and jet launch t_{syn} (purple jet growth).

References

- [1] Fan, X., et al. 2006, AJ, 132, 17
- [2] Bañados, E., et al. 2016, ApJS, 227, 11
- [3] Wang, F., et al. 2019, ApJ, 884, 30
- [4] Bañados, E., et al. 2018, ApJ, 861, L14
- [5] Sramek, R. A., & Weedman, D. W. 1980, ApJ, 238, 435
- [6] Kellermann, K. I., et al. 1989, AJ, 98, 1195
- [7] Khusanova, Y., et al. 2022, A&A, 664, A39
- [8] Rojas-Ruiz, S., et al. 2021, ApJ, 920, 150
- [9] Momjian, E., et al. 2018, ApJ, 861, 86
- [10] Beelen, A., et al. 2006, ApJ, 642, 8
- [11] Priddey, R. S., & McMahon, R. G. 2001, MNRAS, 324, L17
- [12] Venemans, B. P., et al. 2016, ApJ, 816, 37
- [13] Carilli, C. L., et al. 1991, ApJ, 861, 86
- [14] Eilers, A. C., et al. 2017, ApJ, 840, 24
- [15] Davies, F. B., et al. 2019, ApJ, 884, 19

Short CV



2015–2019: B.S. Astronomy & B.S. Physics, The University of Texas at Austin, USA
 2019–present: PhD IMPRS Fellow, Max-Planck-Institut für Astronomie, Germany

The dust temperature REBELS

Laura Sommovigo

Scuola Normale Superiore, Piazza dei Cavalieri 7, I-56126 Pisa, Italy

The Atacama Large Millimeter Array (ALMA) recently opened a new window on the rest-frame far-infrared (FIR) emission of the first generations of galaxies, dramatically improving our understanding of the dust build-up in the early Universe. Dust grains shape the galaxies Spectral Energy Distributions (SEDs), by absorbing the stellar ultraviolet (UV) and optical radiation, and thermally re-emitting at infrared wavelengths. Dust FIR emission is typically modelled as a single-temperature grey-body emission [9, 6, 2], which is characterised mainly by the dust temperature T_d and the dust mass M_d .

ALMA observations have unveiled the presence of large dust masses in galaxies at the Epoch of Reionization (EoR), up to $M_d > 10^7 M_\odot$ as early as $z \sim 8$ [24, 15, 5]. Such large dust masses at these early epochs are in tension with theoretical dust production constraints, resulting in the so called “dust budget crisis”. However, these inferred dust masses are heavily dependent on the cold dust temperatures ($T_d < 40$ K) assumed in high- z galaxies FIR SED-fitting procedure. Most FIR continuum observations at $z > 4$ probe a narrow wavelength range far from the emission peak, where different grey-body curves are hard to discriminate. Thus, a value for T_d is often assumed a priori in the SED fitting procedure. This issue is exacerbated in ALMA large surveys at high- z , ALPINE ($z = 4 - 6$, [17]) and REBELS ($z = 6 - 9$, [8]), where only a single continuum data point (at rest-frame $158 \mu\text{m}$, underlying the [CII] emission line) is available for each target. Due to the lack of constraints on T_d , all the quantities inferred from SED fitting, namely M_d , the IR luminosity L_{IR} and the dust-obscured SFR SFR_{IR} , are highly uncertain.

A new method to derive the dust temperature

In [22] we proposed a novel method to derive the dust temperature in galaxies relying on a single measurement, by combining the [CII] line emission with the underlying continuum flux at rest-frame 1900 GHz. We use the [CII] luminosity, L_{CII} , as a proxy for the total gas mass M_g . Then for a given a dust-to-gas ratio D , $M_d = D \alpha_{\text{CII}} L_{\text{CII}}$, where α_{CII} is the [CII]-to-total gas conversion factor. We derive an analytic expression for α_{CII} using empirical relations such as the Kennicutt–Schmidt relation [14], and the De Looze relation between L_{CII} –SFR [11]. Armed with an expression for M_d and α_{CII} , we derive T_d from the continuum flux at 1900 GHz.

Application to REBELS galaxies

Our method can be exploited in the context of recent ALMA large programs targeting [CII] emitters at $z > 5$, such as the “Reionization Era Bright Emission Line Survey” (REBELS; PI: Bouwens, [8]). REBELS studied 40 of the UV-brightest ($-21.3 < M_{\text{UV}} < -22.5$) known galaxies at $z = 6.5 - 7.7$, identified over a 7 deg^2 area of the sky, systematically scanning for bright ISM-cooling lines [CII] $158 \mu\text{m}$ and [OIII] $88 \mu\text{m}$ and dust-continuum

emission. We apply our method to the 13 REBELS targets detected both in continuum (3σ) and in [CII] (5σ) at $z \sim 7$. These sources constitute the first statistical sample of continuum detected star-forming galaxies at the EoR. Their ALMA images [13] and FIR SEDs, derived with our method, are shown in Figure 1.

We find that the dust temperatures of REBELS galaxies vary in the range $39 - 58$ K and the dust masses are in the narrow range $(0.9 - 3.6) \times 10^7 M_\odot$. Dust production from SNe alone in most cases (85%) can generate such dust masses assuming a dust yield $< 1 M_\odot$ per SN [18, 10, 12].

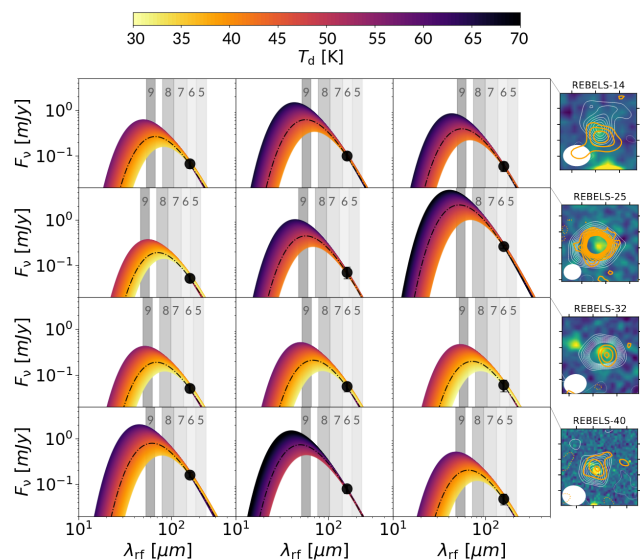


Figure 1: FIR SEDs of the REBELS sources shown in the upper panel. The SEDs are colour coded according to the corresponding dust temperatures (see colorbar). The dashed black curves show the SEDs obtained with the median (T_d , M_d) values for each galaxy. The black points represent the continuum observations at 1900 GHz. The grey area represent ALMA bands 5-9. We also show the dust continuum (orange) and [CII] emission maps (white) of 4 REBELS galaxies. The background images ($5'' \times 5''$) are the stacked JHK-band images. The contours start from 2σ in steps of 1σ of the background standard deviation. The white ellipses represent the beam.

The cosmic dust temperature evolution after REBELS

In the last few years several works spanning the redshift range $0 \leq z < 10$ have suggested the presence of a direct correlation between T_d and redshift. Combining the few available dust temperature estimates for individual galaxies at $z > 5$ with stacking results, different works came to discrepant conclusions (see inset panel in Figure 2). Some works suggest a steeply increasing $T_d - z$ trend (linear [21, 7] or quadratic [25]), while others predict a much milder evolution, with a substantial flattening at $z > 4$ [20, 19].

Our analysis of the REBELS sample can clarify this issue in a unique way since REBELS continuum detections

double the number of previously known sources at $z > 5$, and different $T_d - z$ trends are more robustly identified at the higher- z of the REBELS sample (see inset panel in Figure 2). Extrapolating the reported linear $T_d - z$ relation [21, 7] to $z = 7$ gives $T_d \sim 56$ K, a slightly warmer temperature than REBELS galaxies, for which on average we find $T_d \sim 47$ K. REBELS galaxies average dust temperature is in turn warmer than the ones inferred by [20, 19], which are as low as $T_d \sim 39$ K at $z = 7$. The largest discrepancy is with the preliminary results by [25], which suggest a sharp increase in T_d at $z > 5$ reaching $T_d \sim 87$ K at $z = 7$.

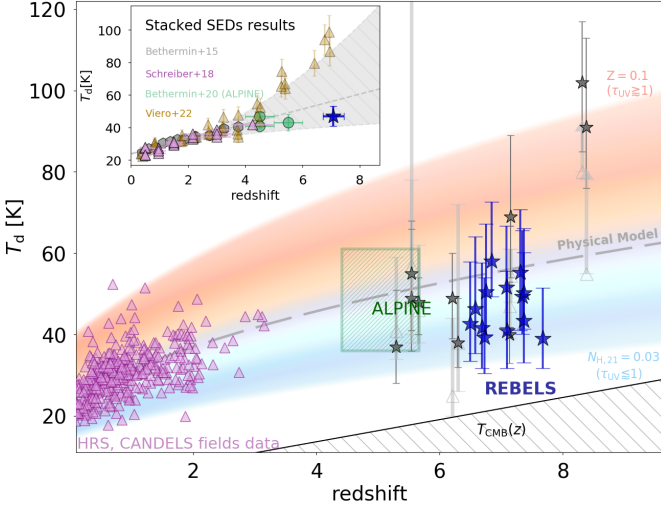


Figure 2: Main panel: Dust temperature T_d as a function of redshift for star-forming galaxies in the range $z = 0 - 8$. The purple triangles represent the star forming galaxies detected in the HRS and CANDELS fields studied in [21]. The grey points show the individual UV-selected galaxies at $z > 5$ for which T_d estimates are available in the literature. In green and blue we show the results obtained with our method for individual ALPINE and REBELS galaxies, respectively. The coloured region and grey dashed line show the T_d -redshift evolution predicted by our physical model (for an increasing effective UV optical depth τ_{UV} from blue to red), see eq. 1. **Inset panel:** T_d values obtained from stacked SEDs fitting in the redshift range $0 < z < 9$ (grey, purple, green and yellow points, from [21, 4, 25], respectively). The grey hatched area and dashed lines show the empirical $T_d - z$ trends derived in different works (from bottom to top, [19, 21, 25]). The blue star corresponds to the average temperature derived here for REBELS galaxies.

We stress that none of the aforementioned empirical $T_d - z$ trends are explained by theory. To address this issue, in [23] we produce a new model aimed at physically motivating the cosmic evolution of the dust temperature. We find that T_d anti-correlates with the *total* gas depletion time $t_{dep} = M_g / \text{SFR}$, as:

$$T_d = 29.7 \left[\frac{(1 - e^{-\tau_{UV}})}{Z} \left(\frac{\text{Gyr}}{t_{dep}} \right) \right]^{1/6} \text{K}, \quad (1)$$

where τ_{UV} is the galaxy effective dust optical depth at rest-frame 1500 \AA (and Z is the metallicity in solar units). The total gas depletion times decreases at high- z due to the higher cosmological accretion rate at early epochs, $t_{dep} \propto (1 + z)^{5/2}$. Thus, we predict mild increase of T_d with redshift as $T_d \propto t_{dep}^{-1/6} \propto (1 + z)^{0.42}$. On top of this $T_d - z$ trend, we can motivate the scatter in the measured T_d values at a given redshift. In UV-transparent galaxies ($\tau_{UV} \ll 1$) the scatter in T_d depends solely on the column density, $N_H \sim 10^{21} \tau_{UV} / Z \text{ cm}^{-2}$, with larger N_H corresponding to warmer dust temperatures due to the more efficient dust heating. Instead, in UV-obscured galaxies ($\tau_{UV} \gg 1$) the scatter in T_d depends only on the metallicity Z , with lower Z implying warmer dust. This follows from our assumption that the dust-to-gas ratio scales linearly with Z ; then for a given UV field a lower metallicity implies that less dust is exposed to the UV emission, thus being more efficiently heated.

Figure 2 shows that our predictions are in perfect agreement with data, both in terms of the measured increasing $T_d - z$ trend and the observed scatter at each given epoch. Our physical model further indicates that large $\tau_{UV} > 1$ combined with low metallicities $Z/Z_\odot < 0.3$ can explain the very hot dust temperatures ($T_d > 80$ K) found in some $z \sim 8$ galaxies [3, 1, 16].

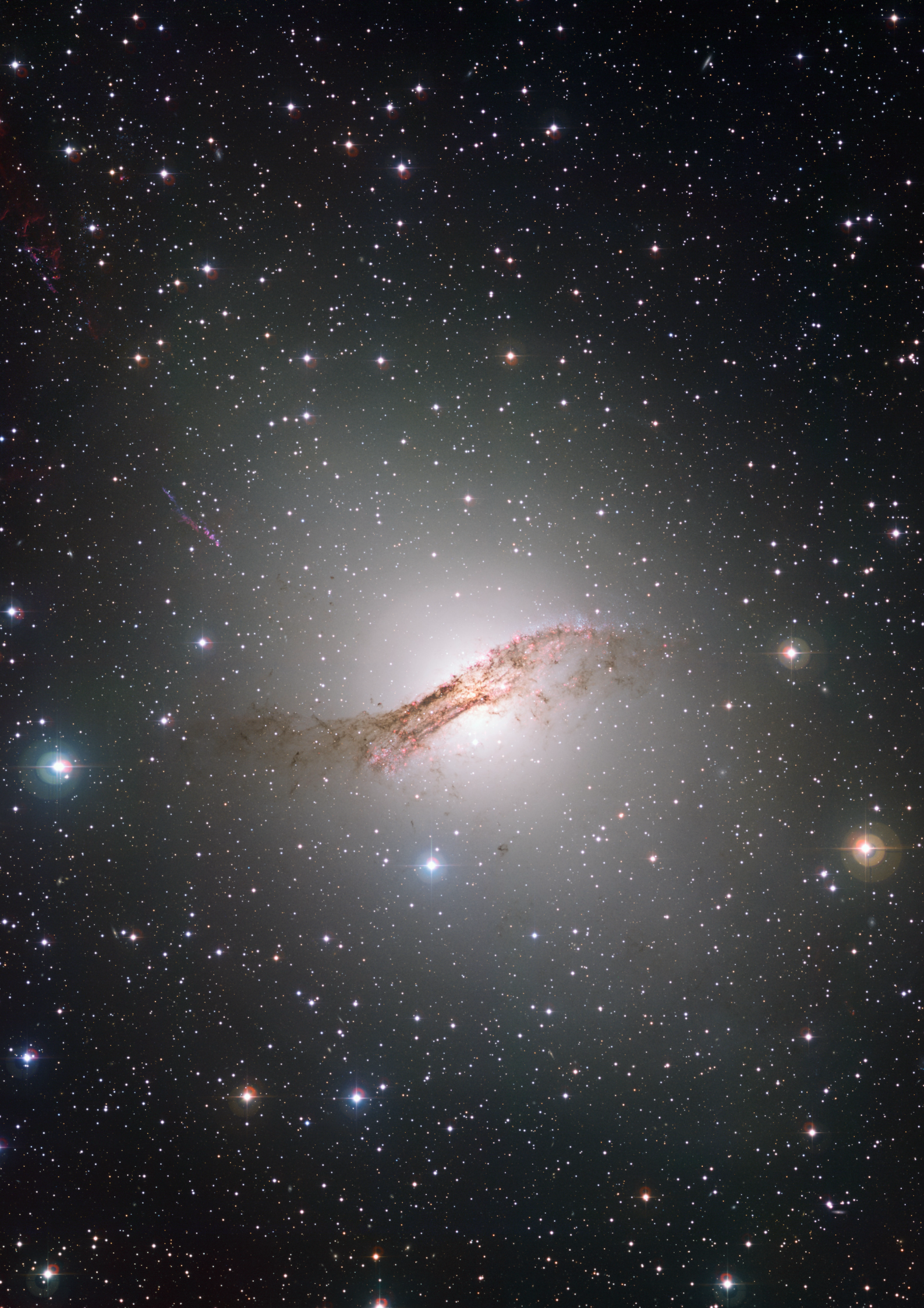
References

- [1] Bakx, T., et al., 2020, MNRAS, 493, 4294
- [2] Barisic, I., et al., 2017, ApJ, 845, 41
- [3] Behrens, C., et al., 2018, MNRAS, 477, 552
- [4] Bethersin, M., et al., 2020, p.arXiv:2002.00962
- [5] Bowler, R. A. A., et al., 2020, MNRAS, 493, 2059
- [6] Bouwens, R., et al., 2016, ApJ, 833, 72
- [7] Bouwens, R., et al., 2020, ApJ, 902, 112
- [8] Bouwens, R., et al., 2021, eprint arXiv:2106.13719
- [9] Capak, P. L., et al., 2015, Nature, 522, 455
- [10] Dayal, P., et al., 2022, MNRAS, 512, 989
- [11] De Looze, I., et al., 2014, A&A, 568, A62
- [12] Ferrara, A., et al., 2022, MNRAS, 512, 58
- [13] Inami et al., 2022, arXiv:2203.15136
- [14] Kennicutt, R. C. J., 1998, ApJ, 498, 541
- [15] Laporte, N., et al. 2017, ApJ, 837, 21
- [16] Laporte et al., 2019, MNRAS, 487, 81
- [17] Le Fevre, O., et al., 2020, A&A, 643, A1
- [18] Lesniewska, A., & Michalowski, M. J., 2019, A&A, 624, L13
- [19] Liang, L., et al., 2019, MNRAS, 489, 1397
- [20] Magnelli, B., et al., 2014, A&A, 561, A86
- [21] Schreiber, C., et al., 2018, A&A, 609, A30
- [22] Sommovigo, L., et al. 2021, MNRAS, 503, 4878
- [23] Sommovigo, L., et al., 2022, MNRAS, 513, 3122
- [24] Tamura, Y., et al., 2019, ApJ, 874, 27
- [25] Viero, M., et al., 2022, arXiv:2203.14312

Short CV



2016-2018: Master in Astronomy, University of Pisa, Italy
 2018-present: PhD in Astronomy, Scuola Normale Superiore, Italy



GALAXIES AND GALACTIC NUCLEI

X-ray blasts from awakening massive black holes

Riccardo Arcodia

Max Planck Institute for Extraterrestrial Physics, Giessenbachstrasse 1, 85748 Garching bei Muenchen

Typical X-ray active galactic nuclei are known to vary on both short (hours) and long (years) timescales. However, the so-called X-ray quasi-periodic eruptions (QPEs), discovered in late 2018 [1], are surely an exotic and novel entry in the catalog of X-ray emitting sources. QPEs are X-ray bursts repeating every few hours in a quasi-periodic fashion, with a flux increase of more than one order of magnitude over a quiescence level (see Figure 1). QPEs have been found so far only in a handful of sources [1, 2, 3, 4].

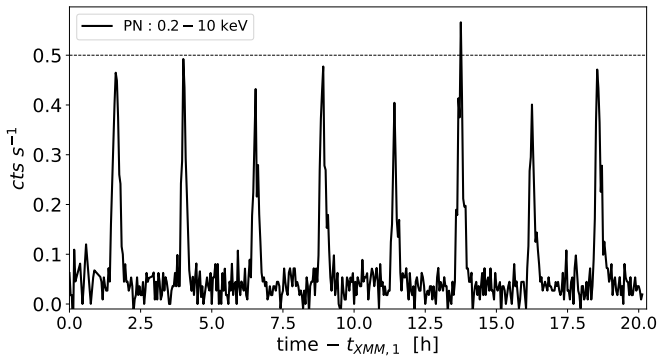


Figure 1: X-ray light curve of the QPE source eRO-QPE2, adapted from [3].

QPEs' observational properties

QPEs have so far been associated with nearby ($z \sim 0.02 - 0.05$) galaxies with stellar masses of $M_{star} \approx 1 - 3 \times 10^9 M_{\odot}$ [3]. Their optical spectra lack broad emission lines and no infrared photometry excess, associated with the dusty environment typical of active galactic nuclei, is observed [1, 2, 3]. However, narrow lines in the optical spectra suggest the presence of an ionizing source, weak in some QPE hosts, in addition to star formation [5]. These galaxies host massive black holes of $M_{BH} \approx 10^{5-7} M_{\odot}$ [5], a range which is intriguingly close to the elusive black hole population with intermediate mass [6]. Therefore, QPEs might provide a new channel to activate the nuclei of low-mass galaxies through transient accretion events, which is still a poorly studied regime in the black hole-galaxy co-evolution history [7].

The average recurrence time between consecutive eruptions in the X-ray light curve spans, from source to source (see Figure 1 for one example), within $\sim 2.5 - 18.5$ h, while the average duration of the eruptions is observed to be $\sim 0.5 - 7.0$ h [3]. The emission in quiescence (i.e. excluding the eruptions) is very soft (most observed X-ray signal below ~ 1 keV) and as bright as $0.3 - 1.6 \times 10^{41}$ erg s^{-1} between $0.5 - 2.0$ keV. At their peak the emission spectrum is harder, but still overall soft

(most observed X-ray signal below $\sim 2 - 2.5$ keV) and QPEs are as bright as $L_{0.5-2.0 \text{ keV}} \approx 10^{42} - 10^{43}$ erg s^{-1} . Given the QPEs' black hole mass estimates [5], this suggests that they are close to being Eddington-limited.

Finding QPEs with eROSITA

QPEs have so far been discovered only through X-rays. Some of them have been found either serendipitously [1] or through dedicated searches in X-ray observations archives [2, 4]. The eROSITA X-ray telescope [8] currently provides the only blind and systematic way to find more QPEs as they happen [3]. eROSITA started the first of eight all-sky surveys (eRASS1-8) on 13 December 2019. In each survey, completed in six months, every point of the sky is observed for ~ 40 s every ~ 4 h with the number of times (typically a few) varying with the location in the sky, increasing towards high ecliptic latitudes [8]. A QPE candidate is found if an extragalactic source shows recurrent high-amplitude variability (see Figure 2 for an example), although follow-up with other X-ray instruments is needed given eROSITA's observational cadence and sampling (e.g. Figure 1 for the same source shown in Figure 2). In the first year of eROSITA operations two QPEs were found with this method [3] and similar rates are expected for the future.

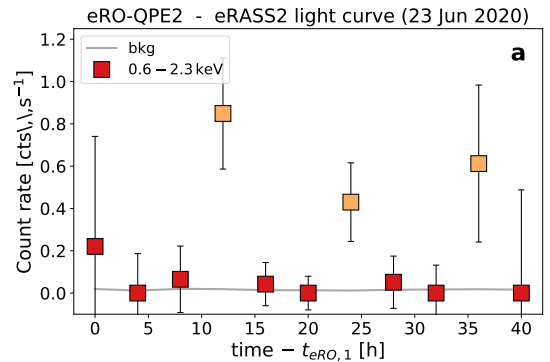


Figure 2: eROSITA X-ray light curve (with red and orange high-lighting faint and bright observations, respectively) of the QPE source eRO-QPE2, of which a continuous follow-up observation is shown in Figure 1. Reported from [3].

The origin of QPEs

The origin of QPEs is still open and debated. However, QPEs' X-ray properties are inconsistent with current models of radiation-pressure instabilities in an isolated accretion disk [3], although dedicated simulations will need to be performed in the future. Similarly, QPEs' multi-wavelength observational properties rule out a binary of massive black holes with mass-ratio close to unity [3]. Recently, models based on a massive black hole and

at least one stellar-mass companion have gained significant attention [9, 10, 11, 12, 13], a scenario often referred to as extreme mass-ratio in spiral (EMRI). EMRI scenarios for QPEs are qualitatively consistent with their multi-wavelength properties. First, QPEs' hosts are low-mass galaxies with massive black holes [3, 5], where nuclear star clusters are expected to be nearly ubiquitous [14], which is confirmed for at least two QPE sources [1, 15]. Second, QPEs have a high-incidence in young post-starburst galaxies [5]. Both these ingredients make a galactic nucleus prone to EMRI-like events [14]. These models are also able to reproduce the average periodicity and luminosity of QPEs. However, quantitative comparisons including a physical model for the X-ray emission still need to be performed.

Interestingly, EMRIs also emit gravitational wave signals detectable by future-generation instruments like LISA and Tianqin [13], although it is still unclear whether the same EMRI can be observed by both electromagnetic and gravitational waves detectors [16]. If confirmed, this would surely revolutionize the future of multi-messenger astronomy.

QPEs are more complicated than it seems

Models have so far been compared to QPEs observations only qualitatively, also because QPEs were initially considered as somewhat orderly pulses with a small scatter in the arrival times. However, performing follow-up on known QPE sources after months or even years helped to mount evidence of more complicated behavior. For instance, QPEs can disappear within a few years [4], which puts strong constraints on their duration, incredibly short compared to the lifetime of a galactic nucleus. Furthermore, a more thorough analysis on the X-ray properties of QPE sources is revealing that their time evolution is far more complex than a simple "quasi-periodicity" [17]. In [17] a tentative separation in two sub-classes of QPEs has been suggested. As a matter of fact, in two sources (namely GSN 069 and eRO-QPE2, [1, 3]), long and short recurrence times, as well as relatively stronger and weaker bursts, alternate [11, 17]. In other two sources (namely RX J1301.9+2747 and eRO-QPE1, [2, 3]) the timing properties can be complex and irregular: the scatter on arrival times is so high that the question as to whether there is a periodicity at all rises ([18]); and at times QPEs do not appear as isolated pulses, but rather as a chaotic mixture of bursts with different amplitudes overlapping in time [17]. An example of this is shown in Figure 3 for the source eRO-QPE1 [17].

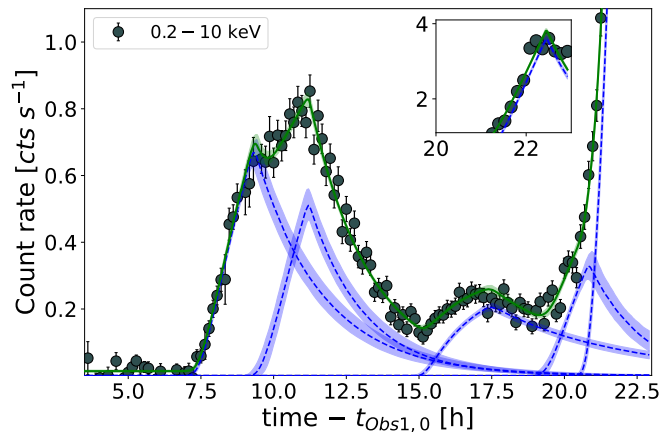


Figure 3: X-ray light curve of the QPE source eRO-QPE1, adapted from [17]. The source underwent a very complex cycle with a chaotic mixture of bursts with different amplitude and overlapping in time (each shown in blue, while the total fit in green).

It is still early days, as this research field effectively started in 2019, but QPEs are surely the new frontier to study variable accretion onto massive black holes. Observations are revealing more and more details and models are being put forward at a fast pace. For the near future, new QPEs can be found with eROSITA and science teams of planned or proposed X-ray missions are investigating whether their instruments can be used to find and/or study QPEs. In the meantime, these questions remain unanswered: what are QPEs and how do they awake massive black holes in galactic nuclei?

References

- [1] Miniutti, G., et al. 2019, *Nature*, 573, 381
- [2] Giustini, M., et al. 2020, *A&A*, 636, L2
- [3] Arcodia, R., et al. 2021, *Nature*, 592, 704
- [4] Chakraborty, J., et al. 2021, *ApJL*, 921, L40
- [5] Wevers, T., et al. 2022, *A&A*, 659, L2
- [6] Greene, J., et al. 2020, *ARA&A*, 58
- [7] Reines, A. & Volonteri, M. 2015, *ApJ*, 813, 82
- [8] Predehl, P., et al. 2021, *MNRAS*, 493, L120
- [9] King, A. 2020, *ApJ*, 917, 43
- [10] Sukova, P., et al. 2021, *ApJ*, 917, 43
- [11] Xian, J., et al. 2021, *ApJL*, 921, L32
- [12] Metzger, B., et al. 2022, *ApJ*, 926, 101
- [13] Zhao, Z. Y., et al. 2022, *A&A*, 661, A55
- [14] Neumayer, N., et al. 2020, *A&ARv*, 28
- [15] Shu, X. W., et al. 2017, *ApJ*, 837, 3
- [16] Chen, X., et al. 2021, arXiv:2112.03408
- [17] Arcodia, R., et al. 2022, arXiv:2203.11939
- [18] Giustini, M., et al., in prep.

Short CV



2012–2015: BSc in Physics at Univ. of Milan-Bicocca, Italy
 2015–2017: MSc in Astrophysics and Space Physics at Univ. of Milan-Bicocca, Italy
 2017–2021: PhD at MPE, Garching, Germany
 2021–present: Postdoctoral researcher at MPE, Garching, Germany

An observed link between spin-filament alignment flips and bulge formation

Stefania Barsanti

Research School of Astronomy and Astrophysics, Australian National University, Canberra ACT, Australia
ARC Centre of Excellence for All Sky Astrophysics in 3 Dimensions (ASTRO 3D), Australia

The study of the interplay between galaxy angular momentum and structures in the cosmic web is a powerful tool to constrain galaxy evolution scenarios. We study the alignments of galaxies' spin axes with respect to nearby cosmic web filaments as a function of various properties of the galaxies and their constituent bulges and discs [1]. We exploit the SAMI Galaxy Survey to identify 3D spin axes from spatially-resolved stellar kinematics and to decompose galaxies into their kinematic bulge and disc components. The GAMA redshift survey is used to reconstruct the surrounding cosmic filaments. The mass of the bulge is found to be the primary parameter of correlation with spin-filament alignments: galaxies with lower bulge masses tend to have their spins parallel to the closest filament, while galaxies with higher bulge masses are more perpendicularly aligned. Other galaxy properties, such as visual morphology, stellar age, star formation activity, kinematic parameters and local environment, show secondary correlations. The observational link between bulge growth and flipping of spin-filament alignments from parallel to perpendicular can be explained by mergers, which can drive both alignment flips and bulge formation. The separate study of bulge and disc spin-filament alignments reveals additional clues about the formation pathways of these galaxy components: bulges tend to have more perpendicular alignments, suggesting they are merger products, while discs show different tendencies according to the mass of the associated bulge, pointing to multiple formation scenarios. To our knowledge, this is the first time that such a study has been conducted using observations rather than simulations.

The puzzle of galaxy formation

Understanding how galaxies acquire their angular momentum in the cosmic web is crucial to complete the puzzle of galaxy formation. Large-scale cosmological hydrodynamical simulations predict that the alignment of the galaxy spin axis with respect to the orientation of the filament within which it resides depends on the stellar mass [2, 3]: low-mass galaxies tend to have spins aligned parallel with the closest filament, while the spins of high-mass galaxies are more perpendicular to the filament. Only recently has this mass-dependent trend been detected in the observations [4]. Since mergers are found to be mainly responsible for the flipping of the spin-filament alignments [5], it is interesting to ask whether we can detect a correlation between bulge properties and the alignments in the observations.

Galaxy sample and measurements

To identify the orientation of the spin axis of a galaxy,

we take advantage of spatially-resolved stellar kinematics from the SAMI Galaxy Survey, an integral field spectroscopic survey of more than 3000 galaxies with stellar mass range $8 < \log(M_*/M_\odot) < 12$ and redshift range $0.004 < z \leq 0.115$ [6]. We measure the stellar kinematic position angles (PA) and follow the 3D thin-disc approximation method [7]. To disentangle the spin axes of bulges and discs, we take advantage of the 2D kinematic bulge/disc decomposition [8]. Figure 1 shows velocity maps for a SAMI galaxy and its constituent bulge and disc. Our final SAMI galaxy sample comprises 1121 galaxies with $9 < \log(M_*/M_\odot) < 12$, with measurements for 468 bulges and 516 discs.

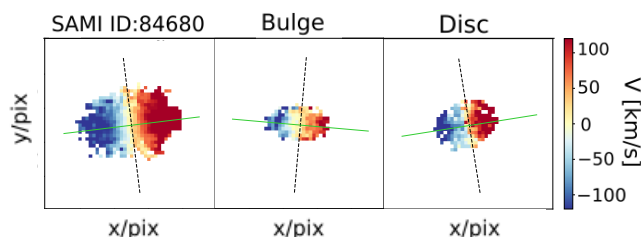


Figure 1: Stellar velocity maps for a SAMI galaxy and its constituent bulge and disc. The green line shows the kinematic PA and the black dashed line marks the projected axis of rotation.

Reconstruction of the cosmic web

We reconstruct the filaments of the cosmic web (shown in Figure 2) using the structure extractor DISPERSE [9] and the GAMA redshift survey [10] from which the SAMI Galaxy Survey has been selected.

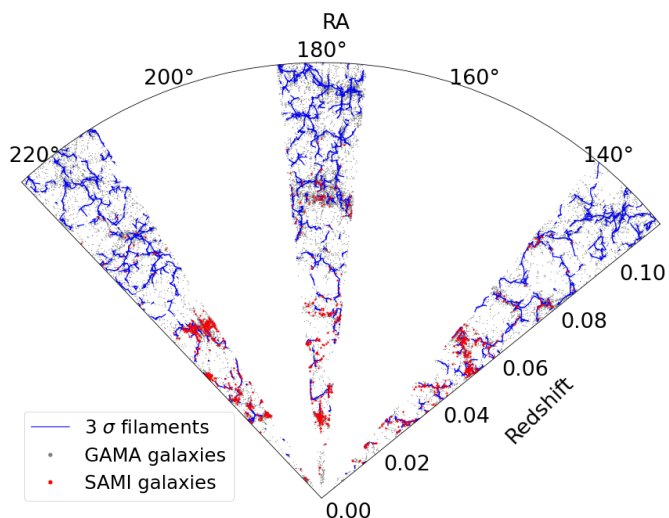


Figure 2: Projected network of cosmic filaments (blue lines) reconstructed from the GAMA galaxies (grey points). The red points represent the 1121 SAMI galaxies.

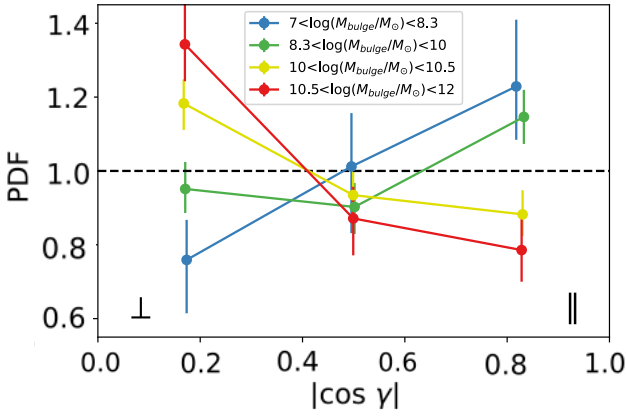


Figure 3: PDFs of the spin–filament alignments for 1121 SAMI galaxies in ranges of M_{bulge} . High- M_{bulge} galaxies tend to have spins aligned perpendicular to the closest filament, whereas low- M_{bulge} galaxies tend to have parallel alignments.

Spin–filament alignment correlates best with M_{bulge}

Our aim is to identify the galaxy properties that are most closely related to the flipping of the spin–filament alignments, to understand the physical processes involved. We focus on stellar mass, bulge-to-total flux ratio, and their geometric combination, the mass of the bulge: $M_{\text{bulge}} = M_{\star} \times B/T$. Each SAMI galaxy is assigned to the closest filament using the smallest 3D Euclidean distance. The spin–filament alignment is parametrised as $|\cos \gamma|$, the absolute value of the cosine of the angle between the galaxy spin axis and the closest filament: $|\cos \gamma|=1$ means that the galaxy spin axis is parallel to the filament while $|\cos \gamma|=0$ is perpendicular alignment.

Applying the Spearman test, we find significant correlations (coefficient; p -values < 0.05) of the galaxy spin–filament alignments with M_{\star} ($\rho = -0.07$; $p_S = 0.014$), B/T ($\rho = -0.11$; $p_S = 10^{-4}$) and M_{bulge} ($\rho = -0.13$; $p_S = 10^{-5}$). The partial least squares regression technique shows that M_{bulge} is the single parameter with the largest contribution ($\sim 70\%$) to the $|\cos \gamma|$ variance. Other galaxy properties, such as visual morphology, stellar age, star formation activity, kinematic parameters and local environment, show secondary correlations.

We divide the 1121 SAMI galaxies into M_{bulge} ranges and explore the probability distribution function (PDF) of $|\cos \gamma|$ in Figure 3. Galaxies with higher values of M_{bulge} have spins aligned preferentially perpendicular to the closest filament, whereas galaxies with lower values of M_{bulge} preferentially have parallel alignments. The PDFs are significantly different from a uniform distribution according to the Kolmogorov–Smirnov test (p -values < 0.05).

Thus M_{bulge} is the galaxy property that correlates best with spin–filament alignment. We conclude that bulge growth and spin–filament alignment flips from par-

allel to perpendicular are likely both caused by the same physical process, namely mergers.

Spin–filament alignments of bulges and discs

We investigate the separate spin–filament alignments of the bulge and disc components of galaxies in Figure 4. The alignment for bulges tends to be more perpendicular at all M_{bulge} values, suggesting they are merger products. Discs show a significant parallel tendency for low- M_{bulge} galaxies, but significant perpendicular alignment for high- M_{bulge} galaxies, implying multiple formation and evolution scenarios for discs.

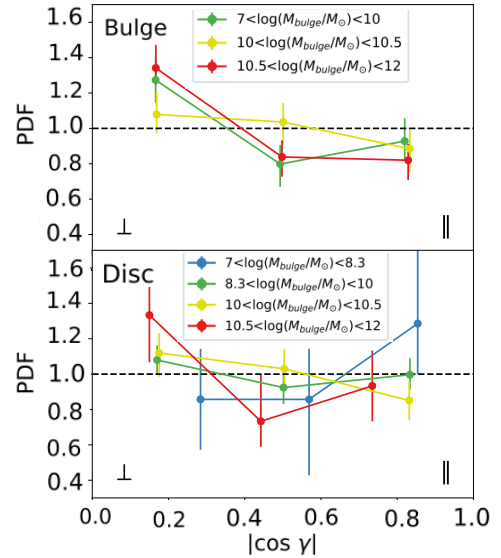


Figure 4: PDFs of spin–filament alignments for 468 bulges (top) and 516 discs (bottom) in ranges of M_{bulge} . Bulges show more perpendicular alignments, while discs tend to be aligned parallel for low M_{bulge} and perpendicular for high M_{bulge} .

Conclusions

Our findings highlight the importance of integral field spectroscopy surveys for elucidating how changes in the angular momentum of galaxies, bulges, and discs are related to their evolution within the cosmic web. The upcoming Hector galaxy survey will extend and deepen our understanding of spin–filament alignments.

References

- [1] Barsanti, S., et al. 2022, arXiv:2208.10767
- [2] Dubois, Y., et al. 2014, MNRAS, 444, 1453
- [3] Codis, S., et al. 2018, MNRAS, 481, 4753
- [4] Welker, C., et al. 2020, MNRAS, 491, 2864
- [5] Welker, C., et al. 2014, MNRAS, 445, L46
- [6] Croom, S., et al. 2021, MNRAS, 505, 991
- [7] Lee, J., & Erdogdu, P., 2021, ApJ, 671, 1248
- [8] Oh, S., et al. 2020, MNRAS, 495, 4638
- [9] Sousbie, T., 2011, MNRAS, 414, 350
- [10] Driver, S. P., et al. 2011, MNRAS, 413, 971

Short CV



- 2013: BSc in Physics, Univeristy of Pisa, Italy
- 2015: MSc in Astrophysics and Cosmology, University of Trieste, Italy
- 2017: MSc in Astronomy, Macquarie University, Australia
- 2021: PhD in Astronomy, Macquarie University, Australia
- 2021-present: ASTRO 3D Postdoctoral Fellow, Australian National University, Australia

An H I story of galaxies in A2626 and beyond

Tirna Deb

Department of Physics and Astronomy, University of the Western Cape, South Africa

In this diverse universe, galaxies are also observed in various shapes, sizes and colours. The cosmic environment of galaxies affects their properties, both during their formation and subsequent evolution involving interactions with their surroundings. In dense cosmic environments such as galaxy clusters, several physical mechanisms remove the atomic hydrogen gas (H I) discs of galaxies, resulting in quenching of the star formation activity in those galaxies. One of the most effective gas removal mechanisms acting on galaxies in clusters is ‘ram pressure stripping’[1] (RPS). This occurs when galaxies fall into the core of a cluster and encounter a head wind pushing the cold gas out of the galaxy, leaving the stars unaffected. Extreme examples of RPS are the ‘jellyfish’[2] galaxies that display ‘tentacles’ of gas that stretch far beyond their stellar discs and in which after new stars are born.

To investigate the morphological transformation and the quenching of star-formation of galaxies, we need to understand the physical processes of gas depletion and removal from galaxies. While the H I gas provides the raw fuel for star formation, the morphologies and kinematics of the extended, collisional and fragile H I gas discs of galaxies serve as sensitive diagnostic tracers of these environment driven gas depletion and removal processes[3, 4]. We have studied H I properties and morphologies of galaxies in and around A2626 cluster to investigate the environmental impact on the gas evolution and star formation activities of these galaxies.

Galaxies in and around A2626 cluster

Abell 2626 (A2626) is a moderately massive galaxy cluster ($M_{\text{halo}} \approx 5 \times 10^9 M_{\odot}$) at a redshift of $z=0.0545$, which, due to its location within the cosmic web, as well as its own identified substructures[5], is an ideal laboratory to study galaxy transformation processes. A2626 is part of the WINGS imaging and spectroscopic survey[6, 7] and harbours a number of so-called ‘jellyfish’ galaxies[8], indicating an ‘active’ cluster environment. A2626 is embedded in a wall of the cosmic web and is close to cluster A2637 as well as a diffuse, filament-like structure behind the wall. An extensive MMT/Hectospec redshift survey[5] over a $2^{\circ} \times 2^{\circ}$ area has revealed that three main environments exist in and around A2626: 1) the cluster A2626 with a virialized population of galaxies, 2) various substructures inside the cluster, indicating recently accreted galaxy groups, and 3) a diffuse filament just behind the cluster with a collection of loose groups dubbed ‘the Swarm’. Volume-limited H I imaging data from a single MeerKAT pointing centred on A2626[9] revealed 219 H I detected galaxies with optical counterparts covering different cosmic environments. We have presented the H I properties of the detected galaxies with tables and an atlas page for each galaxy, including an H I column-density map, a velocity field, a position-velocity diagram, and a global H I profile.

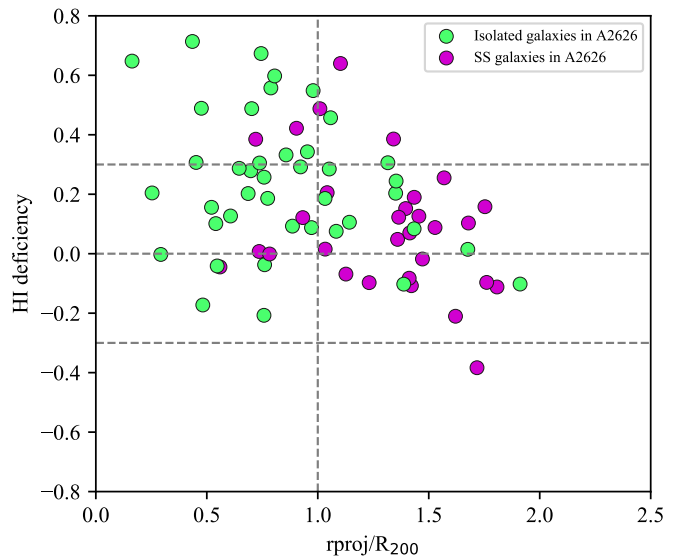


Figure 1: H I deficiency vs. projected distance normalised by R_{200} for the non-substructure or isolated (green circles) and substructure (magenta circles) galaxies in A2626. Horizontal dashed lines present the range of H I deficiencies of the field galaxies. There is a clear correlation between H I deficiency and projected distance - H I deficient galaxies reside close to the cluster core.

H I morphologies of galaxies in A2626 and beyond

We have explored the relationship between H I deficiency, H I morphology, and star formation deficiency for the galaxies in and around the A2626 galaxy cluster. There are three main environments: non-substructure galaxies in A2626 (cluster environment), substructure galaxies in A2626 (groups influenced by the cluster environment) and the Swarm galaxies (group environment). The galaxies detected in H I with sufficient signal-to-noise and angular resolution are considered for our analysis. To quantify asymmetries of the outer H I disc of a galaxy, we used 1) three visual classes based on the outermost reliable H I contour: settled, disturbed, unsettled H I discs, 2) the offset between the H I centre and the optical centre of a galaxy, and 3) the modified asymmetry parameter A_{mod} [10]. The H I deficiency of a galaxy is correlated with the projected distance from the centre of A2626 cluster. This trend probably indicates an increase of gas removal efficiencies in the cluster core, similar to what previous observations have found[11, 12]. Moreover, substructure galaxies tend to be more asymmetric than the non-substructure galaxies in A2626, plausibly because of more efficient tidal interactions within substructures than outside substructures. Furthermore, asymmetric, offset, and smaller H I discs are not necessarily the result of the cluster environment, as they are also observed in substructures in A2626 and in the Swarm. This hints that ‘pre-processing’ of the H I discs of galaxies in groups or substructures plays an important role, together with the ‘processing’ in the cluster environ-

ment. Finally, the galaxies in all three environments have slightly lower star-formation rates (SFRs) than the typical SFR for normal galaxies as manifested by their offset from the star formation main sequence, implying effective gas removal mechanisms when the galaxies are both in group and cluster environment.

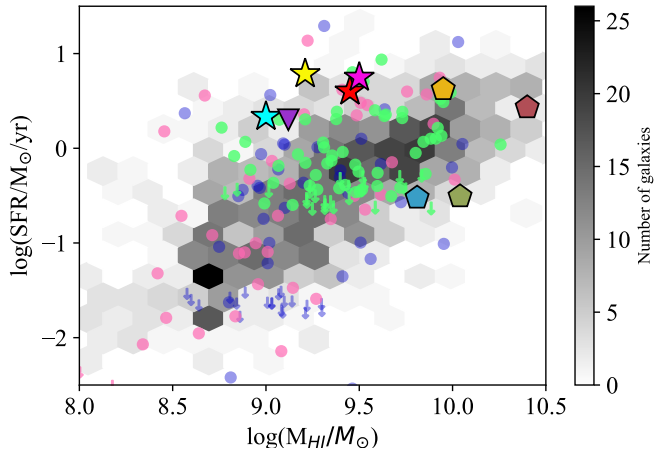


Figure 2: SFR vs H I mass for JFGs and JFCGs compared to the reference sample galaxies with the similar stellar mass range. Grey hexagons are galaxies from the xGASS sample (Catinella et al. 2010). Star and pentagon markers are JFGs and JFCGs respectively. JFGs are very H I deficient but their star formation is not quenched yet.

Jellyfish candidate galaxies in A2626

Within the MeerKAT surveyed volume in A2626, there are six plausible RPS or jellyfish candidate galaxies (JFCGs) from B-band optical images[13]. Two of the six galaxies JW100 and JW103 are confirmed as RPS galaxies from the H I observations. Both of these galaxies have low H I content, reside close to the cluster core, and move at very high velocities ($\sim 3\sigma_{cl}$). The other JFCGs, identified as non-jellyfish galaxies, are H I rich, their H I morphologies reveal warps, asymmetries, and possible tidal interactions. When we compared the H I content vs the SFR in both the RPS galaxies in A2626 and three other confirmed jellyfish galaxies from the GASP sample[14] with the reference sample galaxies, all five jellyfish galaxies stand out in the relation because of the lower H I masses for their SFRs. This signifies that in spite of having lost most of its gas reservoir, JFGs continue to form stars significantly.

Striking jellyfish galaxy JW100

JW100 is one of the most well-studied JFGs. We detect atomic (H I), molecular (CO), and ionised ($H\alpha$) gas tails of

similar extent (~ 50 kpc) in JW100. Comparing the multi-phase velocity channels, we do not detect any H I or CO emission in the northern part of the tail where $H\alpha$ and X-ray emission is present[15], possibly due to a prolonged interaction between the stripped gas and the inter-cluster medium. We also observe an anti-correlation between atomic and molecular gas, which signifies an efficient conversion of H I to H_2 in the southern part of the tail. We estimate that 80% of the H I gas has been removed and/or converted into H_2 by RPS. Of the remaining 20% of H I gas, we find 70% in the tail and 30% still in the disc. Thus JW100 is already at a very advanced stage of gas removal.

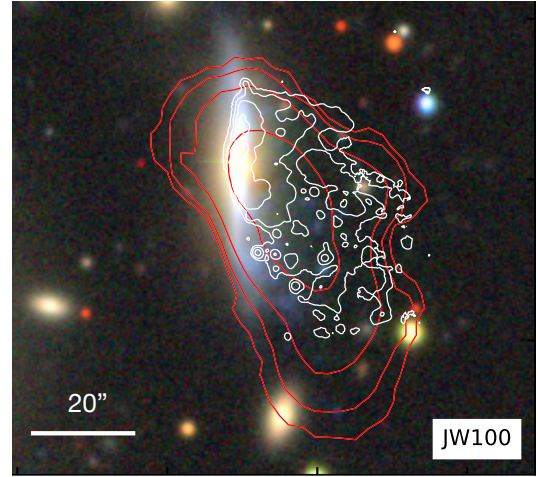


Figure 3: Multi-phase gas in the RPS tail of JW100. $H\alpha$ (white, 1" resolution) and H I (red, 20" resolution) contours are overlaid on the DECaLS color image.

References

- [1] Gunn, J.E., & Gott, J.R. III, 1972, ApJ, 176, 1
- [2] Poggianti, B.M., et al., 2017a, Nat, 548, 7667
- [3] Davies, R.D., & Lewis, B.M., 1973, MNRAS, 165, 231
- [4] Serra, P., et al., 2013, MNRAS, 428, 1
- [5] Healy, J., et al., 2021a, AJ, 162, 193
- [6] Omizzolo, A., et al., 2014, A&A, 561, 111
- [7] Moretti, A., et al., 2014, A&A, 564, 138
- [8] Poggianti, B.M., et al., 2016a, AJ, 151, 78P
- [9] Healy, J., Deb, T., et al., 2021b, A&A 654, A173
- [10] Lelli, F., et al., 2014, MNRAS, 445, 1694
- [11] Solanes, J.M., et al., 2001, ApJ, 548, 97
- [12] Chung, A., et al., 2009, AJ, 138, 1741
- [13] Poggianti, B.M., et al., 2016b, AJ, 151, 78
- [14] Poggianti, B.M., et al., 2017b, ApJ, 844, 48
- [15] Poggianti, B.M., et al., 2019, ApJ, 887, 155

Short CV



2016: Master in Physics, Presidency University, Kolkata, India
 2022: PhD in Astronomy, University of Groningen, The Netherlands
 2022–present: Postdoctoral Fellow, University of the Western Cape, South Africa

Why is colour special? Fundamental differences between red and blue quasars

Victoria A. Fawcett

Centre for Extragalactic Astronomy, Department of Physics, Durham University, DH1 3LE, UK

Quasi-stellar objects (QSOs), also known as quasars, are the most powerful class of Active Galactic Nuclei (AGN). Due to the unobscured view of the SMBH accretion disc (AD), which peaks in the ultra-violet (UV), the majority of Type 1 QSOs have very blue optical colours. However, there is a small but significant subset with redder optical-infrared colours (referred to as “red QSOs”).

Although red QSOs have been well studied in the literature (e.g., [1, 2]), there are still conflicting views on how red and blue QSOs are related. Some studies suggest they are intrinsically the same objects, with a red QSO simply representing a blue QSO observed at a higher inclination to the putative dusty torus, while other studies suggest an evolutionary scenario whereby a red QSO is a short-lived phase in QSO evolution. In order to distinguish between these two scenarios, in our work we have explored the radio and spectral properties of a sample of optically-selected red and blue QSOs [2, 3, 4, 5, 6, 7, 8].

To select our colour-selected samples we use the g^* (4770 Å) and i^* (7625 Å) band extinction-corrected photometry in the Sloan Digital Sky Survey (SDSS) DR14 catalogue [9]. We define our red and blue “control” QSOs (hereafter, rQSOs and cQSOs) as the top 90th percentile and middle 50th percentile of the observed SDSS $g^* - i^*$ distribution, respectively; therefore, the cQSOs represent typical QSOs in terms of their colour (see Figure 1 and [2, 3, 4] for more details).

In the following we summarise recent results from [3, 5, 8], exploring the radio and spectral properties of optically-selected rQSOs and how these compare to typical cQSOs.

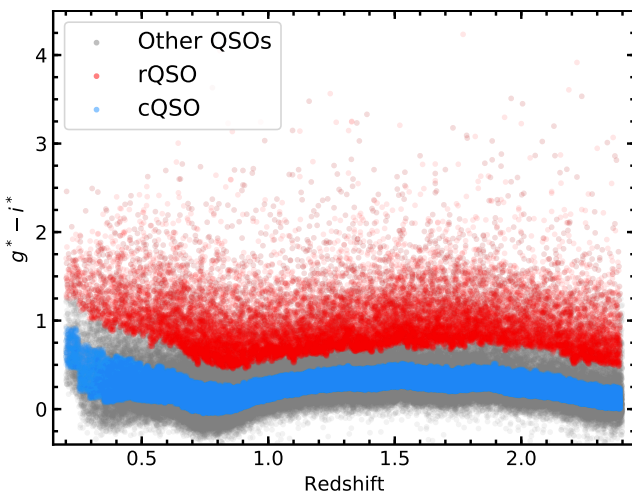


Figure 1: $g^* - i^*$ vs redshift for our sample of optically-selected rQSOs (red) and cQSOs (blue): the rQSOs and cQSOs represent the top 10% and median 50% of the $g^* - i^*$ distribution, respectively, as a function of redshift. See [2] for more details.

Enhanced radio emission in red QSOs

To explore the radio properties of our rQSOs, we matched the colour-selected samples to four different radio surveys: Faint Images of the Radio Sky (FIRST; 1.4 GHz), LOFAR Two-meter Sky Survey DR1 (LoTSS; 120–168 MHz), VLA Stripe 82 (S82; 1.4 GHz), and VLA COSMOS 3GHz (C3GHz; 3 GHz). See [5] and references therein for more details.

Exploring the radio-loudness parameter (\mathcal{R} ; defined here as the $L_{1.4\text{GHz}}$ to $L_{6\mu\text{m}}$ ratio; see [2] for more details), we calculated the enhancement in the radio-detection fraction of the rQSOs in the four different radio surveys (see our previous studies for more details [2, 3, 4]). Figure 2 displays the radio enhancement for the FIRST- (shaded orange), combined S82+C3GHz- (shaded blue), and LoTSS- (shaded magenta)-detected samples plotted as a function of \mathcal{R} . All three of these samples peak around $\mathcal{R} \sim -4.5$ with a factor ~ 3 – 6 excess in the radio enhancement for rQSOs, decreasing to around unity towards the extreme radio-loud and radio-quiet values.

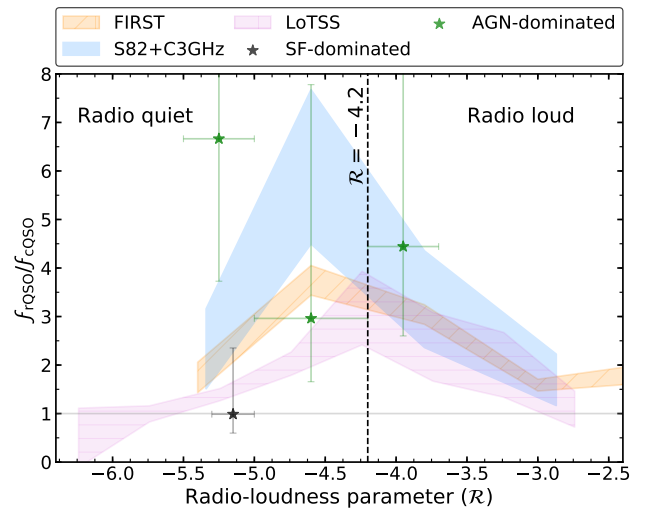


Figure 2: Radio-detection enhancement as a function of radio-loudness (\mathcal{R}) for the different radio-detected samples. The radio enhancement of the C3GHz rQSOs with radio emission dominated by SF is shown as a black star, and those with radio emission dominated by AGN processes are shown as green stars. See [3, 5] for more details.

Utilising the rest-frame (8–1000 μm) far-infrared (FIR) data available in the COSMOS field, we define the origin of the radio emission as dominated by star formation (SF) if the measured radio luminosity was within a factor of 3 of the radio-FIR relationship for star-forming galaxies, and AGN-dominated otherwise [3]. Using these definitions, we then split the lower radio-loudness bins covered by our C3GHz sample into sources with radio emission ei-

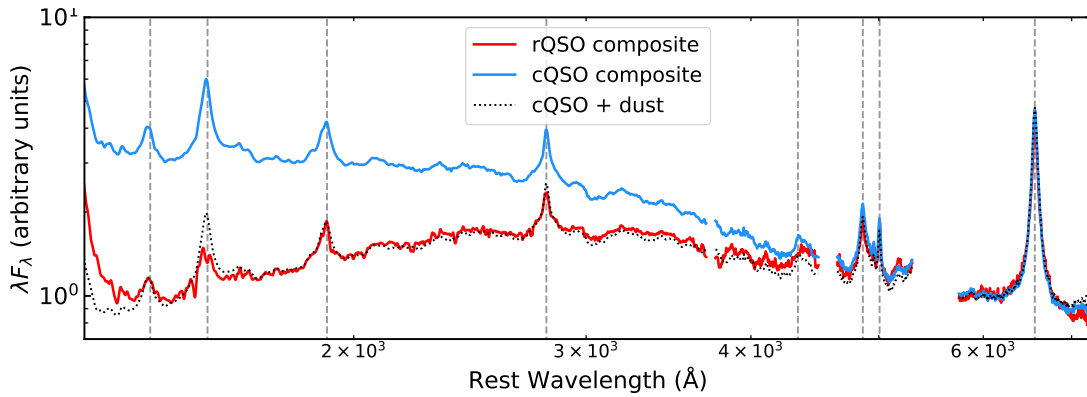


Figure 3: X-shooter rQSO and cQSO composites; the rQSO composite is consistent with a dust-reddened cQSO composite [8].

ther dominated by SF or AGN (black and green stars, respectively). From Figure 2, it is clear that, at $\mathcal{R} < -5$, SF-dominated sources have a radio enhancement consistent with unity (albeit low source statistics), expected if there are no differences in the SF properties of rQSOs and cQSOs [6]. Therefore, the radio enhancement in rQSOs is likely driven by AGN mechanisms. Analysing the radio morphologies, we also find that rQSOs have a preference for compact (< 2 kpc) radio counterparts compared to cQSOs [2, 3, 4, 7].

VLT/X-shooter properties of red QSOs

Analysing VLT/X-shooter optical–NIR spectra, we explored the extinction, emission and accretion properties of a sample of 40 rQSOs and cQSOs [8]. By fitting a dust-reddened cQSO composite to the rQSOs, we find that the red colours in $\sim 92\%$ of the rQSOs can be fully explained by dust extinction of an otherwise normal cQSO (see Figure 3). The amount of dust reddening in our rQSO sample is modest, with $E(B-V)$ values ranging from ~ 0.02 – 0.23 mags ($A_V \sim 0.06$ – 0.7 mags). We also find a strong correlation between $\Delta(g^* - i^*)$ and $E(B-V)$ which suggests our method of selecting dust-reddened QSOs is robust (see Figure 6 within [8]).

To explore the accretion properties of rQSOs, we fitted a thin AD model to the X-shooter spectra, fixing A_V to the best-fit values from our dust extinction analysis, in order to compute the mass accretion rate, black-hole spin and Eddington ratio parameters. For $\sim 83\%$ of the rQSOs and $\sim 86\%$ of the cQSOs, the thin AD model provided a good fit to the QSO continuum. Since both the majority of the rQSOs and cQSOs are well fitted with a thin AD model, this suggests that there are no significant differences between the accretion discs of cQSOs and rQSOs, once the effects of dust extinction are taken into account. We also refitted the thin AD models to the spectra, this time leaving A_V as a free parameter, and found consistent levels of dust extinction for the majority of the rQSOs. In addition to this, we find no significant differences in the

accretion properties of rQSOs and cQSOs.

Red QSOs as a transitional phase in galaxy evolution

The enhanced radio emission in red QSOs cannot be explained via a simple orientation model, suggesting more fundamental differences between red and blue QSOs. We also find that the main difference between red and typical QSOs is the presence of dust rather than significant differences in the accretion properties. On the basis of these results, a potential self-consistent scenario that links the enhanced radio emission to the dust in red QSOs is one in which the radio emission originates from shocks produced by either an outflow or a jet interacting with a higher opacity ISM/circumnuclear environment compared to typical QSOs (e.g., Figure 4).

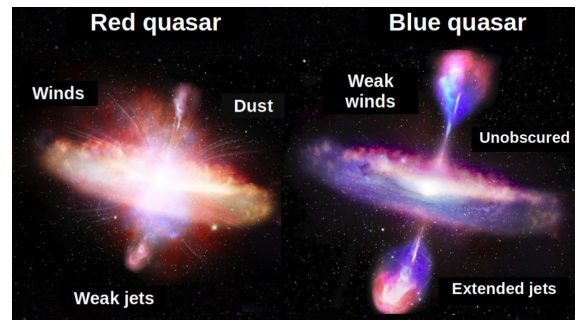


Figure 4: A schematic of potential evolutionary differences between red and blue QSOs; a red QSO has more dust, stronger winds, and weaker jets. Credit: L. Klindt & S. Munro.

References

- [1] Kim, D., & Im, M., 2018, *A&A*, 610, A31
- [2] Klindt, L., et al. 2019, *MNRAS*, 558, 3109
- [3] Fawcett, V. A., et al. 2020, *MNRAS*, 494, 4802
- [4] Rosario, D. J., et al. 2020, *MNRAS*, 494, 3061
- [5] Fawcett, V. A., et al. 2021, *Galaxies*, 9, 107
- [6] Calistro Rivera, G., et al. 2021, *A&A*, 649, A102
- [7] Rosario, D. J., et al. 2021, *MNRAS*, 505, 5283
- [8] Fawcett, V. A., et al. 2022, *MNRAS*, 513, 1254
- [9] Pâris, I., et al. 2018, *A&A*, 618, A51

Short CV



2017–2018: Master in Astronomy, University of Warwick, UK
 2018–2022: PhD in Astronomy, Durham University, UK
 2022–present: PDRA in Astronomy, Newcastle University, UK

Quasar Feedback Survey – the impact of jets and multi-phase outflows on their host galaxies

Aishwarya Girdhar

European Southern Observatory,

Garching bei München, Karl-Schwarzschild-Straße 2, 85748 Garching bei München

Active galactic nuclei (AGN) are the sites of growing supermassive black holes at the centre of galaxies [1]. Through accretion of matter, AGN can produce tremendous amounts of energy, that could also potentially exceed the binding energy of their host galaxies [2]. With this amount of energy available, if it can efficiently couple to the gas extending from the vicinity of the AGN to galactic scales, the AGN could cause significant impact (known as ‘feedback’) on their host galaxies by either facilitating or suppressing the star-formation (see review in [3]). This ‘AGN feedback’ has become an imperative ingredient in cosmological galaxy formation simulations for them to reproduce key observables of galaxy populations and intergalactic material [4]. However, understanding how this process occurs in the real Universe, particularly in the case of the most powerful AGN (i.e., quasars; $L_{\text{bol}} \geq 10^{45} \text{ erg s}^{-1}$), remains a challenge.

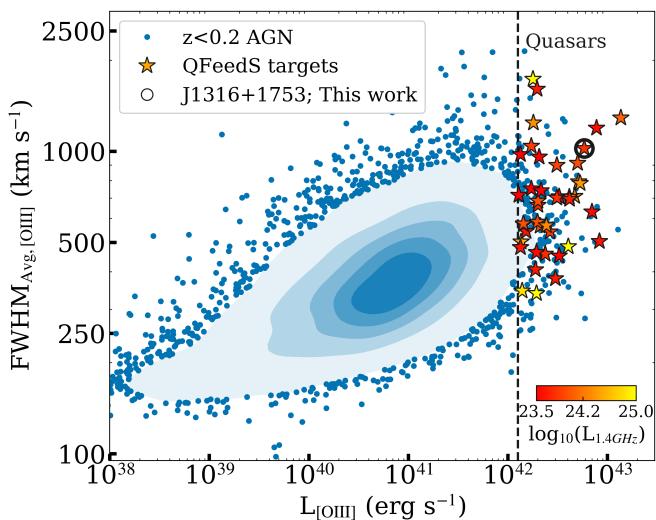


Figure 1: [O III] FWHM versus $L_{[\text{O III}]}$ for $z < 0.2$, spectroscopically-selected AGN from [6], represented as blue data points and density contours. Stars represent the 42 QFeedS targets, color-coded for their radio luminosity.

Quasar Feedback Survey

Quasar Feedback Survey (QFeedS; Figure 1; [5]) aims to address the challenges outlined above by studying the spatially-resolved multi-wavelength properties of 42 relatively low redshift ($z < 0.2$) quasar host galaxies. Using this redshift range allows us to obtain sensitive, high spatial resolution observations, whilst also yielding a reasonable sample of powerful quasars ($L_{\text{bol}} \geq 10^{45} \text{ erg s}^{-1}$) representative of L_* at the peak cosmic epoch of growth, where quasar feedback is expected to dominate ([1]). We study spatially-resolved radio observations using 6 GHz

VLA data, which provides important insights into the prevalence and properties of radio jets in what is a representative and predominantly ‘radio-quiet’ quasar sample [7, 5]. Radio-loud quasars have come to be known for their strong feedback effects, however high resolution radio data has now come to reveal how radio-quiet quasars could also be housing radio-jets capable of causing turbulence in the host galaxy, as we also show in this work.

Low-Power radio jets driving Multi-phase gas perpendicular to host-galaxy

We present MUSE and ALMA data of J1316+1753, a luminous $z=0.15$, type-2 quasar selected from the Quasar Feedback Survey. This target represents one of the most [O III] luminous sources from the survey ($L_{[\text{O III}]}=10^{42.8} \text{ erg s}^{-1}$) and exhibits a broad [O III] emission-line profile (FWHM $\sim 1300 \text{ km s}^{-1}$; Figure 1). Radio imaging of this source reveals low-power radio jets ($P_{\text{jet}} \sim 10^{44} \text{ erg s}^{-1}$) that are compact, reaching only 1 kpc in projected distance from the core. Furthermore, the jets are inclined into the plane of the host galaxy disk.

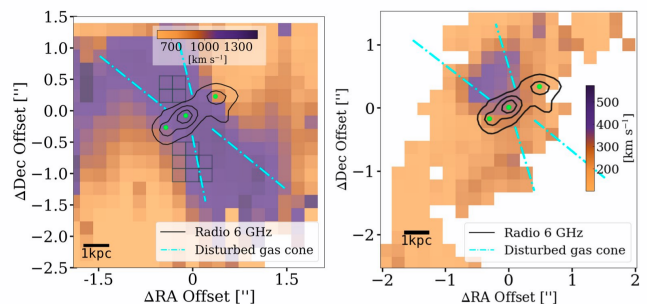


Figure 2: Kinematic analysis of the ionised (left) and molecular (right) gas in the central region around the jet, using maps of the non-parametric values of the [O III] and CO(3–2) emission-line fits. The black contours in each map represent the 6 GHz radio emission at levels of [32,16,4] RMS_{radio}. The three cyan dots represent the radio core (HR:A) and jet hot spots (HR:B and HR:C). A 1 kpc scale bar is shown in each of the maps. The emission corresponding to an enhanced velocity-dispersion ($W_{80} \geq 1000 \text{ km s}^{-1}$ in left panel and $\geq 400 \text{ km s}^{-1}$ in right panel), suggests a bi-conical structure in the region perpendicular to the jets (indicated by the dash-dotted cyan lines).

Our data enables us to map the stellar kinematics (traced with stellar absorption features), warm ionised gas properties (traced with optical emission-lines) and the cold molecular gas properties (traced with the CO(3–2) emission-line). On galaxy scales, both the molecular gas and ionised gas broadly follow the stellar gravitational motions [8]. However, across the central few kiloparsecs, both gas phases reveal high velocity non-

gravitational motions and we observe evidence of jet-induced feedback.

Ionised gas with very high velocity-dispersion (i.e., $W_{80} = 1000 - 1300 \text{ km s}^{-1}$) is seen to propagate outwards in a bi-cone from just behind the radio hot spots, travelling perpendicular to the galaxy disk and seen in projection as extending to at least 7.5 kpc from the nucleus (see Figure 2). The highest inferred electron densities of the ionised gas are found within these bi-cones (as inferred from the [S II] doublet). This turbulent gas is also seen in the molecular gas phase. However, it is 3 times less extended (and only in one direction) with 3 times lower velocity-dispersion (i.e., $W_{80} \sim 400 \text{ km s}^{-1}$) compared to ionised gas phase (see Figure 2).

velocity is observed just beyond the brighter radio hot spot, with tentative evidence for depleted CO (3–2) emitting gas at the same location.

Strong spatial connection between the jets and stellar properties

We see a close alignment of the position angle of the stellar bulge with the radio-jet axis. Furthermore, the regions with the highest stellar velocity-dispersion (i.e., σ_*) are seen to be lagging behind the jets, following the jet axis (see Figure 2 & 4 in [8]).

Implications for ‘radio-quiet’ AGN feedback

Our observations provide strong evidence for low power radio jets, inclined into the galaxy disk, having a direct impact on the multi-phase ISM inside the host galaxy of this type-2 quasar. Our observations are qualitatively consistent with the simultaneous positive and negative feedback effects observed in hydrodynamics simulations of jet-ISM interactions [9, 10, 11]. Specifically: (a) as the inclined, lower power jets move through the galaxy, it inflates a bubble of jet plasma which leads to a stronger interaction with the ISM; (b) as the jets propagate, they compress the gas in the disk also causing new stars to form in these regions, contributing to the formation of the stellar bulge and; (c) highly turbulent material is stripped and escapes above and below the galaxy disk, following the path of least resistance, resulting in removal of gas from the host galaxy.

Whilst jets have been seen to be dominant in lower power AGN, our observations reveal that jets can be the dominant feedback mechanism, even for this bolometrically luminous source, i.e., for an AGN currently in a ‘quasar mode’. To understand the relative role and impact of jets and winds in quasars we are currently performing a similar multi-wavelength study of the wider population.

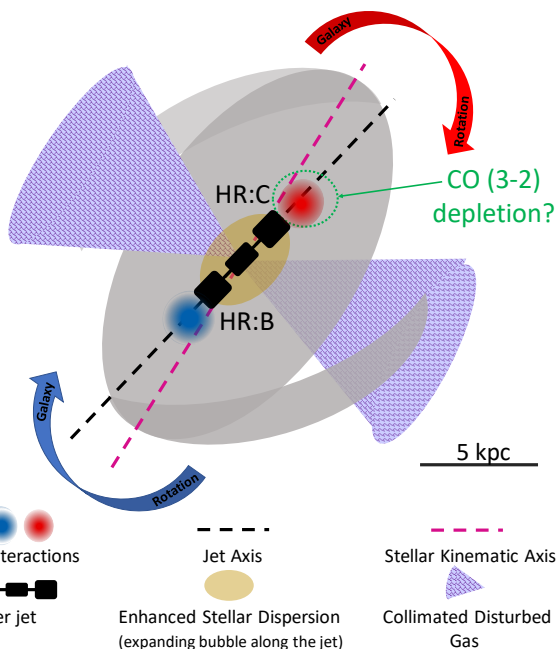


Figure 3: A schematic view of the galaxy J1316+1753 to highlight the key observations identified in this work. The line-of-sight view (where North is up and East is to the left); A legend shows the different symbols used to represent the main features of interest.

In Figure 3, we present a schematic of the galaxy from line of sight illustrating the observed features. We observe two bright and high velocity offset ionised gas components (separated by 441 km s^{-1}) concentrated at the positions of the jet hot spots and that appear to propagate away from the jets, along the jet axis (see Figure 3). Furthermore, a -100 km s^{-1} change in the molecular gas

References

- [1] Kormendy, J., Ho, L. C., 2013, ARA&A, 51, 511.
- [2] Cattaneo, A., et al., 2009, Natur, 460, 213.
- [3] Harrison, C. M., 2017, NatAs, 1, 0165.
- [4] Vogelsberger, M., et al., 2014, MNRAS, 444, 1518.
- [5] Jarvis, M. E., Harrison, C. M., Mainieri V., et al., 2021, MNRAS, 503, 1780.
- [6] Mullaney, J. R., et al., 2013, MNRAS, 433, 622.
- [7] Jarvis, M. E., Harrison C. M., et al., 2019, MNRAS, 485, 2710.
- [8] Girdhar, A., Harrison, C. M., Mainieri V., et al., 2022, MNRAS, 512, 1608.
- [9] Mukherjee, D., et al., 2018, MNRAS, 479, 5544.
- [10] Mandal, A., et al., 2021, MNRAS, 508, 4738.
- [11] Meenakshi, M., et al., 2022, arXiv, arXiv:2203.10251

Short CV



2012–2015: Bachelor of Science (Hons.) in Physics, University of Delhi, India
 2017: Research Visit, Scuola Normale Superiore, Pisa, Italy
 2017–2019: Master in Astronomy & Astrophysics, University of Innsbruck, Austria; University of Padova, Italy; University of Belgrade, Serbia
 2019–present: PhD in Astronomy, European Southern Observatory, Germany

The Impact of the CMB on high- z AGNs jets

Luca Ighina

INAF, Osservatorio Astronomico di Brera, Via Brera 28, 20121, Milano, Italy
DiSAT, Università degli Studi dell'Insubria, Via Valleggio 11, 22100, Como, Italy

Radio-Loud (RL) Active Galactic Nuclei (AGNs) are among the brightest astrophysical sources at all wavelengths. Their relativistic jets can affect both their Supermassive Black Holes (SMBHs) growth and the surrounding intergalactic medium. While in the radio band these jets can be observed at all scales (from pc to Mpc scales), their X-ray and γ -ray emission is expected to be concentrated on very small scales (<10 pc). However, after the launch of the Chandra X-ray telescope, several kpc-scale jets were detected [1] and the mechanism responsible for their high-energy radiation at these scales is still under debate. Understanding its origin is crucial also to derive the physical properties of these jets (e.g. the power) at large scales and, as a consequence, their impact on the environment. In the following, we explore the Inverse Compton interaction of the relativistic electrons within relativistic jets with the Cosmic Microwave background photons (IC/CMB) as possible interpretation. Moreover, we also estimate how this interpretation could also affect the observed evolution across cosmic times of the SMBHs hosted in jetted systems.

The most distant large-scale relativistic jet, at $z = 6.1$

After the detection of several large-scale jets with the Chandra telescope, one of the most popular interpretations proposed for their X-ray emission was that it is produced by the IC/CMB interaction [2]. Despite requiring quite extreme assumptions on the physical parameters (e.g. bulk Lorentz factor of the kpc-scale jets $\Gamma \sim 10$ -20), this model was successful in reproducing the high X-ray fluxes observed in the majority of these large-scale jets. However, after the launch of the Fermi γ -ray telescope, this model was challenged by the non-detection of the expected strong γ -ray emission in a few objects in the low- z Universe ($z < 1$). Therefore, another interpretation was proposed, with the X-ray radiation produced by a second population of highly-energetic electrons (with Lorentz factors $\gamma \sim 10^{8-9}$) through synchrotron (see [3]). Nevertheless, we still expect the IC/CMB process to take place, especially at high redshift. Indeed, given the strong redshift dependence of the CMB energy density, $U_{\text{CMB}} \propto (1+z)^4$, and that the IC/CMB is significantly boosted for jets oriented close to our line of sight (i.e. for sources classified as blazars), the best way to constrain it is to focus on high- z blazars. To this end we performed a Chandra X-ray observation of the most distant blazar currently known, PSO J0309+27 at $z = 6.1$ [4]. This observation revealed the presence of a ~ 20 kpc jet extending in the North-East direction (see Figure 1), making it the highest-redshift large-scale jet currently known. From the detailed study of its multiwavelength emission (see [5]), we found that its X-ray flux is fully consistent with the IC/CMB process with $\Gamma \sim 2$, therefore without requiring the extreme bulk velocities needed at low redshift. This is due to a double effect of the CMB energy

density increase at high redshift: (a) it boosts the IC/CMB process by a factor $(1+z)^4$; (b) it decreases the cooling timescale of the electrons, which, in turn, cannot be accelerated up to the very high energies needed to emit in the X-rays through synchrotron. Therefore, from our work we concluded that, while in the local Universe the synchrotron process likely dominates the X-ray emission observed in large-scale relativistic jets, at high redshift ($z \gtrsim 2$) the IC/CMB process becomes the most important mechanism.

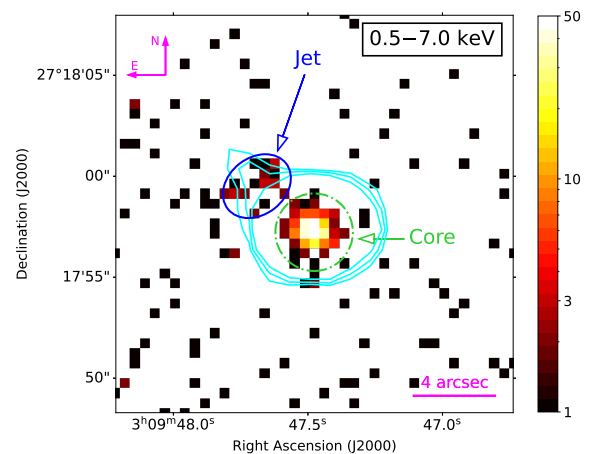


Figure 1: Chandra X-ray image of PSO J0309+27 with the $(3, 3\sqrt{2}, 6) \times \text{RMS}$ radio contours at 3 GHz from the VLASS survey overlaid. The kpc-scale jet is highlighted by the blue ellipse. Adapted from [5].

Space density evolution of blazars

If, as explained above, the IC/CMB process was important and significant at high redshift, we would expect the overall X-ray emission (core plus extended jet emission) of blazars to increase as a function of redshift. Interestingly, such a trend was found from the comparison of statistically complete samples of blazars at high and low redshift (e.g. [6]). In particular, these studies found that $z \sim 4.5$ blazars have, on average, X-ray-to-radio luminosity (X/R) ratios about two times larger than their low- z counterparts. This difference could also have important consequences on our understanding of the evolution of blazars, and therefore of the jetted SMBHs, through cosmic times. Indeed, recent studies have found that the cosmological evolution of the blazar population significantly differs when observed in the X-ray or the radio band. In particular, X-ray studies (e.g. [7]) find that the number of blazars at high redshift is significantly larger than the one expected from the radio band (e.g. [8]). As shown also in Figure 2, the X-ray space density evolution of blazars, computed starting from the radio Luminosity Function (LF) derived by [8] and assuming a constant X/R conversion factor, under-predicts the number of blazars compared to the observed X-ray data (green points). However, if we now consider that a fraction of

the overall X-ray emission is due to the IC/CMB process, we expect the typical X/R ratios of blazars to evolve with redshift as follows:

$$L_X/L_r(z) = L_X/L_r(z=0) \times (1 - A_0) + A_0 \times (1+z)^4,$$

where A_0 is the relative contribution of the IC/CMB emission at $z = 0$. Based on the study of the largest complete samples of blazars selected in the radio band, we found A_0 to be of the order of $\sim 10^{-3}$, that is, the IC/CMB contribution at low redshift is negligible, as expected. By including this type of X/R evolution in the computation of the expected X-ray space density starting from the radio LF, we found that the increase of the X-ray emission related to the IC/CMB process can reconcile the evolutions observed in the radio and X-ray band, see the solid red curve in Figure 2.

In order to improve the current statistics at high redshift and therefore to further test the IC/CMB mechanism, the e-ROSITA X-ray mission will be crucial, thanks to its relatively deep sensitivity over the entire sky. Indeed, the actual number and redshift distribution of the blazars detected by this mission will depend on the importance of the IC/CMB process to the observed X-ray emission. At the same time, detailed studies on these X-ray-selected sources with the Chandra telescope, like the one presented above, will further constrain the IC/CMB model.

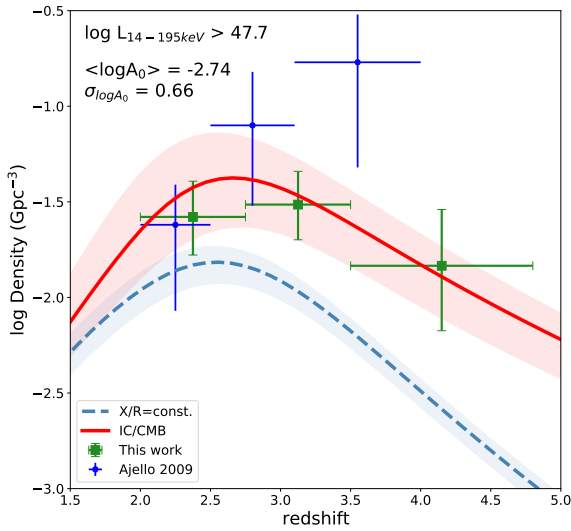


Figure 2: Observed X-ray space density of blazars: green squares from [9], blue points from [7] as reference. The two lines are the expected space density evolution of blazars with (solid red) and without (dashed blue) the redshift evolution given by the IC/CMB process. Adapted from [9].

Hunting down RL AGNs at high redshift

If, on the one side, the e-ROSITA mission will uncover

the X-ray-brightest end of the blazar population, on the other side, on-going and future radio surveys, like the ones performed by the Square Kilometre Array Observatory and its precursors, will uncover the much larger RL population of AGNs at high redshift. Indeed, soon after the first data release of the Rapid ASKAP Continuum Survey (RACS) we were able to identify one of the most distant RL AGNs currently known: VIK J2318–3113, at $z = 6.44$ [10]. Given this first successful identification, we are now using the RACS survey as starting point for the discovery of new RL AGNs at high redshift. In particular, from its combination with optical/NIR wide-area surveys currently available (namely Pan-STARRS and DES) and the use of the *dropout* technique we are building the first statistically complete sample of RL AGNs at $5 < z < 6.5$. In Figure 3 left panel we report the sky coverage of the RACS and the optical/NIR surveys used together with the sky distribution of the currently known $z > 5$ RL AGNs and our newly selected candidates. While the spectroscopic confirmation of the majority of the candidates is still ongoing, we were already able to identify two new $z > 6$ RL AGNs through dedicated Gemini–South/GMOS observations (GS-2021-DD-112, P.I. Ighina; see Figure 3 right panel). Chandra observations of these sources will potentially allow us to detect and study more kpc-scale jets at $z > 6$ to further test the IC/CMB model.

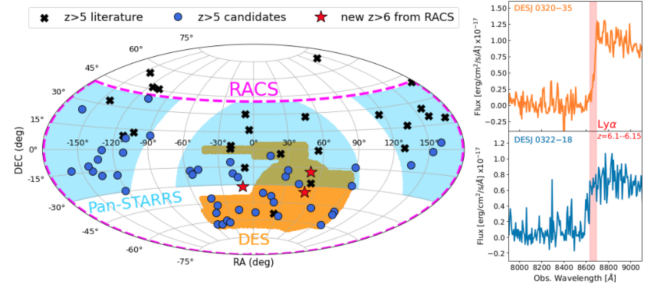


Figure 3: Left panel: Sky coverage of the radio and optical/NIR surveys used for our selection together with the currently known, the new selected candidates and the newly identified RL AGNs at $z > 5$. Right panel: zoom on the optical/NIR dropout of the two newly confirmed RL AGNs at $z > 6$.

References

- [1] Schwartz, D. A., et al., 2000, ApJ, 540, 69
- [2] Tavecchio, F., et al., 2000, ApJ, 544, L23
- [3] Georganopoulos, M., et al., 2016, Galaxies, 4, 65
- [4] Belladitta, S., et al. 2020, A&A, 635, L7
- [5] Ighina, L., et al. 2022, A&A, 659, A93
- [6] Ighina, L., et al. 2019, MNRAS, 489, 2732
- [7] Ajello, M., et al., 2009, ApJ, 699, 603
- [8] Mao, P., et al., 2017, ApJ, 842, 87
- [9] Ighina, L., et al. 2021, MNRAS, 505, 4120
- [10] Ighina, L., et al. 2021, A&A, 647, L11

Short CV



2018–2020: MSc in Astrophysics, Milano–Bicocca University, Milano, Italy
 2020–present: PhD in Physics and Astrophysics, Insubria University, Como, Italy
 2024–on: Relaxing on a beach somewhere in the Caribbeans

The Galaxy Luminosity Function via Clustering Based Redshift Inference: can we find the bottom of the galaxy population?

Geray S. Karademir

Swinburne University of Technology, John St, Hawthorn, VIC 3122, Australia

Even at low redshifts, observing faint galaxies is a challenge as both deep and wide surveys are needed [1]. In addition to being hard to observe these galaxies are hard to simulate at the same time, as they require very low resolution limits. As faint galaxies are particularly sensitive to dark and baryonic matter coupling and feedback, the faint end of the galaxy luminosity function (GLF) has been in the focus of multiple controversies, including the missing satellite problem or the core-cusp problem .

In this study we use clustering based redshift inference (cluster- z s) to map the $z \sim 0$ GLF down to the faintest possible luminosities, beyond the reach of spectroscopic and photometric redshift surveys.

Clustering based redshift inference

Clustering based redshift inference is a method to derive the redshift distribution of a target dataset statistically. This process exploits the fact that galaxies are clustered (rather than randomly distributed) to derive redshift information for our target sample, using only their observed positions on the sky. The basic idea behind the calculation of cluster- z s is that the spatial distribution of galaxies on the sky is unique at each redshift. This leads to the principle that if two populations of objects overlap on the sky, but are at different redshifts their angular correlation is expected to be zero (ignoring gravitational lensing effects) [see 2]. By calculating the cross-correlation amplitude between the target and the reference dataset in a number of redshift bins it is possible to derive the redshift distribution of the target sample. We follow a similar cluster- z formalism as laid out by [3].

For the calculation there are three samples needed. One dataset consisting of objects with unknown redshifts but known spatial positions for which the cluster- z s are

going to be calculated for. In order to trace the large scale structure a reference set with objects of accurate measurements of their full 3D positions is needed in addition. As the calculated clustering amplitude have to show if objects at a specific redshift are clustered stronger or less, than a uniform population would do, we need an unclustered random dataset to compare to. All of these datasets obviously have to cover the same area on the sky.

The overall process of deriving cluster- z s is explained in greater detail in [4] and is illustrated here for three redshift slices for the ~ 60 square degrees GAMA region G12 in Figure 1. In the left panel the target data-points overlay the reference data-points of three different redshift slices. Secondly the corresponding cross- (w_{tr} , between the target and reference set) and auto-correlation (w_{rr} , between the reference and random set) functions are calculated based on the datasets in the first panel. The cluster- z amplitude is calculated as the integral of w_{tr} and w_{rr} within the clustering ranges shown in the middle panel. If this value is calculated for all redshift slices, the final cluster- z distribution can be constructed.

The faint end of the GLF

Since cluster- z s only consider angular position, we are limited by the depth of the photometric catalogue at $m_r < 22.5$, which is ~ 3 magnitudes beyond the GAMA spectroscopic redshift limit. For this experiment we use positions and total r -band magnitude from the GAMA produced photometric catalogues [5], which are derived from KiDS r -band imaging [6] for the three equatorial GAMA fields. We bin our target sample by observed magnitude, and perform the cluster- z calculation (illustrated in Figure 1) to determine the conditional redshift

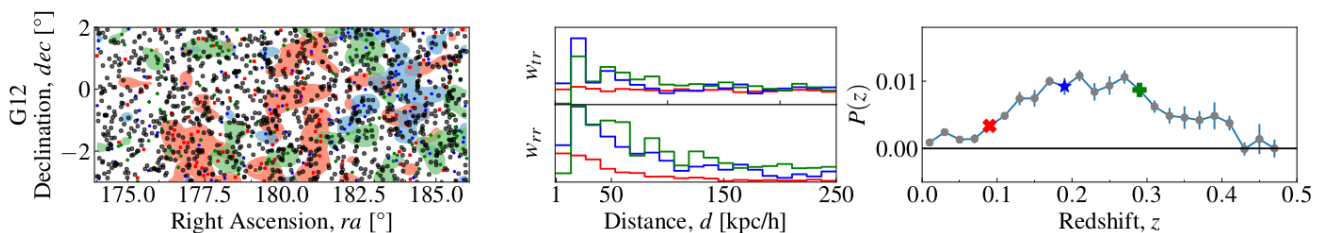


Figure 1: Illustration of the clustering redshifts process in one of the equatorial GAMA fields (G12). In the left panel the contours of three different redshift slices at $z = 0.09$ (red), 0.19 (blue), 0.29 (green) with $\Delta z = 0.02$ is shown, on top of a sub-sample of the target data (black). The differences of the cosmic web at these redshifts are used to calculate the cross-correlation of the target dataset and the reference data at these redshifts. By using the integrated results of the resulting cross-correlation function w_{tr} and the auto-correlation function w_{rr} over the corresponding clustering ranges r_c (shown in the middle), the $P_{m,z}$ at these redshifts are calculated. In the last panel the resulting $P_{m,z}$ is shown and the points derived at the three redshift slices are marked accordingly. (reproduced from [4])

distribution $P(z|m)$ for each magnitude bin. For the calculation we are restricted to $z \lesssim 0.5$, as the maximal extent of our GAMA spec- z reference sample. The main technical challenge in our experiment arises from the fact that output of the process of clustering redshift inference is proportional to the redshift distribution for the target sample, up to some unknown scalar. Our strategy is to use a simple parametric model for the evolving GLF to constrain the values for the normalisation factors as it is described in [4].

Our main result of mapping the field GLF at $z \sim 0$ across 14 magnitudes or 5.5 decades in luminosity is shown in Figure 2. The measured slope of the GLF remains remarkably flat over the range $-20 \lesssim M_r \lesssim 13$, with a sharp upturn below $M_r \sim -12.5$ or $\log L/L_\odot \sim 6.5$. A similar upturn has been found for the Coma Cluster by Yamanoi [7]. Following Yamanoi [7], we use a simple model to predict the luminosity function for the Globular Cluster (GC) population, based on our GLF fits. As it is shown in Figure 2 this simple prediction with no free parameters provides a good explanation to our measurements.

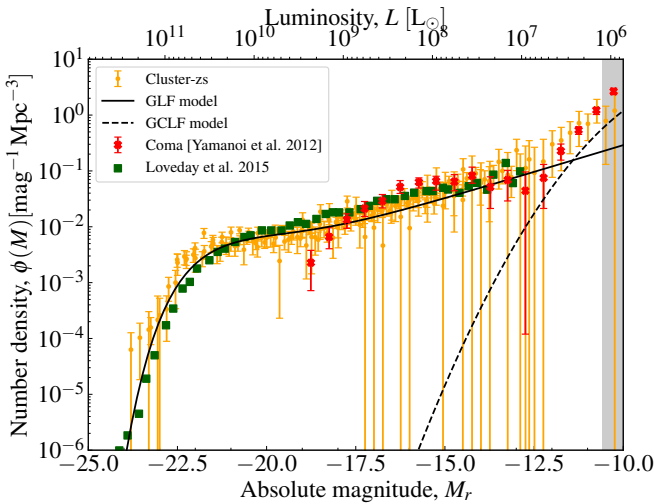


Figure 2: Comparison of the resulting GLF measurements (orange) with the literature and the GLF and GCLF models (black). The values $M_r > -10.7$ (grey area) are below our magnitude limits and potentially incomplete. At magnitudes $M_r \gtrsim -11.5$ the GCLF is resulting in larger values than the GLF model. This upturn occurs at the same range where the GCLF is overtaking the GLF, which indicates that at $M_r \gtrsim -11.5$ sub-galactic objects become more numerous than galaxies (reproduced from [4]).

The dominant source of systematic error/uncertainty in our results is the unknown evolution of the mean bias of the target samples over the $0 < z \lesssim 0.5$ interval. Being mindful of these issues, we have focused particularly on the $z \sim 0$ GLF, where the impact of these uncertainties is minimised.

Figure 2 shows that we have mapped the $z \sim 0$ GLF from the most luminous galaxies all the way down to where sub-galactic objects take over as the most numerous extragalactic population.

In doing so we demonstrated the potential for clustering based redshift inference in deriving the GLF. This technique offers manifold applications as it is not limited to the optical only and can be extended: e.g. by using deeper reference sets, or by combining different reference sets even deeper studies would be possible.

References

- [1] Loveday, J., et al., 2015, MNRAS, 451, 1540
- [2] Rahman, M., et al., 2015, MNRAS, 447, 3500
- [3] Menard, B., et al., 2013, preprint(arXiv:1303.4722)
- [4] Karademir, G. S., et al., 2021, MNRAS, 509, 5967
- [5] Bellstedt, S., et al. 2020, MNRAS, 496, 3235
- [6] Kuijken, K., et al., 2019, A&A, 625,A2
- [7] Yamanoi, H., et al., 2012, AJ, 144, 40

Short CV



2016: BSc in Physics, Ludwig-Maximilians-University, Munich, Germany
 2018: MSc in Astrophysics, Ludwig-Maximilians-University, Germany
 2019-present: PhD in Astrophysics, Swinburne University of Technology, Melbourne, Australia

Non-linear (Black Hole Mass)—Spheroid Scaling Laws & The Role of Galaxy Morphology

Nandini Sahu

OzGrav-Swinburne, Centre for Astrophysics and Supercomputing, Swinburne University of Technology, Hawthorn, VIC 3122, Australia

The correlations observed between directly (dynamically) measured super massive black hole (SMBH) mass and host galaxy properties holds crucial insights for understanding their (expected) co-evolution and have many direct applications. The most studied correlation is between black hole mass (M_{BH}) and the mass of the spheroid ($M_{*,\text{sph}}$) of the host galaxy, which was thought to be linear (on a log-log scale) based upon a sample massive early-type galaxies (ETGs) and excluding late-type galaxies (LTGs) with alleged “pseudo-bulges”. However, with increasing sample size, subsequent studies have revealed important advancements about the nature of the $M_{\text{BH}}-M_{*,\text{sph}}$ relation. A comprehensive review on scaling relations of M_{BH} with various host galaxy properties (e.g., $M_{*,\text{sph}}$, velocity dispersion σ , and central light concentration inferred by Sérsic index n) known until 2016 can be found in [7].

Here we present subsequent crucial advancements in the understanding of BH–Spheroid (*a.k.a.* bulge) correlations based upon a total sample of 127 dynamically measured BH masses and bulge properties measured with unprecedented accuracy, which almost doubles the sample used in [16].

Galaxy Sample and Measurement of Bulge

In order to extract accurate bulge properties (e.g., mass or size), we generated 2D isophotal models of host galaxy images. We performed careful multi-component decomposition of galaxy light profile using in-house software ISOFIT and CMODEL inbuilt in IRAF and PROFILER, respectively, which are publically available [3, 4]. Here, ISOFIT performs a uniform sampling of the quasi-elliptical isophotes of the galaxy image using “eccentric anomaly” (rather than the angular parameter of a circle as used in ELLIPSE). Additionally, it uses higher-order Fourier coefficients which precisely capture the isophotal irregularities in a multi-component galaxy and further provide an excellent galaxy model via CMODEL task. Further, we identified various components present in a galaxy and disassembled total galaxy light into its components (including bulge) with the help of special functions inbuilt in PROFILER. For example, we use a Sérsic or core-Sérsic function to describe the light profile of normal bulges and core-depleted bulges, respectively, which provided us with a measure of luminosity associated with the bulge (converted to stellar mass using an appropriate stellar mass-to-light ratio), and it is the size (e.g., effective half-light radius $R_{e,\text{sph}}$).

The image analysis for 127 galaxies was collectively done in [15], [5], and [11]. The dynamical BH mass measurements were taken from other studies, which used stellar and gas dynamical modelling, megamaser kine-

matics, proper motion (for Sgr A), and the latest direct imaging (for M87) techniques. For a detailed description of the imaging, analysis techniques, multi-component decomposition profiles, bulge/galaxy properties, galaxy morphology, and original sources of BH mass, readers are directed to the above three studies. After excluding mergers (NGC 1316, NGC 5128), stripped galaxies (NGC 4342, NGC 4486B), bulge-less galaxies (NGC 2748, NGC 4395, NGC 6926), more than 2σ outliers (NGC 1277, NGC 1300, NGC 2787), and the only galaxy with intermediate BH mass (NGC 404), our sample comprises of 76 ETGs and 39 LTGs. ETGs include elliptical (E: pure spheroidal), ellicular (ES: galaxies with an intermediate-scale disk within their spheroids) [8], and lenticular galaxies (S0: galaxies with a large-scale disk extending out of their bulges) and LTGs include all kinds of spiral galaxies (S).

Black Hole Mass–Spheroid Correlations

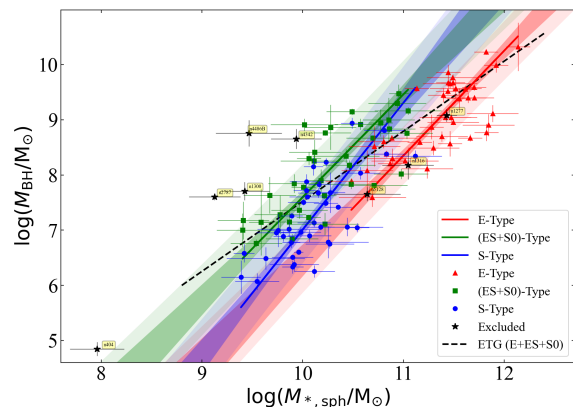


Figure 1: The quadratic $M_{\text{BH}}-M_{*,\text{sph}}$ relations defined by Elliptical (E), Ellicular & Lenticular (ES+S0), and Spiral galaxies (S). The black dash line shows the near-linear relation initially seen for all ETGs (E+ES+S0).

In order to establish the $M_{\text{BH}}-M_{*,\text{sph}}$ relation we used the symmetric application of BCES regression [1] which offers equal treatment and considers substantial uncertainties in both the parameters. Initially, we found that LTGs define a quadratic relation (blue line in Fig 1) that is steeper than the near-linear relation defined by (all) ETGs (dashed black line in Fig 1). However, further investigation showed that ETGs with a disk (ES and S0) and ETGs without a disk (E) define two different almost quadratic relations which are offset from each other by more than an order of magnitude in M_{BH} -direction. Thus, ETGs with a disk, ETGs without a disk, and LTGs define three different almost quadratic relations (with power-law

slopes ~ 2) in the $M_{\text{BH}}-M_{*,\text{sph}}$ diagram. Figure 1 is adapted from [11], see their Table 5 for the parameters of $M_{\text{BH}}-M_{*,\text{sph}}$ relations.

The steeper than linear relation between BH mass and bulge mass has been suspected by previous simulation and semi-analytic studies as well [2, 6]; however, the offset between ETGs with a disk and purely spheroidal elliptical galaxies has been realized in [11] for the first time. Subsequently, the same substructures were observed in the BH mass and spheroid effective half-light radius diagram due to ETGs with a disk, ETGs without a disk, and LTGs. The relation between M_{BH} and spheroid half-light radius, $R_{e,\text{sph,eq}}$, along spheroid's geometric-mean axis are shown in Figure 2 (adapted from [13]). The three $M_{\text{BH}}-R_{e,\text{sph,eq}}$ relations are almost quadratic power-laws, and their full expressions can be found in [13, their Table 2].

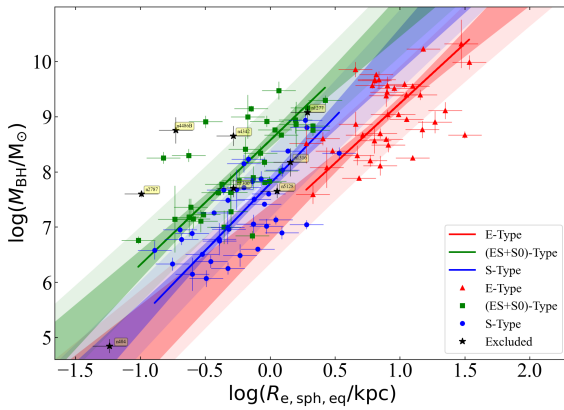


Figure 2: The quadratic $M_{\text{BH}}-R_{e,\text{sph,eq}}$ relations defined by Elliptical (E), Ellicular & Lenticular (ES+S0), and Spiral galaxies (S).

This offset appears to be due to smaller/less massive bulges of ETGs with a disk relative to the spheroids of elliptical galaxies, hosting similar BH mass and has been subsequently observed in the $M_{\text{BH}}-M_{*,\text{sph}}$ diagram via a simulation studying high-redshift evolution of black holes and their host galaxies [10]. Interestingly, the same substructures are observed in the $M_{\text{BH}}-(\mu_e$ or Σ_e : projected bulge density at $R_{e,\text{sph}}$) and the $M_{\text{BH}}-(\rho_e$: internal bulge density at $R_{e,\text{sph}}$) diagrams [14].

On investigating the $M_{\text{BH}}-(\text{total galaxy stellar mass: } M_{*,\text{gal}})$, we found that the offset between ETGs with and without disk reduces, suggesting a single $M_{\text{BH}}-M_{*,\text{gal}}$ relation for all ETGs; whereas, the LTGs define a relation with a slope twice as that of ETGs (see [11]). The $M_{\text{BH}}-M_{*,\text{gal}}$ diagram has a slightly higher scatter in M_{BH} -direction than the $M_{\text{BH}}-M_{*,\text{sph}}$ relations, but provides an easier way to predict BH mass in other galaxies,

without going through the multi-component decomposition of galaxy light.

Conclusion and Future Scope

The revelation of consistent morphology-dependent substructures significantly improve the previous linear relation and advance our understanding of BH mass–bulge connection, which is now known to depend on host galaxy morphology shaped by evolutionary processes (accretion) quenching, mergers) the galaxy goes through. This discovery was possible with accurate bulge properties and detailed galaxy morphology achieved via state-of-the-art modelling and multi-component decomposition of a galaxy image. In addition to the above-discussed BH scaling relations, the we also found morphology-dependent divisions in the $M_{\text{BH}}-\sigma$ [12], $M_{\text{BH}}-(\text{bulge central light concentration or } n_{\text{sph}})$ [13], and $M_{\text{BH}}-(\rho_{\text{soi}}$: bulge density at the gravitational sphere-of-influence of it's SMBH) [14], and additionally, established $M_{\text{BH}}-\mu_{0,\text{sph}}$ and $M_{\text{BH}}-(\text{bulge compactness: } \Sigma_{1\text{kpc}}$ and $\rho_{1\text{kpc}})$ relations [14]. These relations form alternatives to estimates M_{BH} in other galaxies, to be used depending on their known property and morphology.

The newly discovered morphology-dependent BH scaling relations have important ramifications for calibration of virial-factor required for reverberation mapping of AGNs, estimation of morphology-aware BH mass function, modelling of SMBH merger rate, and the expected long-wavelength gravitational-wave signals (see [14] for description). Importantly, these relations hold tests and insights for simulations, semi-analytic, and theoretical studies trying to understand BH–Galaxy co-evolution. In an upcoming paper [9] we explore more-realistic color-dependent stellar mass-to-light ratios for our bulge/galaxy masses, update $M_{\text{BH}}-M_{*,\text{sph}}$ relations, and discuss the role of mergers and/or AGN feedback in interpreting these morphology-dependent BH scaling relations.

References

- [1] Akritas, M. G., & Bershady, M. A., 1996, ApJ, 470, 706.
- [2] Anglés-Alcázar, D., et al. 2017, MNRAS, 472, L109.
- [3] Ciambur, B. C., 2015, ApJ, 810, 120.
- [4] Ciambur, B., & Graham, A., 2016, MNRAS, 459, 1276.
- [5] Davis, B. L., et al. 2019, ApJ, 873, 85.
- [6] Fontanot, F., et al. 2006, MNRAS, 373, 1173.
- [7] Graham, A. W., 2016, Galactic Bulges, 418, 263.
- [8] Graham, A. W., 2019, MNRAS, 487, 4995.
- [9] Graham, A., & Sahu, N., 2022, MNRAS, submitted.
- [10] Marshall, M. A., et al. 2020, MNRAS, 494, 2747.
- [11] Sahu, N., et al. 2019, ApJ, 876, 155.
- [12] Sahu, N., et al. 2019, ApJ, 887, 10.
- [13] Sahu, N., et al. 2020, ApJ, 903, 97.
- [14] Sahu, N., et al. 2021, ApJ, arXiv:2110.05037
- [15] Savorgnan, G., & Graham, A., 2016, ApJS, 222, 10.
- [16] Savorgnan, G. A. D., et al. 2016, ApJ, 817, 21.

Short CV



2017: Masters Degree in Engineering Physics, IIT-BHU Varanasi, India
 2021: PhD in Astrophysics, Swinburne University of Technology, Australia
 2021–2022: Postdoctoral Researcher, Swinburne University of Technology, Australia
 2022: Postdoctoral Fellow, University of New South Wales, Australia



INTERSTELLAR MEDIUM, STAR FORMATION, PLANETARY SYSTEMS

Is brown dwarf formation environment-dependent? A case study in NGC 2244

Víctor Almendros-Abad

CENTRA, Faculdade de Ciências, Universidade de Lisboa, Ed. C8, Campo Grande, 1749-016, Lisboa, Portugal

Brown dwarfs (BDs), objects with masses below $0.075 M_{\odot}$, populate the mass spectrum between the realms of stars and planets, being mainly characterized by their lack of hydrogen burning in their cores. Due to their privileged position, BDs offer a unique window into the unknowns of both worlds and their connection.

Since BDs do not burn hydrogen, they never reach the main sequence and keep evolving with time [1]. The boundary between BDs and stars is located at a spectral type of $\sim M6$ when they are young, and moves down to L-types at field ages. Despite this fundamental difference between stars and BDs, BDs are known to follow a similar early evolutionary path (have disks, outflows, ...), and the distribution of stellar properties (e.g. mass, multiplicity, kinematics and spatial configuration) is shared or has a smooth transition into the BD regime [2]. However, it is still not clear how BDs form. There are several proposed scenarios for their formation [2, and references therein]: like a star, from the turbulent fragmentation of the molecular cloud; like a planet from disk fragmentation, with a later ejection from the system due to some dynamical process. It has also been proposed that BDs form due to the truncation of the mass reservoir of higher-mass objects at earlier stages, thanks to mechanisms such as ejection from the embryo of a multiple system or the photo-erosion of their outer layers by a nearby massive star. At higher masses the general consensus is that most BDs form like stars [3], but it is unknown what happens at lower masses and what is the relative importance of each mechanism. Additionally, the efficiency of the four aforementioned BD formation processes is expected to be affected by the environment where the BD is formed [e.g. 4, 5], so by looking for possible variations of the population of BDs with the environment, the BD dominant formation scenarios can potentially be constrained. In particular, high stellar and gas densities and/or presence of a rich population of OB stars are the main environmental properties that are expected to increase the BD formation efficiency.

The question of the effect of the environmental on BD formation has been addressed by searching for differences in the shape of the initial mass function (IMF) in different star-forming regions. The shape of the low-mass side of the IMF is typically parametrized by a power law ($dN/dM \propto M^{-\alpha}$). In the last two decades, several surveys have taken the task of characterizing the population of nearby star-forming regions down to $\sim 10\text{-}20 M_{Jup}$ [e.g. 6]. These surveys have found the IMF to be universal, with no evident sign of cluster-to-cluster variation.

The IMF of these clusters is characterized by $\alpha = 0.6\text{--}1$, and it was found that for each new BD between 2 and 5 stars are formed [7, and references therein]. But the environment of these nearby star-forming regions is defined by low stellar densities and few to none OB stars, which are the main expected environmental drivers of variations in BD formation efficiency. In order to test whether BD formation is affected by its birth environment, we have started a program to study various young clusters characterized by different environmental properties in terms of stellar density and number of OB stars. In this contribution I discussed our preliminary results on the spectroscopic low-mass IMF of the core of NGC 2244, a 2 Myr old cluster located at 1.5 kpc, whose environment is characterized by low stellar densities (similar to nearby star-forming regions) and a rich population of OB stars, therefore being the perfect laboratory where to study the effect of OB stars on BD formation.

Observations and analysis

[7] presented a deep NIR photometric study of the core region of the young cluster NGC 2244. In this contribution we studied the low-mass population of the same region but using spectroscopy at the lower masses.

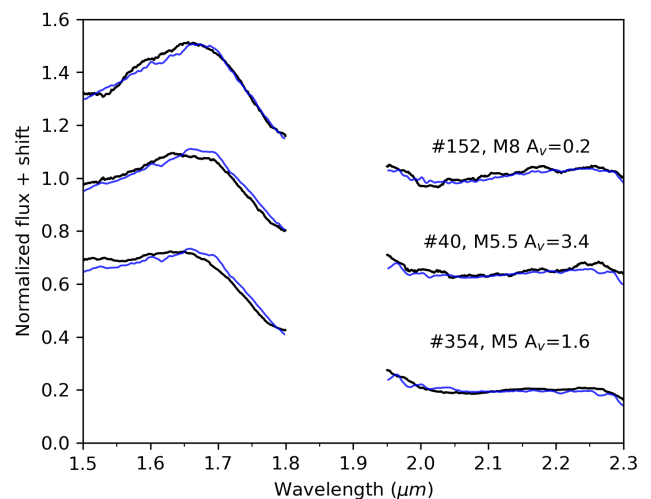


Figure 1: Three of the low-mass members of NGC 2244 with KMOS spectra together with their best fit template.

At higher masses ($0.3\text{--}1.2 M_{\odot}$) we used the member list of Muzic et al. (submitted), where we studied the objects to belong to the entire Rosette nebula by applying the Probabilistic Random Forest (PRF) algorithm using

as input optical to near infrared photometry as well as proper motions from *Gaia* EDR3. We also used archival VIMOS/VLT optical spectroscopy, where the membership came from H- α emission above the accretion threshold.

At lower masses ($<0.3 M_{\odot}$) we obtained near infrared spectroscopy of 85 objects using KMOS/VLT. The spectra were obtained using the *HK* filter ($\sim 1.5\text{--}2.4 \mu\text{m}$), which has a mean spectral resolving power of ~ 1800 . We found 38 of these objects to present a broad shape consistent with being low-mass stars or BDs. For these 38 objects we derived their spectral type and extinction by comparison with spectral templates (see Figure 1).

In order to be confirmed as members they have to present some signature arguing for their youth. We evaluated their youth using gravity-sensitive spectral indices based on the H-band peak feature [8]. We found 32 bona-fide members (M2-M8.5), including, to our knowledge, the first spectroscopically confirmed BDs beyond 1 kpc. In the KMOS brightness range ($J=16.5\text{--}19$ mag), we completed the census of cluster members that were not observed with KMOS by estimating the number of unobserved members using the success rate of the spectroscopic follow up.

Results

Using the compiled member list, we obtained the IMF of the cluster (see Figure 2). The IMF can be fitted by a broken power law, with a mass break at $0.4 M_{\odot}$. At higher masses we found a slope of 2.08 ± 0.06 , which is consistent with the Salpeter slope ($\alpha = 2.35$). At lower masses we found a slope of 1.21 ± 0.13 . This slope is at the steeper side of the typical values found in nearby star-forming regions ($\alpha = 0.6\text{--}1$), although still in agreement within errors. Comparing these results to that obtained in the photometry-only study of the same cluster [1.02 ± 0.04 , 7], we found the new α value to be consistent within errors.

We also evaluated the BD formation efficiency of the cluster through the star/BD ratio, and found this value to be 2.36 ± 0.48 . The star/BD ratio of nearby star-forming regions (2–5) is calculated between $0.03\text{--}0.1 M_{\odot}$, while we estimate that we are only complete down to $\sim 0.045 M_{\odot}$ (see Figure 2), so the derived value is an upper limit of the true value. We also found an indication that the lower mass BDs ($<0.045 M_{\odot}$) are in average closer to the OB stars of the region, but this result can be a bias of

the observed KMOS sample and we are missing a significant fraction of the objects at those masses.

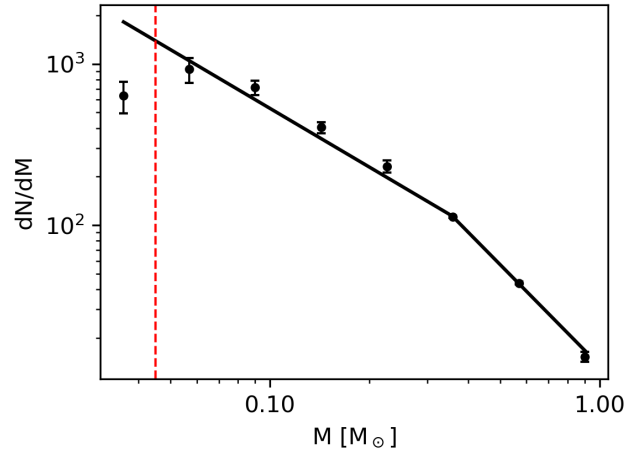


Figure 2: Derived IMF of NGC 2244 together with the fit of a broken-power law, and the estimated completeness of the population ($\sim 0.045 M_{\odot}$).

Summary

We studied the low-mass population of the core region of NGC 2244, a massive young cluster characterized by a rich population of OB stars, in order to test the effect of OB stars on BD formation. We identified 32 new low-mass members of the cluster using near infrared spectroscopy. We found the slope of the low-mass IMF of the region to be steeper than the typical locus of values, although in agreement within the errors. The presented preliminary results could potentially hint BD overproduction on NGC 2244 and calls for the attention of further studies of the region.

References

- [1] Burrows, A., et al., 2001, *RvMP*, 73, 719
- [2] Luhman, K., 2012, *ARA&A*, 50, 65
- [3] Luhman, K., et al., 2007, *Protostars and Planets V*, 443
- [4] Whitworth, A. P., & Zinnecker, H., 2004, *A&A*, 427, 299
- [5] Bonnell, I. A., et al., 2008, *MNRAS*, 389, 1556
- [6] Esplin, T., & Luhman, K., 2019, *AJ*, 158, 54
- [7] Muzic, K., et al., 2019, *ApJ*, 881, 79
- [8] Almendros-Abad, V., et al., 2022, *A&A*, 657, 129

Short CV



2018: Master in Space science and technology, University of the Basque Country, Spain
 2019–present: PhD in Astronomy, Faculty of Science, University of Lisbon, Portugal

Mitigating stellar activity using line selections for Least-Squares Deconvolution

Stefano Bellotti

Institut de Recherche en Astrophysique et Planétologie, Université de Toulouse, France

Stellar magnetic activity represents a serious obstacle to the search and characterisation of small exoplanets with the radial velocity (RV) technique. It contaminates the data sets with spurious signals, known as “jitter”, that can either mimic or hide the presence of a planetary companion [e.g., 1]. This is a crucial aspect when observing M dwarfs, since they are key targets for future planet atmospheric characterisation missions, like Ariel [2]. M dwarfs have indeed favourable properties such as closer habitable zones (increased detection probabilities with RV or transit method) and higher Earth-like planets occurrence rates [3], but can manifest intense magnetic activity resulting in RV signals of hundreds of m s^{-1} , i.e. two orders of magnitude larger than the signature of an Earth-like planet.

The sensitivity toward small planets depends mainly on our ability to filter out activity-induced RV jitter from the data sets. Knowing from previous studies that spectral lines are affected differently by magnetic activity [4], we studied how to reduce effectively the jitter by selecting different sets of lines to use in Least-Square Deconvolution (LSD, [5]). Here, I provide a summary of the line selections for LSD and their impact on the dispersion of RV data sets presented in [6].

Observations

We used optical spectropolarimetric observations of EV Lac (GJ 873). This is a very active M4.0 dwarf, with a rotation period of 4.38 days, and whose magnetic properties were studied by [7] and [8]. The data set comprises 57 observations collected between 2005 and 2016 with ESPaDOnS and NARVAL, two twin spectropolarimeters located at Canada-France-Hawaii Telescope (CFHT) in Hawaii and T el escope Bernard Lyot (TBL) in France, respectively.

The extraction of unpolarised (Stokes I) and circularly polarised (Stokes V) profiles from the spectra was performed with LSD. This numerical technique assumes the spectrum to be the convolution between a mean line profile and a line list or mask, i.e. a Dirac comb describing the arrangement of spectral lines along with their associated properties such as wavelength, depth, excitation potential, and sensitivity to Zeeman effect. We adopted a synthetic mask with $T_{\text{eff}} = 3500 \text{ K}$, $\log g = 5.0 \text{ [cm s}^{-2}\text{]}$, and $v_{\text{micro}} = 2 \text{ km s}^{-1}$, and containing 4216 lines in range 350–1080 nm. By deconvolving the observed spectrum with the mask, we combine the information of thousands of spectral lines and retrieve both a Stokes I and V profile with enhanced signal-to-noise ratio (S/N). The Stokes I profile is then modelled with canonical methods similarly to a cross-correlation function, in order to measure radial velocities.

The following sections describe two approaches to

select specific lines from the mask in order to mitigate the activity-induced RV jitter. The default mask will be referred to as “full” mask, whereas the selections as “sub-masks”. The performance of the sub-masks was assessed by the dispersion of the resulting RV data set, as we distinguished “stable” (low dispersion) and “unstable” (high dispersion) selections. Furthermore, we computed the precision of a sub-mask with 100 Monte Carlo injections of white noise in the spectra and obtaining RV data sets for each case. This way we determined whether a sub-mask was photon noise limited.

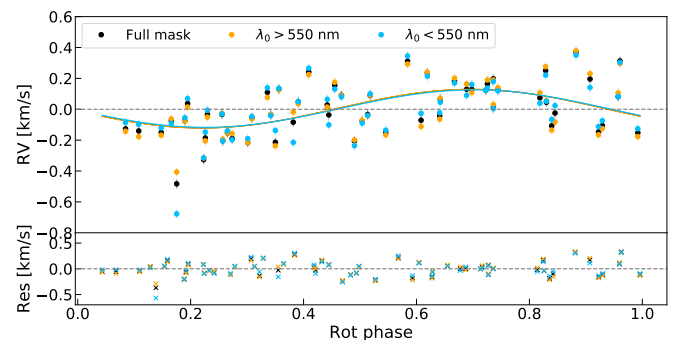


Figure 1: Radial velocity curves and sine fit residuals phase-folded at stellar rotation period for three data sets obtained with three line lists: full, red lines and blue lines. The dispersion is only reduced by 6%, compared to using the full mask, indicating that a straightforward parametric selection is not suitable to mitigate the RV jitter.

Parametric selection

The RV data set computed with the full mask is characterised by a RV RMS of 167 m s^{-1} and a precision of 8 m s^{-1} , indicating that stellar activity is indeed the dominant source of noise. To mitigate such contamination, we first test a direct line selection approach, consisting in splitting the full mask according to the line properties and physical arguments.

The signal from activity surface features like spots is chromatic [9], hence we isolated red ($\lambda > 550 \text{ nm}$) and blue ($\lambda < 550 \text{ nm}$) lines to locate spectral regions where the dispersion is reduced. As illustrated in Figure 1, the RMS increases up to 4% in both cases, compared to the full mask. We selected shallow ($d < 0.6$), intermediate ($0.6 < d < 0.8$) and deep ($d > 0.8$) lines, which should be decreasingly sensitive to convective velocity fields [10]. In this case, we only see an improvement in RV RMS of 6% with the deep sub-mask. Finally, we used the Land e factor (g_{eff}) to distinguish between magnetically sensitive ($g_{\text{eff}} > 1.2$) and insensitive ($g_{\text{eff}} < 1.2$) lines, as past studies reported measurable Zeeman broadening for EV Lac [11]. We note a boost in RMS of 20% and a decrease of

10% for the two cases, respectively. We therefore conclude that a line parametric selection does not yield a sub-mask that is substantially more stable than the full mask.

Randomised selection

A second approach consists in building a large number of sub-masks by selecting lines randomly from the full mask, and storing the RMS of the associated RV data set. From the resulting distribution of RV RMS, we can discriminate between stable and unstable sub-masks. In practice, we separate three groups of stable sub-masks depending on whether their RMS is lower than the 10th, 5th, and 1st percentile, and we merge the lists to obtain three sub-masks for each percentile group.

We benchmarked our analysis on the 2010 data set of EV Lac. The dispersion and precision obtained using the full mask are 182 and 4 m s⁻¹, respectively. The three percentile sub-masks lead to a RMS decrease of at least 50%, but the precision increases by a factor of three, as a consequence of the lower number of lines used in LSD. For this reason, we applied the algorithm multiple times and merged the most stable sub-mask among the three percentile-defined ones. Merging the output of three runs allowed us to obtain a sub-mask yielding the same benefit in RMS, while keeping the precision on a 5 m s⁻¹ level.

We studied the portability of the benefit over different data sets and activity levels. We used the 2007 and 2006 data sets of EV Lac, finding a similar 50% RMS improvement in the former case, while a severe degradation (42%) in the latter case, due to the small number of observations (7 in total) over which the sub-masks are investigated. We then searched for stable sub-masks using observations of AD Leo (active) and DS Leo (moderately active). In both cases, we obtained an RMS reduction down to the instrumental stability of ~ 30 m s⁻¹ [12], starting from 110 and 40 m s⁻¹, respectively. In all cases, the photon noise remained significantly smaller than the dispersion, meaning that the mitigation is indeed performed on the activity contamination.

We also tested whether the algorithm can be used in the opposite direction, i.e. to single out lines that are more sensitive to noise sources. Using the 2010 data set of EV Lac, we built sub-masks with an associated increase in RMS by a factor of two and with an enhanced phase-modulation. This could be used, for instance, to better constrain the stellar rotation period.

Finally, we injected synthetic planetary signals of 0.3–0.9 M_{Jup} on a 10 days circular orbit around both EV Lac and DS Leo. No planet is detectable using the full mask on EV Lac, whereas the percentile sub-masks allow the signal to emerge and the injected RV semi-amplitude to be retrieved within error bars (see Figure 2). For DS Leo,

the planetary signal is consistently extracted in all cases, owing to the lower activity level of the star. This demonstrates that the output sub-masks do not suppress the planetary signal, neither in a high nor a low stellar activity scenario.

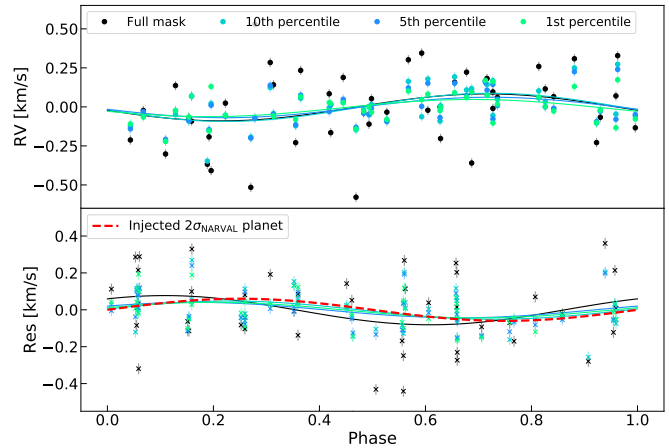


Figure 2: Results of the planet injection tests. Top: RV data phase-folded at stellar rotation period, Bottom: RV residuals of the activity sine fit phase-folded at planet orbital period. The signal induced by a 0.6 M_{Jup} mass planet on a 10 days orbit around EV Lac is retrieved within uncertainties with the sub-masks generated with our algorithm, contrarily to the full mask.

Conclusions

We studied the impact of different line selections to compute RV data sets with LSD, in order to find lines that mitigate the jitter and could enable more reliable exoplanet detections around active M dwarfs. We reached the following conclusions: 1) a direct selection based on line parameters is not sufficient to reduce the jitter considerably and 2) a randomised selection allows to build sub-masks that reduce the jitter by at least 50% and that are portable over different data sets and activity levels. The method is also applicable to find lines which are more sensitive to activity or when planetary signals are included, without the danger of suppressing their signal.

References

- [1] Queloz, D., 2001, A&A, 379, 279-287
- [2] Tinetti, G., 2018, ExA, 46, 135-206
- [3] Gaidos, E., 2016, MNRAS, 457, 2877
- [4] Dumusque, X., 2018, A&A, 620, A47
- [5] Donati, J. F., MNRAS, 291, 658
- [6] Bellotti, S., 2022, A&A, 657, A107
- [7] Morin, J., 2008, MNRAS, 390, 567
- [8] Shulyak, D., 2019, A&A, 626, A86
- [9] Reiners, A., 2010, ApJ, 710, 432
- [10] Reiners, A., 2016, A&A, 587, A65
- [11] Johns-Krull, C. M., 1996, ApJ, 459, L95
- [12] Moutou, C., 2007, A&A, 473, 651

Short CV



2013–2017: BSc in Physics, University of Pavia, Italy
 2017–2019: MSc in Astrophysics, Niels Bohr Institute, Denmark
 2020–present: PhD in Astronomy, IRAP, Université de Toulouse, France
 2022–present: Visiting PhD trainee, ESTEC-ESA, The Netherlands

Sublimating Ices Feeding Forming Planets

Alice S. Booth

Leiden Observatory, Leiden University, 2300 RA Leiden, The Netherlands

Overview

With over 5000 exoplanets detected[¶] around nearby stars it is necessary to take a step back and study their birth environments - protoplanetary disks. The wide array of planet sizes, planet compositions and orbital architectures are the outcome of the planet formation process which, is set by the physical and chemical conditions in the disk. An important tool to trace the formation location of a planet is its elemental composition. The relative abundances of the primary volatiles, carbon and oxygen, in the gas and ice in disks vary as a function of radius [1]. Therefore, a planet's composition should reflect its formation location in the disk relative to the key snowlines.

Tracing disk composition with ALMA

Disks are made up of dust, gas and ice and with the Atacama Large Millimeter Array (ALMA) we can probe the distribution of the millimeter-sized dust and molecular gas on 10-100 au scales, e.g., [2, 3]. Observations of the dust show clearly that disks most often have rings of dust and less frequently asymmetries (see Figure 1 for examples of the continuum emission from the HD 100546 and IRS 48 disks [4, 5]). ALMA observations of gas in disks probe the composition of the warm molecular layer and the primary gas tracer in disks is carbon monoxide (CO). Initial observations revealed a depletion of CO in disks relative to the value in the interstellar medium. In addition to this, the complementary gas tracers, e.g., C₂H, CS and SO show that in most disks the gas at >10 au is depleted in both carbon and oxygen with an overall elevated C/O > 1, e.g., [7]. The depletion of volatiles can be partly explained by the chemical conversion of CO to CO₂ and more complex ices [8], but another mechanism is required to fully match the observations.

Volatile redistribution in disks

The impact of the dust evolution on disk chemistry is becoming increasingly more pertinent to understand. As disks evolve the smaller micron-sized dust grains will grow to at least millimetre sizes. During this process, the grains will decouple from the gas, settle in the mid-plane and drift inwards. This process also removes simple molecules from the gas as they will freeze out onto the surfaces of these dust grains. The inward transport of these ices leaves the outer disk volatile poor but will enrich the inner planet-forming zone (< 10 au) [9]. But, if this inward drift is stopped then these volatiles will remain trapped in ices in the outer disk. The dust traps (like those seen in Figure 1) are indeed common and are likely caused by the presence of giant planets or low mass companions located on orbits within the disk cavities. These dust traps are also ice traps sequestering volatiles in the outer disk and preventing them from reaching the inner (terrestrial) planet-forming zone of the disk < 10 au.

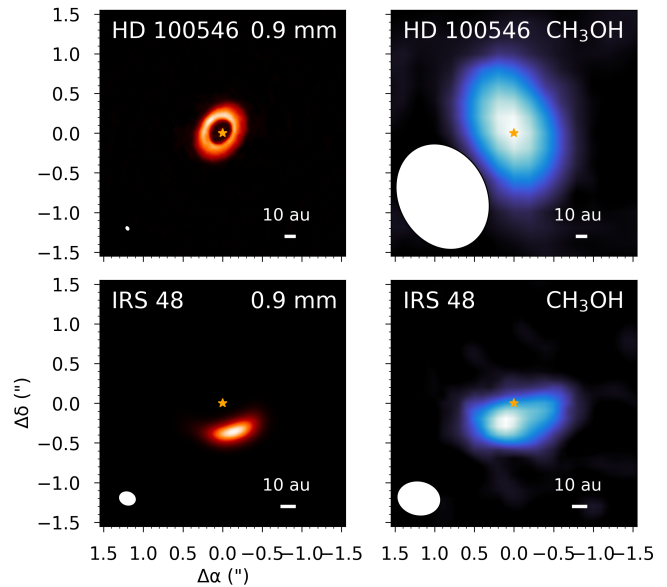


Figure 1: Intensity maps of the 0.9 mm continuum and CH₃OH emission which indicates dust temperatures > 100 K at the cavity edge in the HD 100546 and IRS 48 disks [4, 5, 6, 12]. Angular resolution of the observations are shown via ellipses in the bottom left corner of each panel.

Sublimating ice traps

The clearest evidence for these ice traps was seen via the detections of methanol (CH₃OH) in the warm Herbig transition disks HD 100546 and IRS 48 [6, 10]. Here, although the dust is trapped at 10's of au, the dust at the cavity edge is heated by irradiation from the star allowing for the thermal sublimation of CH₃OH and likely H₂O (100-150 K). An array of simple oxygen-bearing molecules have also been detected in these disks including SO, SO₂ and/or NO [11, 12, 13]. These species all have a common gas-phase formation path via the OH radical, a product of the photodissociation of H₂O. In this region of the disk, we expect the full volatile content to be in the gas phase and is thus observable to us with ALMA. This results in a C/O ≤ 0.5: the opposite of most other disks. The observations of IRS 48 are the most striking since this disk has an asymmetric dust-trap where all of the larger grains and ice reservoir are located on one side of the disk (see Figure 1).

An inherited organic reservoir

Disks inherit their dust, gas and ice from the earlier stages of star formation. But, it is not clear how pristine this material is, i.e. do all the ices sublimated during the formation of the disks or if some of the interstellar ices are preserved. The detection of CH₃OH in the warm Herbig disk HD 100546 was the first clear evidence that some ices in disks are preserved from earlier

[¶]<https://exoplanetarchive.ipac.caltech.edu/>

times. CH_3OH can only form efficiently on the surfaces of cold (20 K) dust grains and not via gas-phase processes [14]. But, the dust in these disks is too warm to make CH_3OH locally. Further work has detected the more complex molecules dimethyl ether (CH_3OCH_3) and tentatively methyl formate (CH_3OCHO) in Class II disks for the first time [13]. These detections are in the IRs 48 system where again, the ices are sublimating at the dust cavity edge. The ratio of CH_3OCH_3 to CH_3OCHO is consistent with what has been measured in other environments [16]. This again strongly supports the ice inheritance of ices from the cold dark cloud stage.

Impact on forming planets

The composition of a planet is set by the local disk material it accretes. In disks like HD 100546 and IRS 48 where the dust trap is located close enough to the star to allow for thermal ice sublimating, the gas in the cavity will have a low C/O ratio ≈ 0.5 (or even lower if O abundances are

enhanced due to pebble drift). This means that the gas making its way into the inner ($\lesssim 1$ au) planet-forming zone of the disk will be oxygen-rich and the small grains bare. The dust traps are located at ≈ 20 -50 au from the central stars, so the ice sublimation is at a much further radius than the expected H_2O snowline in a full disk. This shows clearly that the dust evolution has profoundly affected the thermal structure of the disk and thus the chemistry. But, this all depends on where the dust trap is located and the temperature of the host star. Since, other transition disks, e.g., PDS 70, do not show these chemical signatures of ice sublimation [15]. Therefore, in the PDS 70 disk, the planets in the cavity are likely accreting gas with a $\text{C/O} > 1$. The detections of complex organic molecules (COMs) in HD 100546 and IRS 48 have shown that disks can inherit ices from the earlier stages in star formation. This result sets the precedent that all disks, and as a consequence all exoplanet systems, should all have the ingredients necessary for prebiotic chemistry.

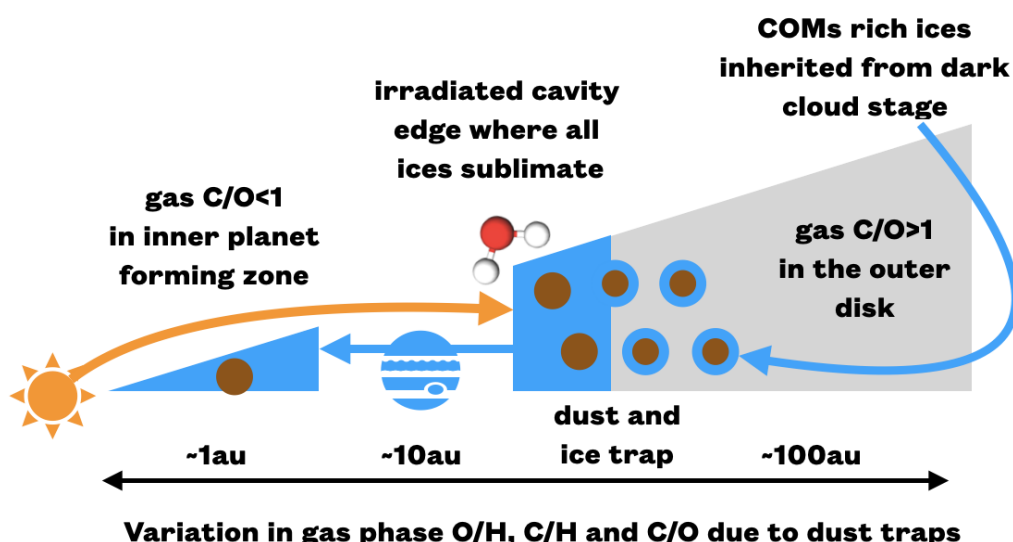


Figure 2: Cartoon showing the impact of a sublimating ice trap on the gas-phase C/O in a disk.

References

- [1] Öberg, K.I., et al. 2011, ApJL, 743, L16
- [2] Andrews, S.M., et al. 2018, ApJL, 869, L41
- [3] Öberg, K.I., et al. 2021, AJSS, 257, 1
- [4] Pineda, J.E., et al. 2019, ApJ, 871, 48
- [5] van der Marel, N., et al. 2013, Science, 340, 1199
- [6] Booth, A.S., et al. 2021, Nature Astronomy, 5, 684
- [7] Miotello, A., et al. 2019, A&A, 631, A69
- [8] Bosman, A.D., et al. 2018, A&A, 618, A182
- [9] Krijt, S., et al. 2020, ApJ, 899, 134
- [10] van der Marel, N., et al. 2021, A&A, 65, L5
- [11] Booth, A.S., et al. 2018, A&A, 611, A16
- [12] Booth, A.S., et al. 2021, A&A, 65, L6
- [13] Brunken, N.G.C., et al. 2022, A&A, 659, A29
- [14] Fuchs, G. W., et al. 2009, A&A, 50, 629
- [15] Facchini, S., et al. 2021, ApJ, 162, 99
- [16] Coletta, A., et al. 2020, A&A, 641, A54

Short CV



2016: Bsc in Physics, University of Aberdeen
 2016–2020: PhD in Astrophysics, University of Leeds
 2020–present: Post-Doctoral Researcher, Leiden Observatory, Leiden University

The formation of massive close binaries: is the migration scenario viable?

Emma Bordier

Institute of Astronomy, KU Leuven, Celestijnenlaan 200D, 3001, Leuven, Belgium
European Southern Observatory (ESO), Alonso de Cordova 3107, Vitacura, Santiago, Chile

In contrast to the low- and intermediate-mass stars, star formation in its high-mass ($M_{init} > 8 M_{\odot}$) regime is still very uncertain. The formation of young massive stars occurs embedded in their obscured natal clouds and is rapid, making observing them very challenging. In addition, it is now known that most massive stars experience multiplicity (presence of one -or more- stellar companion(s)) even during their earliest phases [1, 2]. Multiplicity scales with mass and reaches almost 100% for main sequence OB stars, a fact that cannot be omitted while studying the early stages of massive stars. A large fraction of massive stars appear to host at least one *close* companion (< 1 au), meaning that the most likely end product of massive star formation is a rather close binary (or higher-order system). An important question to be addressed by the community is how these multiples were formed. It is likely that they were initially born as a wide system that evolved into a tighter one, the consequence of an inward migration of the companion(s) [3]. Understanding high-mass multiple star formation in detail would simplify the predictions of their final fate, as for example core collapse supernova or gamma ray bursts. Observational studies of massive young binaries, either at the Massive Young Stellar Object (MYSO) or pre-main sequence stage are essential to gather information about the various formation theories in place.

Up to now, numerous high-resolution imaging studies have been conducted to explore the early multiplicity of young stars probing relatively large separations (from ~ 500 to $\sim 15\,000$ au). However, little is known about the close environment (< 100 au) of massive forming stars. In these proceedings, I summarise the analysis published in [4], where we bring novel observational constraints about the multiplicity of six young massive stars (1 – 100 au) in the M17 nearby star-forming region and discuss the most likely channels for the formation of such multiple systems.

The M17 sample

Long baseline near infrared interferometry enables to spatially resolve binaries and get unique astrometric information. In particular, the GRAVITY instrument at the VLTI is able to detect rather close and faint companions down to ~ 1 mas and $\Delta\text{mag}=4$. Our sample consists of six young O stars in the M17 complex, the brightest ones in the region and for which reliable measurements of the radial velocities and well defined spectral types are available in the literature (Figure 1). We obtain six snapshot observations along with six medium resolution spectra ($R\sim 500$) with GRAVITY. The acquisitions were preceded by the observations of a point-source calibration star, close to the target physically and in terms of spectral type, to accurately correct the atmospheric and

instrumental transfer function.

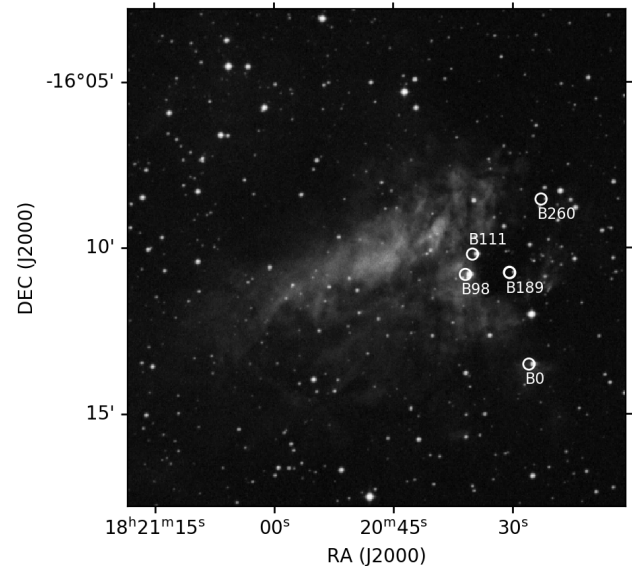


Figure 1: Digitized Sky Survey (DSS) image on which the M17 GRAVITY sources are labelled in white.

Methods

The main interferometric observables, the visibility amplitudes ($|V|$) and closure phases (CP) were modelled using the python module PMOIRE. From the $|V|$ and CP, we derive the variable parameters of flux ratio (f) and the source positions ($\Delta\alpha; \Delta\beta$) by performing binary model fitting. Binaries produce two fringe packets that will overlap to produce a sinusoidal signal in the visibility amplitudes. The separation between the peaks relates to the binary separation while the minimum visibility provides a measurement of the flux ratio between components. The CPs are sensitive to the asymmetries in the source distribution. A variety of models has been explored for each source, iteratively increasing the multiplicity order (single, binary, triple...) and complexity (e.g fully resolved component). We infer the mass of the objects comparing the calibrated K -band spectra to a family of atmosphere models and evolutionary tracks (the full method can be found in [4]).

Results - Multiplicity and companion fraction

We find that 100% of the targeted sources host at least one companion in the probed separation range (1-100 mas): three are binaries and three are triples. When adding the five spectroscopic companions reported in the literature, a total of 14 companions orbit the six systems yielding a companion fraction (CF) of 2.3 ± 0.6 (see Fig-

ure 2). These observational results are compatible with the multiplicity fractions (MF) and CFs measured in other galactic regions for stars with $M > 20 M_{\odot}$ [1, 5, 6]. The young age of M17 and the cluster environment tends to show that massive star formation results in a multiple system with at least two companions on average.

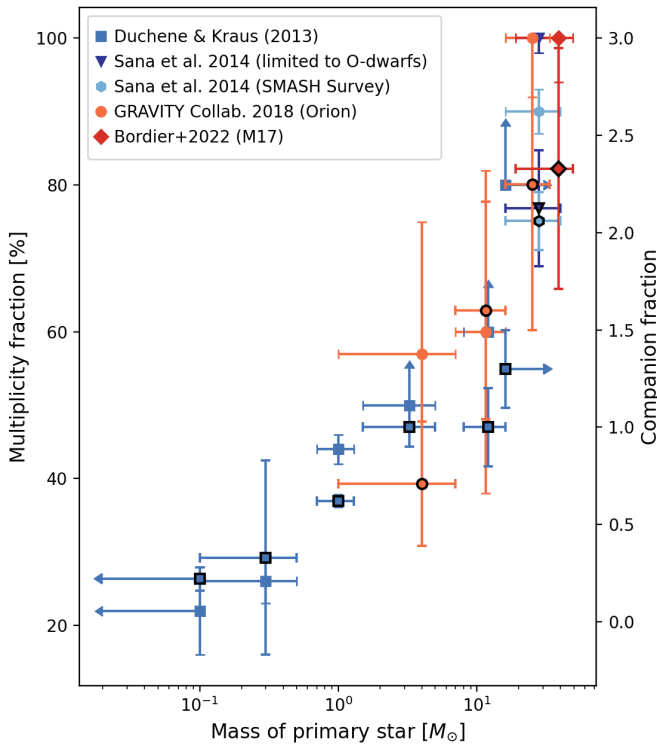


Figure 2: MF and CF measured with GRAVITY for the six O-stars in M17 (red) as a function of the primary mass. For reference, values of other studies are also presented for different primary mass ranges. For a given symbol, the black marker stands for the companion fraction while the plain color refers to the multiplicity fraction.

Results - Separation distribution and mass ratio

The detected interferometric companions span a wide range of separations, ranging from 1 mas to ~ 70 mas. Two companions were found at very close distances (around 1 mas), five are located at intermediate separations ($4 < a < 20$ mas) and one is relatively distant (~ 70 mas). Similarly, we investigate the brightness properties. Flux ratios are converted into brightness contrasts and displayed as a function of the companion separation. Again, no clear trend can be identified and rather shows the contrasting companion profiles. There is a gap in the

signal with a significant lack of detection below $\Delta \text{mag} \sim 2$ for companions located within 3 mas, which are ambitious sensitivities to reach with GRAVITY. Overall, these results show the broad variety of companions surrounding these pre-main sequence massive stars.

Consequences for the star formation scenario

A successful model for massive star formation should reproduce the proximity between the components and the high-degree of multiplicity observed in older populations of massive stars. To date, only two main theoretical approaches were explored to support massive star formation: monolithic collapse of turbulent cores and competitive accretion. Lately, it has been shown evidence for an inward migration of stars as a function of a cluster age, one of the numerous processes that can favour the hardening of binaries [7]. While this mechanism can occur in both theories, collaborators suggest that massive binaries are formed in wide pairs and then evolve into tight systems following a timescale of ~ 2 Myrs [8, 7]. Detecting companions within 2 mas from the primary star in M17 could indicate that protostellar cores formed at the edges of the accretion disk migrated over time and are entering the spectroscopic regime, as suggested by Oliva [9] and Ramírez-Tannus [7]. Additionally, the presence of companions at wider distances (dozens of mas) is also a valid detection featuring the migration process. In fact, disk fragmentation occurring in the vicinity of the central forming star may boost the formation of prestellar cores at similar distances (~ 100 au) [9]. Given the young age of M17 (~ 1 Myr), a combination of mechanisms is at play to set the final structures of the cluster. We seek to investigate whether such behaviour extends to the youngest and faintest objects in the region, confirming or discrediting the proposed scenario. If the migration scenario is correct, we expect that most of the objects have at least one detectable companion within the expected size of the accretion disk. A non-detection of companions within ~ 200 au would invalidate the migration scenario.

References

- [1] Duchêne, G., & Kraus, A., 2013, ARA&A, 51, 1
- [2] Koumpia, E., et al. 2021, A&A, 654, A109
- [3] Meyer, D.M.-A., et al. 2018, MNRAS, 473, 3
- [4] Bordier, E., et al. 2022, A&A, 663, A26
- [5] Gravity Collaboration 2018, A&A, 620, A116
- [6] Sana, H., et al. 2014, ApJ, 215, 15
- [7] Ramírez-Tannus, M.C., et al. 2021, A&A 645, L10
- [8] Sana, H., et al. 2017, A&A, 599, L9
- [9] Oliva, G. A., & Kuiper, R., 2021, A&A, 644, A41

Short CV



2014-2017: BSc in Fundamental Physics, Université Paris-Saclay
 2017-2019: MSc in Astronomy and Astrophysics, Observatoire de Paris
 2019–present: PhD in Astronomy, KU Leuven and ESO, Belgium and Chile
 2020–present: ESO Studentship Programme

Revealing a clustered region of massive star formation through NIR jets using VLT instruments

Rubén Fedriani

Department of Space, Earth and Environment, Chalmers University of Technology, SE-412 96 Gothenburg, Sweden

The formation of massive stars ($M_* > 8 M_\odot$) is a process that is not yet clearly understood. There are many observational challenges preventing us from uncovering the mechanisms behind their birth, such as the limited number of high-mass young stellar objects (HMYSOs), their location at large distances (typically a few kiloparsecs), and high visual extinction [see, e.g. 1, 2, for recent reviews]. We do know that, similarly to their low-mass counterparts, HMYSOs eject great amounts of material in the form of bipolar outflows and jets [e.g. 3, 4]. These outflows are intrinsically related to the process of accretion onto the protostellar surface [5, 6, 7]. Thus, jets and outflows are crucial for pinpointing the location of massive protostars and providing insights into the physical processes unfolding in the extinguished regions.

When observing in the near infrared (NIR) regime, the driving source is usually not accessible as it is very often totally obscured. However, it is possible to observe the jets driven by massive young stars in the NIR and these can provide a wealth of information about the star-forming complex. Moreover, the excellent angular resolution usually achieved in this regime allows us to probe the collimated jet and individual knots. Molecular hydrogen (H_2) is a particularly good shock tracer as it is the primary coolant in the NIR and its emission can be extended over spatial scales of several parsecs [8, 9, 10, 11, 12], displaying numerous strong emission lines. In the K-band (1.9 – 2.5 μm) in particular, the strongest transition is the $H_2 1 - 0 S(1)$ at 2.12 μm , which has been used in many studies to probe the jet morphology in massive protostellar environments [13].

HMYSO accretion is indeed revealed by their outflows, extending parsecs away from the star, but also through reflected light in their outflow cavity walls [14]. This reflected light emission can further reveal the YSO nature when no clear association can be done with their outflows. In particular, the $Br\gamma$ at 2.16 μm is an excellent tracer of young protostars as it probes phenomena occurring very close to the YSO. The $Br\gamma$ line has been detected at the base of powerful jets driven by a HMYSO [15], as well as in accretion discs in a sample of HMYSOs [16].

When NIR is combined with other (usually longer) wavelengths, one can tell the different parts of the story. Figure 1 top panel (a) shows an RGB image from the Hubble Space Telescope where the jet driven by the massive protostar G35.2-0.74N is clearly seen. In the bottom panel (b), a multi-wavelength composite is shown where the NIR traces the shocked material as revealed

by H_2 2.12 μm and $[FeII]$ at 1.64 μm and the free-free radio emission at 6 cm from the powerful outflow.

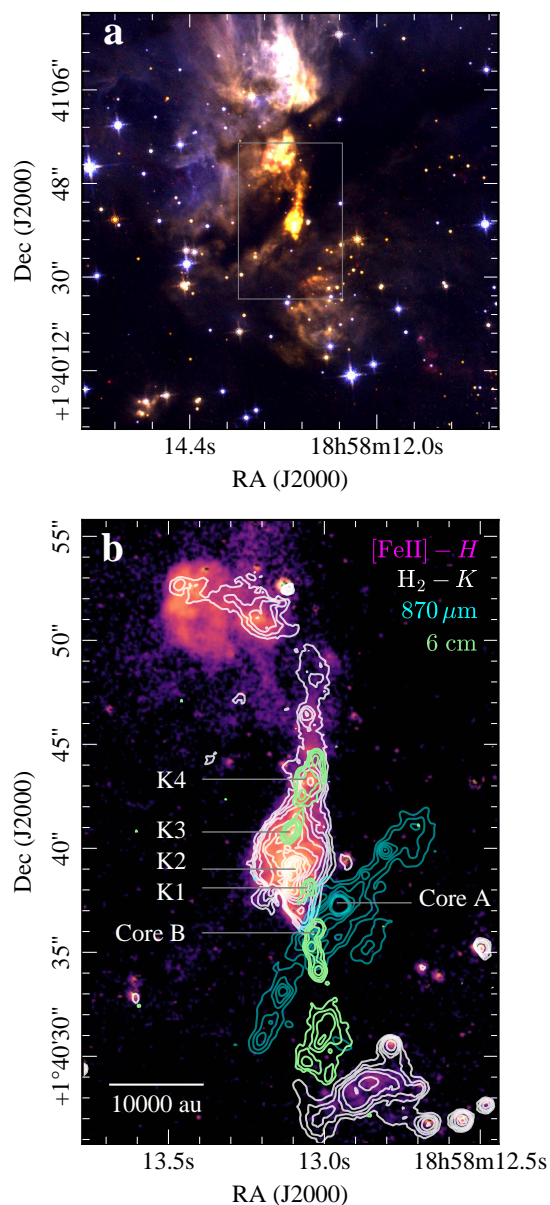


Figure 1: G35.2-0.74N star formation complex. **a** Three colour composite HST image, revealing the jet from the massive protostar. Red channel is the $[Fe II]$ 1.644 μm , green channel is the H 1.600 μm , and blue channel is the J 1.100 μm . **b** Composition of the HST/WFC3 (violet) image, VLT/ISAAC (white contours), ALMA (cyan), and VLA (green) datasets. In both panels, north is up and east is left. Taken from Fedriani et al. [17].

The morphology of the IRAS 18264-1152 region.

We aim to probe the IRAS18264-1152 high-mass star-forming complex in NIR through H₂ jets to analyse the morphology and composition of the line emitting regions and to compare with other outflow tracers [18].

We observed the H₂ NIR jets via K-band (1.9 μm–2.5 μm) observations obtained with the integral field units VLT/SINFONI and VLT/KMOS. VLT/SINFONI provides the highest NIR angular resolution achieved so far for the central region of IRAS18264-1152 (~ 0.2''). We compared the geometry of the NIR outflows with that of the associated molecular outflow, probed by CO (2–1) emission mapped with the Submillimeter Array. Figure 2 shows a radial velocity map using the IFU KMOS where the different outflows are outlined.

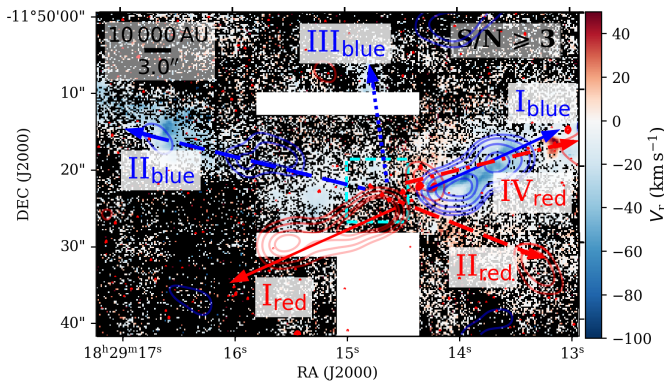


Figure 2: Velocity map for IRAS18264-1152. Taken from Costa Silva et al. [18].

We identify nine point sources in the SINFONI and KMOS fields of view. Four of these display a rising continuum in the K-band and are *Brγ* emitters, revealing that they are young, potentially jet-driving sources. The spectro-imaging analysis focusses on the H₂ jets, for which we derived visual extinction, temperature, column density, area, and mass. The intensity, velocity, and excitation maps based on H₂ emission strongly support the existence of a protostellar cluster in this region, with at least two (and up to four) different large-scale outflows, found through the NIR and radio observations. We compare our results with those found in the literature and find good agreement in the outflow morphology. This multi-wavelength comparison also allows us to derive a stellar density of ~ 4000 stars pc⁻³. We also measure and fit its spectral energy distribution (SED) using the python package *sedcreator* [19]. Figure 3 upper panel shows the best fit for this source while the logo of the package is shown on the lower panel.

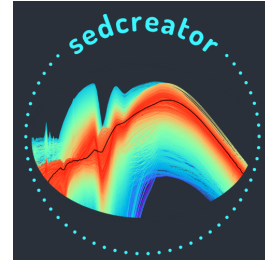
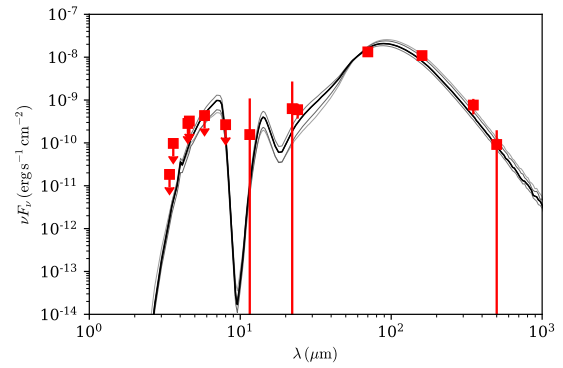


Figure 3: Upper: Velocity map for IRAS18. Lower: Best SED fit and logo for *sedcreator*. Taken from Costa Silva et al. [18].

Conclusions

Our study reveals the presence of several outflows driven by young sources from a forming cluster of young, massive stars, demonstrating the utility of such NIR observations for characterising massive star-forming regions. Moreover, the derived stellar number density together with the geometry of the outflows suggest that stars can form in a relatively ordered manner in this cluster.

References

- [1] Tan, J. C., Beltrán, M. T., et al. 2014, *Protostars and Planets VI*, 149
- [2] Rosen, A. L. & Krumholz, M. R., 2020, *AJ*, 160, 78
- [3] Frank, A., et al. 2014, *Protostars and Planets VI*, 451
- [4] Bally, J., 2016, *ARAA*, 54, 491
- [5] Blandford, R. D., & Payne, D. G., 1982, *MNRAS*, 199, 883
- [6] Pudritz, R. E., & Norman, C. A., 1983, *ApJ*, 274, 677
- [7] Shu, F., et al. 1994, *ApJ*, 429, 781
- [8] Davis, C. J., et al. 2004, *A&A*, 425, 981
- [9] Caratti o Garatti, A., et al. 2008, *A&A*, 485, 137
- [10] Davies, B., et al. 2010, *MNRAS*, 402, 1504
- [11] Caratti o Garatti, A., et al. 2015, *A&A*, 573, A82
- [12] Fedriani, R., et al. 2018, *A&A*, 616, A126
- [13] Gredel, R., 2006, *A&A*, 457, 157
- [14] Fedriani, R., et al. 2020, *A&A*, 633, A128
- [15] Caratti o Garatti, A., et al. 2016, *A&A*, 589, L4
- [16] Koumpia, E., et al. 2021, *A&A*, 654, A109
- [17] Fedriani, R., et al. 2019, *Nature Communications*, 10, 3630
- [18] Costa Silva, A. R., et al. 2022, *A&A*, 659, A23
- [19] Fedriani, R., et al. 2022, *arXiv:2205.11422*

Short CV



2009–2014: Bachelor in Mathematics, University of Cadiz, Spain
 2014–2015: Master in Astrophysics, University Complutense of Madrid, Spain
 2015–2020: PhD in Astrophysics, University College Dublin, Ireland
 2019–2021: CICO Postdoctoral Fellow, Chalmers University of Technology, Sweden
 2021–2022: Marie Skłodowska-Curie Actions Fellow (MSCA-IF), Chalmers University of Technology, Sweden (grant No 101032092)

The Mass of Young Stars likes to play Hide & Seek

Eleonora Fiorellino

Konkoly Observatory, Research Centre for Astronomy and Earth Sciences, Eötvös Loránd Research Network (ELKH), Konkoly-Thege Miklós út 15-17, 1121 Budapest, Hungary

Star formation is not an efficient process. Typical values of efficiency for low-mass stars ($< 2M_{\odot}$) ranges between 0.20 and 0.40 [1, and references therein]. At the same time, the mass accretion rate (\dot{M}_{acc}) measured for Class II young stars (or Classical T Tauri stars, CTTs) are too small ($10^{-7} - 10^{-12} M_{\odot} \text{yr}^{-1}$, [2]) to build solar-type stars, when integrated for the observed timescales (0.5 – 2 Myr, [3]). The question which naturally comes up is how stars gain their mass during their formation from the prestellar cores collapse to the main sequence entrance, through the magnetospheric accretion scenario [4]. We believe that the most effective way to answer this question is to investigate the mass accretion rate during the early stages of the star formation (Class 0 and I).

We will focus on Class I young stellar objects (YSOs), the evolutive stage of the star formation process when the forming star is still surrounded by the envelope, as in the previous stage (Class 0). However, even if the spectral energy distribution (SED) of Class I is still dominated by the IR-excess, it is possible to observe the photosphere contribution in the near-IR (NIR). In particular, we will discuss the relation between \dot{M}_{acc} , the disk mass (M_{disk}), and the stellar mass (M_{\star}) for a sample of nearby (< 500 pc) Class I YSOs.

The $\dot{M}_{acc} - M_{\star}$ relation

The most precise method to compute $\dot{M}_{acc} = \frac{5 L_{acc} R_{\star}}{4 G M_{\star}}$ [4] of young stars is by measuring L_{acc} directly from the Balmer-jump in the ultra-violet (UV), and by computing the stellar parameters from the theoretical evolutive models. As a consequence, \dot{M}_{acc} has been well studied in a systematic manner for optically visible Class II sources (e.g. [2]), while characterizing accretion in Class I is challenging due to large extinctions, with only a handful of sources observed (see [5]). The situation changed after empirical relations between the accretion luminosity L_{acc} and NIR accretion tracers fluxes were computed with unprecedented small errors [9]. These empirical relations were used to analyze KMOS observations of Perseus NGC1333 cluster (< 1 Myr), providing the only \dot{M}_{acc} survey in Class I YSOs [6]. This study consists currently in the largest sample of Class I for which the accretion luminosity (L_{acc}), the stellar parameters, and, thus, \dot{M}_{acc} are computed. According to these data, Class I \dot{M}_{acc} in NGC1333 is larger up to 2 orders of magnitude in log-scale than Class II, where the most accreting objects are the most veiled ones. However, to draw robust conclusions on Class I in general, further observations are needed.

We selected a sample of 50 YSOs among the nearby (< 500 pc) Class I [7] for which the veiling, the apparent magnitude, and the $\text{Br}\gamma$ equivalent width (EW) were al-

ready measured. We computed their distances using *Gaia dr2* results on single sources, when available, or on the relative star-forming region, and we used them to calculate the $\text{Br}\gamma$ flux from the EW. We used SED-BYS v.2.0 python-based package [8] to extract photometry and build SEDs from which we computed the bolometric luminosity (L_{bol}) [6]. Assuming the age of the sources between the birthline and 1 Myr, we adopted a self-consistent method which links together L_{bol} , $L_{\text{Br}\gamma}$ and IR colors to analyse Class I protostars. In this way, for each protostar, we derived the spectral type (SpT), the extinction (A_V), the stellar radius (R_{\star}), M_{\star} , and L_{acc} (e.g., [5],[6]). Finally, we estimated \dot{M}_{acc} , finding values between $\sim 10^{-8}$ and $5 \times 10^{-5} M_{\odot}/\text{yr}$.

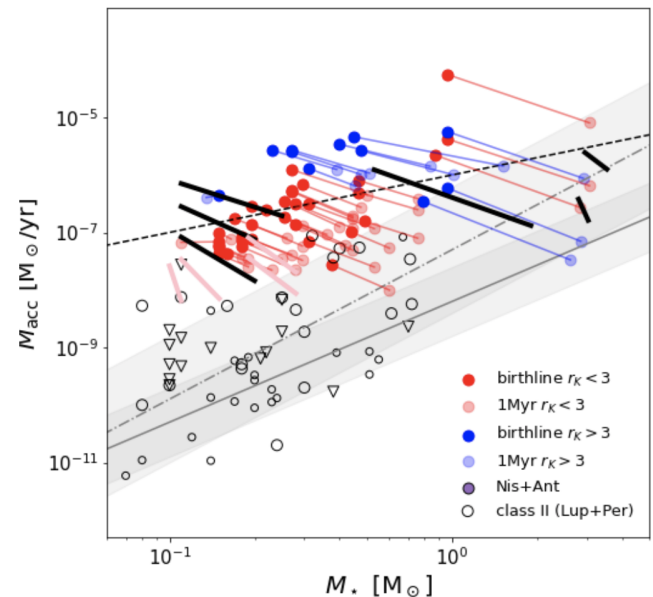


Figure 1: The $\dot{M}_{acc} - M_{\star}$ distribution of Class I (red and blue as described by the legend) compared with the same distribution on Class II (empty circles). Pink and black segments show the low-veiled ($r_K < 3$) and high-veiled ($r_K > 3$) mass accretion rates for Perseus Class I [6]. The grey solid line shows the best fit for the Lupus Class II sample [9]. The grey dashed-dotted line shows the best fit for Perseus Class II sample [6]. The dashed black line represents a linear relation with a unitary slope. Figure taken from Fiorellino et al. 2022, submitted.

Figure 1 shows the distribution $\dot{M}_{acc} - M_{\star}$. The fact that \dot{M}_{acc} is larger in Class I than in Class II is here confirmed and enhanced. In particular, we note that Class I \dot{M}_{acc} is larger than for Class II with similar masses for low-mass sources (up to $2.5 M_{\odot}$), while sources with $M_{\star} > 2.5 M_{\odot}$ show accretion rates compatible with Class II distribution. Considering only low-mass sources, we note

that all the highly veiled Class I in our sample have $\dot{M}_{acc} > 10^7 M_{\odot}/\text{yr}$. Because of the uncertainty on the age, we did not fit the Class I distribution (red and pink filled circles). However, we plot a linear relation (dashed black line) with a unitary slope to guide the reader observing that Class I seem to present a flatter distribution with respect the Class II sources (empty circles).

The $\dot{M}_{acc} - M_{disk}$ relation

For 33 out of the 50 Class I we analyzed, we have collected measurements of suitable flux densities at (sub)millimeter wavelengths across the literature and the archival interferometric data. Assuming optically thin regime, we calculated the dust mass with equation: $M_{dust} = \frac{D^2 F_{\nu}}{\kappa_{\nu} B_{\nu}(T_{dust})}$, where D is the distance to the source, B_{ν} is the Planck function for dust temperature T_{dust} , F_{ν} and κ_{ν} are the flux and the dust opacity at the frequency of the observation ν . We note that the optically thin regime can be not satisfied, in this case our estimates provide a lower limit on the dust mass measurement. Dust temperature of 30 K is assumed, dust opacity value is $0.00899 \text{ g cm}^{-2}$, and spectral emissivity slope β is set to 1. With uniform assumptions on dust properties we are not introducing additional discrepancy between the disks measured within different observing projects. The disk mass ($M_{disk} = M_{dust} + M_{gas}$) is obtained by assuming a gas-to-dust ratio of 100.

Figure 2 presents $\dot{M}_{acc} - M_{disk}$ over disk masses. The Class I systems are matching a trend seen for Class II disks in Lupus star-forming region [2]. We also compare our results with three evolutionary tracks provided by magneto-hydrodynamic (MHD) disk winds theoretical models which predict different slopes in the $\dot{M}_{acc} - M_{disk}$ diagram [10]. Figure 2 shows that the slope of the evolutionary track changes when MHD disk wind effect are introduced on the viscous model [11], from shallower slopes for disk wind with magnetic field strength decreasing with time, to become completely flat (constant accretion rate with decreasing mass) for constant magnetic field strength with disk evolution. The viscous model is obtained considering initial disk mass $M_0 = 1M_{\odot}$ and $t_{\nu} = 10^5 \text{ yrs}$ [11]. Hybrid of viscous and MHD disk wind evolution is done following Eqs. 60 and 61 in [10]. Our results suggest that purely MHD disk wind evolution of the accretion disk does not reproduce the evolution from Class I to Class II. However, we stress that we cannot properly test these models with our sample, since both the magnetic effects and the disk viscous timescale depend on the environmental effects, while our sample is composed by sources from many different regions.

Conclusions and future steps

We summarise two important conclusions of this work. First, we highlight that a bias is present in our sample. To analyse Class I YSOs we need an estimate of the veiling, which is possible only for low-veiled sources. Considering only low-veiled young stars, we are studying only the less accreting objects. Therefore, we can interpret these results as lower limits among Class I YSOs. Second, observations of single star-forming clouds and models that include earliest stages of disk formation are necessary to further constrain the disk wind model and properly compare different evolutionary stages of young stars.

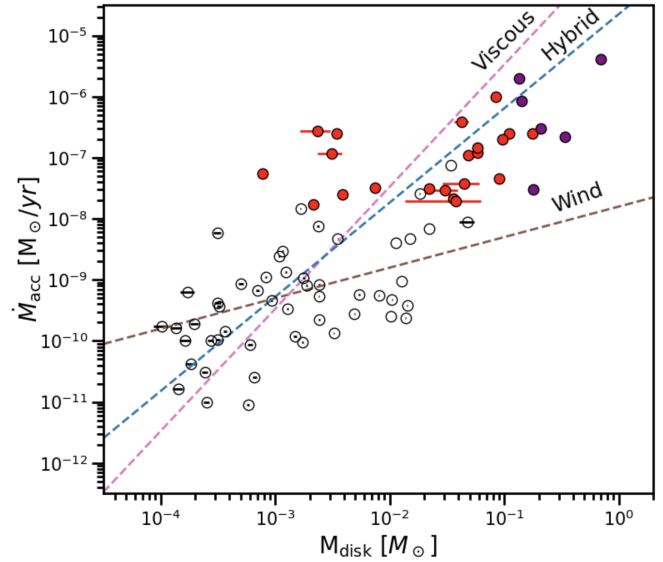


Figure 2: Mass accretion rate vs. disk dust mass. Red filled circles are the solution of our sample. Purple filled circles are other Class I, and orange filled circles are Class 0. Empty circles are Class II from Lupus sample. Dashed lines correspond to evolutionary tracks for three cases: pure viscous evolution (pink), hybrid of viscous and wind (light blue) and pure MHD disk wind (brown). Figure taken from Fiorellino et al. 2022, submitted.

References

- [1] Fiorellino, E., et al. 2021, MNRAS, 500, 4257
- [2] Manara, C., et al. 2022, 2022arXiv220309930M
- [3] Enoch, M., et al. 2009, ApJ, 692, 973
- [4] Hartmann, E., et al. 2021, ARA&A, 54, 135
- [5] Antonucci, S., et al. 2011, A&A, 534, 32
- [6] Fiorellino, E., et al. 2021, A&A, 650, 43
- [7] Connelley, M., & Greene, T., 2010, AJ, 140, 1214
- [8] Davies, C. L., 2021, SoftwareX, 14, 100687
- [9] Alcalà, J., et al. 2017, A&A, 600, 20
- [10] Tabone, B., et al. 2021, A&A, 650, 192
- [11] Lodato, G., et al. 2017, MNRAS, 472, 4700

Short CV



- 2014: Bc in Physics & Astrophysics, La Sapienza University, Rome, Italy
- 2017: MSc in Astrophysics & Astronomy, La Sapienza University, Rome, Italy
- 2017–2020: PhD in Astronomy, Astrophysics & Space Science, PhD program: La Sapienza and Tor Vergata Universities, and INAF Institute, Rome, Italy
- 2019–2020: ESO Studentship, Garching, Germany
- 2020–present: ERC Postdoctoral Fellowship, Konkoly Observatory, CSFK, Budapest, Hungary

Strength In Numbers: How Do Stellar Companions Affect Giant Planet Formation?

Clémence Fontanive

Center for Space Habitability, University of Bern, Switzerland

The origin of the most massive extra-solar giant planets and brown dwarfs, objects with intermediate properties between stars and planets, remains unclear, with several possible formation pathways considered. In particular, the population of brown dwarfs and giant planets orbiting around their host stars from very close orbital separations is still challenging to reconcile with theories of formation and evolution. Stellar binaries have long been neglected in exoplanet science, with many selection effects and biases against binaries present in observational surveys, and theoretical models of planet formation primarily focused on single stars. However, with over half of the stars in our Galaxy being part of binary or higher-order multiple systems [1], studying binaries as environments for exoplanets is essential to achieve a complete overview of the diversity and origins of exoplanetary systems.

The dominant finding emerging from studies of exoplanets in binary star systems is the idea that tight binary companions, with separations of tens of au, prevent the formation or survival of planets, observationally confirmed through a strong deficit of exoplanets in such binaries [2]. Nonetheless, slightly wider binaries, on separation scales of hundreds of au, may be less detrimental to the existence of planets, and could even help planet migration processes via secular interactions with the planets [3]. In addition, early surveys suggested that massive giant planets and brown dwarf companions on tight orbits may be predominantly found in wide binary systems, and that these inner planetary companions in multiple-star systems may show distinct physical and orbital properties to the rest of the exoplanet population [4].

Recently, we confirmed the robustness of these findings [5], measuring that $\sim 80\%$ of stars hosting a planet or brown dwarf above $7 M_{\text{Jup}}$ and within 1 au have an outer binary companion on the separation range 20–10,000 au. This indicates that stellar multiplicity likely plays a role in the existence and properties of these massive planetary and brown dwarf companions, although the precise nature and extend of this role is still not understood.

Compilation of planets in binaries

In order to place these results into a wider context, we gathered the largest compilation to date of planets in wide binary star systems, presented in [6]. From a sample of 938 stars hosting 1326 confirmed exoplanets and brown dwarfs within 200 pc, we identified from existing literature information and the Gaia catalogues 218 hosts to have visual stellar companions, confirmed to be co-moving with the primary star. The companion separations extend from <1 au for the most extreme case to 20,000 au, the outer limit placed on the companion search, with companion masses ranging from the hydro-

gen burning-limit to several Solar masses, resulting in a wide diversity of systems.

The obtained compilation provides a raw binary fraction of $23.2 \pm 1.6\%$ for planetary hosts, with a $2.2\text{-}\sigma$ difference between single-planet systems ($25.1 \pm 1.9\%$) and multi-planet systems ($18.0 \pm 2.7\%$). An even larger $3.6\text{-}\sigma$ difference was observed in multiplicity rate between stars harbouring giant planets or brown dwarfs, with masses above $0.1 M_{\text{Jup}}$ ($25.5 \pm 1.8\%$), and those hosting sub-Jovian planets ($16.6 \pm 1.7\%$), a trend that seems to be further emphasised as we look at higher-mass and shorter-separation planets and brown dwarfs.

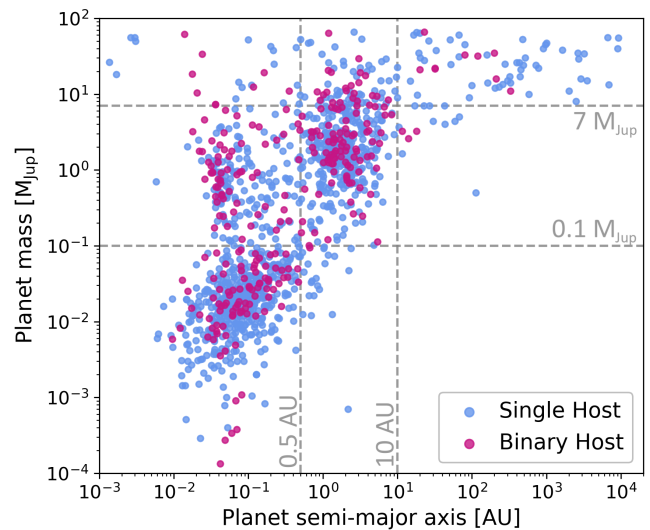


Figure 1: Semi-major axes against masses of all planets and brown dwarfs in the studied compilation, showing those around single stars in blue and those in binary star systems in magenta.

While underlying biases from the original planet discovery surveys and incompleteness effects in the binary search were not accounted or corrected for in this study, the gathered compilation may also be used to investigate if or how stellar multiplicity impacts planet properties across various regions of the planetary parameter space (Figure 1). Detailed analyses comparing the distributions of planetary semi-major axes and masses between those orbiting apparently single stars and those found in binary systems confirmed the excess of close-in, massive giant planets and brown dwarfs in binaries, compared to less massive planets, and to wider, warm and cool giants.

Effect of binary separation

To understand how the observed stellar companions may be affecting the formation or architectures of the inner planets and brown dwarfs, we investigated the binary separations of all the systems in our sample with an exo-

planet or brown dwarf within 0.5 au and above $0.1 M_{\text{Jup}}$. This analysis revealed that short-period giant planets identified in very wide binaries, with binary separations beyond 1000 au, show the same mass and semi-major axis distributions as close-in giant exoplanets orbiting single stars (Figure 2). This suggests that such distant stellar companions do not influence the final properties and orbital configurations of the inner planets.

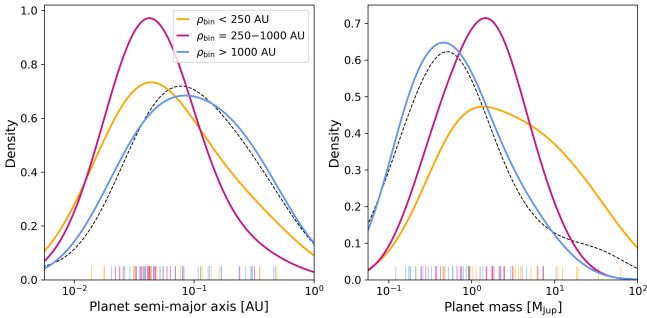


Figure 2: Planet semi-major axes (left) and masses (right) as a function of binary separation for all planets with masses above $0.1 M_{\text{Jup}}$ and semi-major axes within 0.5 au. The dashed black lines show the distributions for planets in the same mass and semi-major axis ranges found to be orbiting single stars.

On the other hand, we found that the excess of massive and close-in planets in binaries mostly appear to be in binary systems with separations of several hundreds au, and that planets and brown dwarfs in such binaries tend to show larger masses and/or shorter orbital separations than the planetary population around single stars or very wide binaries (Figure 2). These findings therefore indicate that outer stellar companions located at several hundred au are able to influence the formation or evolution of the observed giant planets and brown dwarfs, with the mechanisms at play seemingly resulting in the formed inner companions reaching higher masses and tighter orbital configurations than those forming around single stars.

Disk fragmentation triggered by binary companions

The trends found between stellar multiplicity and different exoplanet populations are observed for the most massive planets and brown dwarfs only. We thus investigated the possible effects of outer binary companions on giant planet formation through gravitational instability (GI) in circumstellar disks, since this process primarily produces massive planetary and substellar companions, in contrast to the core accretion mechanism. We therefore adapted simulations of self-gravitating disks [7] to binary environments, adding outer stellar companions around $0.2 M_{\odot}$ disks that were found to be stable and unable to fragment in standard single-star environments.

Testing various binary semi-major axes, we found that the added external stellar companions were successfully able to induce fragmentation in otherwise-stable disks, when on intermediate separations of \sim few hundred au, as shown in Figure 3 [8]. However, closer-in companions within \sim 100 au were found to be too disruptive, while wider binaries beyond several hundred au had no effect on the disk evolution, which remained stable as in the single-star case. Exploring a range of binary configurations (varying the binary eccentricity, inclination, companion mass), we found that this optimal range is a function of the various binary elements, resulting in a sweet spot of binary configurations over which outer companions are able to trigger GI fragmentation, and lead to the formation of giant planets or brown dwarfs. GI induced by intermediate-separation stellar companions may hence be able to explain the origin of the observed excess of massive giant planets and brown dwarfs in such binaries.

References

- [1] Raghavan, D., et al. 2010, ApJS, 190, 1
- [2] Kraus, A., et al. 2016, AJ, 152, 8
- [3] Naoz, S. & Fabrycky, D., 2014, ApJ, 793, 137
- [4] Zucker, S., & Mazeh, T., 2002, ApJ, 568, 113
- [5] Fontanive, C., et al. 2019, MNRAS, 485, 4967
- [6] Fontanive, C., & Bardalez Gagliuffi, D., 2021, FrASS, 8, 16
- [7] Forgan, D., & Rice, K., 2013, MNRAS, 432, 3168
- [8] Cadman, J., et al. 2022, MNRAS, 511, 457

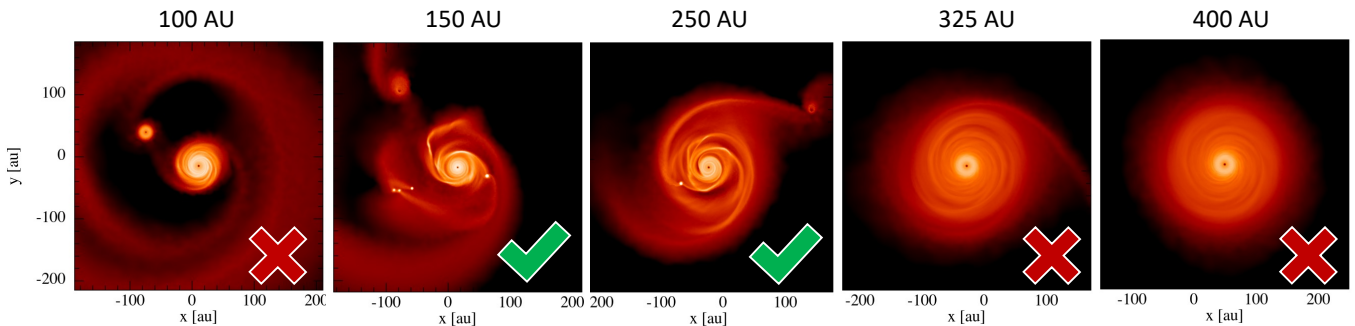


Figure 3: Simulations of self-gravitating disks with outer stellar companions on binary separations ranging from 100 au to 400 au. The added binary companions with separations of 150–250 au were able to successfully trigger the fragmentation of the disk.

Short CV



2011–2015: MSci in Physics, Imperial College London, UK
 2015–2019: PhD in Astronomy, University of Edinburgh, UK
 2019–present: CSH Fellow, University of Bern, Switzerland

The effect of the streaming instability on protoplanetary disc dust emission

Chiara Eleonora Scardoni

Institute of Astronomy, University of Cambridge, Madingley Road, Cambridge CB3 0HA, UK

According to the core accretion theory, rocky planets form in protoplanetary discs by growing the initial μ -sized dust grains up to the size of a planet. This growth process can be divided into three main stages: grain growth (from $\sim \mu\text{m}$ to $\sim \text{cm}$), planetesimal formation (from $\sim \text{cm}$ to $\sim \text{km}$) and protoplanet formation (from $\sim \text{km}$ to $\sim 10^3 - 10^4 \text{ km}$). The planetesimal formation stage is particularly problematic due to the so-called "radial drift barrier", which hinders the formation of km-sized objects. The aerodynamical interaction between the dust and the gas, in fact, causes the dust grains to lose angular momentum and drift inwards; the efficiency of this interaction is measured through the Stokes number τ_s , a dimensionless quantity related to the grain size and disc parameters: the closer is τ_s to 1, the stronger is the interaction, and thus the radial drift. For typical disc parameters, $\tau_s \sim 1$ corresponds to grain sizes of $\sim \text{cm}$, which are thus expected to rapidly drift inwards, becoming unavailable to form planetesimals.

A potential solution to this problem is the streaming instability, an hydrodynamical instability that promotes the formation of dust overdensity regions, which can help the planetesimal formation in a twofold way: on one hand, the overdense regions interact differently with the gas, determining a reduction in the radial drift velocity; on the other hand, they can become dense enough to promote rapid gravitational collapse and planetesimal formation. The efficiency of streaming instability depends on the local system's properties: the grain Stokes number τ_s , proportional to the grain size (favourable condition: $\tau_s \sim 1$); the pressure support Π (which influences the dust-gas interaction); and the local dust to gas mass ratio Z (which must be high enough to trigger the instability).

In this context, our goal is to check if observational data contain signatures of streaming instability by comparing the emission properties in the mm of simulated systems undergoing streaming instability to recent data in the Lupus star forming region [2, 3]. Since the dust clumps formed via streaming instability are too small to be directly observed, we probe them through observable quantities; in particular, we consider the optically thick fraction, defined as the ration between the system's flux and the flux that it would emit if it were a black body,

$$ff = \frac{F_{\nu,\text{system}}}{F_{\nu,\text{bb}}}; \quad (1)$$

and the spectral index

$$\alpha = \frac{\partial \log F_{\nu,\text{system}}}{\partial \log \nu}, \quad (2)$$

and compare the simulations' distribution to the data distribution in the $ff - \alpha$ plane, studied by [2, 3].

Dust clump formation

We perform 12, 2D, local simulations of systems including 28 particle species (characterised by different Stokes numbers) with the hybrid hydrodynamical code ATHENA. Following previous studies of the parameter space [e.g. 4], we choose combinations of parameters (Stokes numbers, dust to gas mass ratio and particle mass distribution) that are expected to trigger streaming instability. After evolving each simulation until the formed clumps have reached a steady state, we compute the dust density profile for each particle species before (see the left panel in Figure 1) and after (right panel) particle clumping, noticing that the biggest particles in the simulations – i.e. those with τ_s close to 1 – participate in clumps (e.g., the magenta and blue lines in the Figure), whereas the smaller ones tend to remain uniformly distributed in the background (e.g., orange, yellow and green lines).

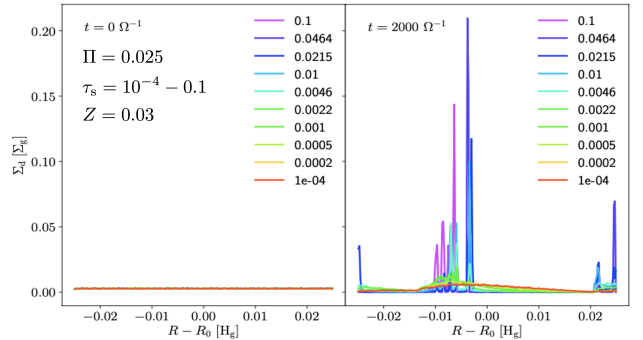


Figure 1: Particle density distribution before (left panel) and after (right panel) clump formation. The different colours refer to different Stokes numbers (see the plot legend). Plot from [1].

Dust clump emission

Once obtained the particle distribution, we use a canonical disc model to convert the dimensionless simulations to physical systems; by varying the gas density we obtain for each simulation 10 different physical systems characterised by different grain sizes; this is particularly useful as the mm opacity varies significantly with the grain size. We compute the grain opacity for the obtained grain sets (using the code by Birnstiel [5]) and apply a radiative transfer model to find the emitted flux, from which we then obtain ff (Eq. 1) and α (Eq. 2).

Figure 2 shows the distribution in the $ff - \alpha$ plane for one of our simulations. The blue squares represent the initial distribution of the 10 systems obtained from the conversion of the dimensionless simulation to physical units; the magenta diamonds show the systems' distribution after particle clumping; the black arrows link together the initial and final condition for the same system.

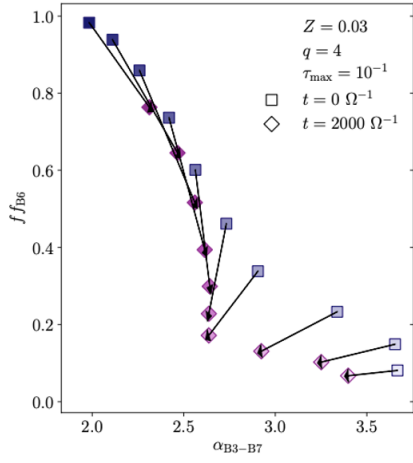


Figure 2: Distribution in the $ff - \alpha$ plane from [1]. The blue squares and the magenta diamonds show the distribution before and particle clumping, respectively. The black arrows link the initial condition of each system to its final condition.

Since the clumps are overdense, they are optically thicker than the initial particles' uniform distribution; as a consequence, when a particle goes in the clump, its emission is partially hidden. This explains why in all the systems we notice a decline in the optically thick fraction: some of the emission from grains in the uniform initial conditions is now hidden in optically thicker areas, causing a reduction of the overall flux declines and thus of the optically thick fraction. The spectral index, instead, can either increase or decrease, depending on the opacity index β (describing the opacity variation with the frequency) of clumping (big) particles. Recalling the relation between the spectral index and the opacity index (being B_ν the Planck function)

$$\alpha \sim \frac{\partial \log B_\nu}{\partial \log \nu} + \beta, \quad (3)$$

we notice that an increase (reduction) in β will produce an increase (reduction) in α . Since the contribution given by the smallest particles is always the same, because they remain in the uniform background, we deduce that the increase/decrease in α must be related to the value of β of the big (clumping) particles, whose emission is down-weighted after clump formation: if β of clumping particles is high (low) then α decreases (increases).

Results

We finally compare the simulations' and data distribution in the $ff - \alpha$ plane through the plot in Figure 3. The left panels refer to the group of simulations characterised by maximum Stokes number $\tau_{\max} = 0.1$, the right pan-

els refer to simulations with $\tau_{\max} = 1$; the upper panels show the distributions before particle clumping, the lower panels show the distribution after particle clumping. The different colours in the plot refers to different simulations (see the corresponding parameters in the plot legend), while the green stars show the data distribution. By comparing the upper and lower panels, we notice that the clump formation via streaming instability drives the simulations to the area of the plot occupied by the data.

Since the simulations refer to a local portion of the disc, whereas the data are based on measurements of flux emitted by the whole disc, we also define an integrated disc model (by mapping our simulations' results to different radii of the disc). We find that, provided that streaming instability takes place in a region of the disc which dominate the flux, also in the integrated disc model the action of streaming instability drives the simulations to the area of the $ff - \alpha$ plane occupied by the data.

We therefore conclude that the formation of dust clumps via streaming instability is consistent with the observations in the Lupus star forming region.

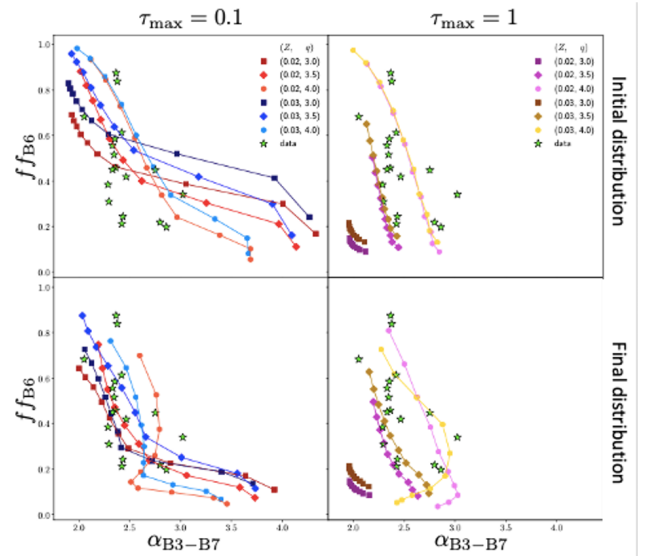


Figure 3: Distribution in the $ff - \alpha$ plane for all the simulations (see parameters in the legend) before (upper panels) and after (lower panels) clump formation. The data distribution is shown through the green stars. Plot from [1].

References

- [1] Scardoni, C., & al, 2021, MNRAS, 504,1495-1510
- [2] Tazzari, M., et al. 2021, MNRAS, 506, 5117-5128
- [3] Tazzari, M., et al. 2021, MNRAS, 506, 2804-2823
- [4] Bai, X-N., & Stone, J., 2010, APJ, 722, L220-L223
- [5] Birnstiel, T., & al, 2018, APJ, 869, L45

Short CV



2017: Bachelor's Degree in Physics, Università degli Studi di Milano
 2019: Master's Degree in Physics, Università degli Studi di Milano
 2019–present: Ph.D. student at the Institute of Astronomy, University of Cambridge

Can a massive star possess its own planetary system?

Vito Squicciarini

Department of Physics and Astronomy 'Galileo Galilei', University of Padova, Vicolo dell'Osservatorio 3, 35122, Padova, Italy

INAF - Osservatorio Astronomico di Padova, Vicolo dell'Osservatorio 5, 35122, Padova, Italy

Having recently reached the impressive milestone of 5000 confirmed exoplanets, the exoplanetary field has attained in less than 30 years a remarkable degree of maturity. Not only is a purely discovery phase giving way to a more thorough characterization phase, but also the quest for statistical trends connecting the observed properties of the exoplanet population has rapidly become a major scientific goal. Unveiling the physical processes lurking behind the multifaceted hues of observed planetary architectures –and the limits outside which these processes no longer work– is indeed the ultimate purpose of *exoplanet demographics*.

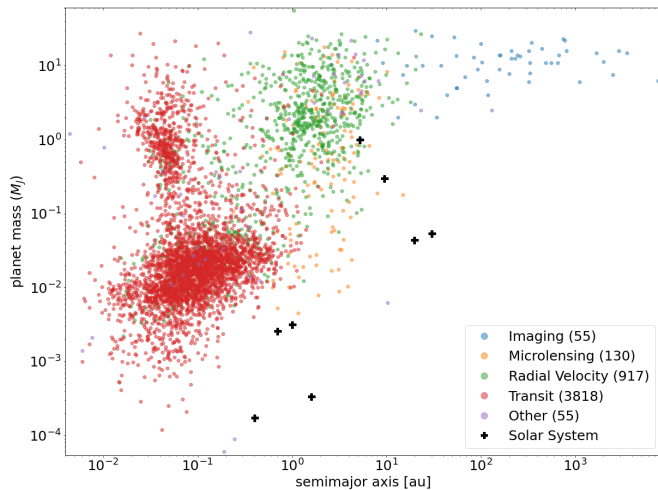


Figure 1: Mass vs semimajor axis of confirmed exoplanets. Only exoplanets whose stellar host mass is known to a precision of at least 30% are shown. Each planet is labeled according to its detection method: transits in red, radial velocity in green, microlensing in orange and direct imaging in blue. Source: NASA Exoplanet Archive.

Is the exoplanet census unbiased?

The foundations of exoplanet demographics lie in a powerful, yet simple idea: namely, that the distribution of exoplanets as a function of their physical, orbital and stellar-host properties has been thoroughly crafted by physical processes related to their formation and subsequent evolution. However, these trends are mostly concealed by detection biases intrinsic to the detection techniques employed. In other words, each method has its strengths and weaknesses, and is suited to probing only a specific portion of the parameter space (Figure 1).

As a consequence of the bias of transits and radial velocities (RV) for closed-in planets, about 90% of the confirmed exoplanets lie closer to their stars than the Earth is to the Sun. Moreover, 99.3% of the confirmed

exoplanets orbit around stars with $M_* < 2M_\odot$; given that about 96% of the stars have $M_* < 2M_\odot$, *high-mass* stars ($M_* > 2M_\odot$) are underrepresented by a factor of six. Is it just a sensitivity problem, or is there any physical obstacle that makes it difficult –and eventually impossible– to form a planet around a star of increasing mass?

The impact of stellar mass

The occurrence of giant planets (which are the easiest to detect) as a function of the stellar host mass has been the focus of several radial velocities campaigns. A robust positive correlation between giant planet occurrence and stellar mass exists [1]; however, after reaching a peak at $M_* \approx 1.7M_\odot$, a turnoff is observed in this occurrence, eventually dropping to 0% at $M_* \gtrsim 3M_\odot$. A peak in the semimajor axis distribution at a few au and a significant positive correlation with stellar metallicity are also observed.

These trends are in line with the predictions of core accretion (CA), the mechanism thought to be responsible of giant planet formation in our solar system [2]. The increased reservoir of disk mass –scaling with stellar mass– is naturally reflected into a greater frequency of gas giants, and the increasingly rapid dispersal of the protoplanetary disk around heavier stars eventually leaves not enough time for giant planet formation at $M_* \gtrsim 3M_\odot$.

However, the sensitivity of RV gradually degrades with orbital distance, and it can be shown that for $M_* \gtrsim 2.5M_\odot$ the technique gets essentially blind to the region where giant planet formation should preferentially take place [3]. This is extremely important, as RV is even blinder to the wide-orbit exoplanet population possibly produced by a different mechanism, gravitational instability (GI) [4]. Unlike CA, GI preferentially creates a flat mass distribution of Super Jupiters and brown dwarfs at wide separations from their stars. Extending the demographics of giant planets to this regime would help clarifying the relative weight of the two contributions; direct imaging, a technique that is preferentially sensitive to young giant planets in wide orbits, is particularly suited to this scope.

The BEAST survey

The direct-imaging B-star Exoplanet Abundance Study (BEAST) is the first planet-hunting survey dedicated to B stars ($M_* > 2.4M_\odot$) [5]. BEAST exploits the high-contrast imaging capabilities of SPHERE@VLT, and in particular those of the Integral Field Spectrograph (IFS) and the dual-band imager (IRDIS), providing images in a $1.7'' \times 1.7''$ and $11 \times 11''$ field of view, respectively.

The stellar sample of BEAST is constituted by 85 members of the Scorpius-Centaurus association, the nearest ($\sim 100 - 200$ pc) star-forming region to the Sun. Binary stars have been retained –with the exception of those in the separation range $0.1 - 6''$, negatively affecting the performance of SPHERE–, offering thus the additional opportunity to investigate the effect of stellar multiplicity. The combination of short distance and young ($\sim 5 - 20$ Myr) age makes this sample particularly suited for direct imaging, enabling the detection of companions as small as $5M_J$.

While the survey is still in progress ($\sim 30\%$ in April 2022), its provisional results are already intriguing. b Cen is a tight binary system, with a total mass of $6 - 10M_\odot$, possessing a $10.9 \pm 1.6M_J$ giant planet at a very wide (~ 550 au) separation [6]. With two observations at hand, plus a serendipitous archival epoch from 2000, we were able to assess the common proper motion to b Cen with $> 7\sigma$ significance.

This object acquires its greatest significance when coupled to a second, even more intriguing detection. μ^2 Sco [7] is, from a stellar evolution standpoint, a massive star ($M = 9.1 \pm 0.3M_\odot$): a star massive enough to end its life as a supernova. A comoving substellar companion, μ^2 Sco b, was found at 290 au (Figure 2). With a mass $M = 14.4 \pm 0.8M_J$, it is slightly above the deuterium-burning limit, which classically marks the transition between planets and brown dwarfs. En passant we mention that, lurking beneath the glaring light of the star, a second candidate was tentatively spotted at an extremely small separation ($0.12'' \approx 20$ au). If confirmed, its luminosity would correspond to that of an object with $M = 18.5 \pm 1.5M_J$.

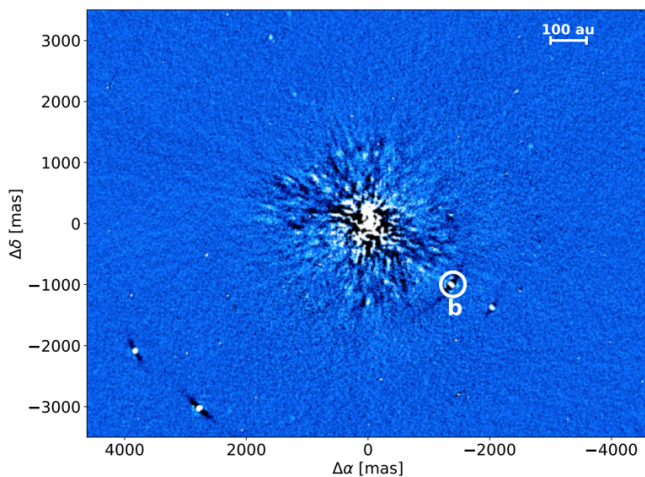


Figure 2: An image of μ^2 Sco. The star, artificially obscured by the coronagraph, is at the center of the image. Several background sources can be seen as bright point sources. μ^2 Sco b is the source inside the white circle.

Discussion

The nature of these unusual objects is uncertain, and challenges our current view of planet formation. A mass criterion would place b Cen b in the planetary regime and μ^2 Sco b in the brown dwarf regime, but their similar properties strongly argue for classifying them within a unified frame. With respect to their mass ratio q , i.e. the ratio between companion and stellar mass, their $q = 0.001 - 0.002$ are intriguingly similar to that of Jupiter.

Such a q is typical of a core accretion scenario, and an extrapolation of known frequencies of giant planets to the B-star regime is indeed favoured over an extrapolation to low q of the stellar companion distribution [7]. However, the expected timescale of core buildup is of the order of a few million years, much higher than the timescale of disk dissipation ($\sim 10^5$ yr), hence posing an insuperable obstacle to this scenario.

On the other hand, formation timescales are not a problem for the extremely rapid ($10^3 - 10^4$ yr) GI; the large observed orbital separations are naturally consistent with this scenario. However, the mass distribution of GI objects is rather flat, with more than 90% of the objects having masses above the deuterium-burning limit already around $1M_\odot$ stars [8]. Thus, the conversion efficiency of disk mass into companion mass would here be atypically low.

The BEAST survey has already shown that a massive star can possess its own planetary –or at least planet-like– system, challenging our prior views of giant planet formation under such exotic conditions. In the next few years, we will know how frequent these systems are, and thorough follow-up efforts will hopefully shed light on their elusive origin.

References

- [1] Wolthoff, V., et al. 2022, arXiv e-prints, arXiv:2202.12800
- [2] Pollack, J. B., et al. 1996, *Icarus*, 124, 62
- [3] Gaudi, B. S., 2022, in *Astrophysics and Space Science Library*, Vol. 466, 237–291
- [4] Boss, A. P., 2003, *ApJ*, 599, 577
- [5] Janson, M., et al. 2021, *A&A*, 646, A164
- [6] Janson, M., et al. 2021, *Nature*, 600, 231
- [7] Squicciarini, V., et al. 2022, accepted by *A&A*
- [8] Forgan, D. H., et al. 2018, *MNRAS*, 474, 5036

Short CV



2013–2017: BSc in Physics, University of Padova, Italy
 2017–2019: MSc in Astronomy, University of Padova, Italy
 2019–present: PhD in Astronomy, University of Padova / INAF, Italy

Young Stars in the Galactic Center

Sebastiano D. von Fellenberg

Max-Planck-Institute for Radio Astronomy, auf dem Hügel 69, D-53121 Bonn, Germany

Observations

We compile spectroscopic GC observations spanning almost two decades^{||}. Our observations consist of AO-assisted SINFONI observations, which we re-reduce and analyse. A considerable fraction of these data were analysed in previous publications, e.g. [2, 3, 4, 5, 6] and we

analyse previously unpublished observations of the GC. We try to classify all stars photometrically discernible in the exposures into either young or old type by extracting spectra and identifying the emission and absorption lines. We classified over 2800 stars into un-classifiable, old, candidate young or young star.

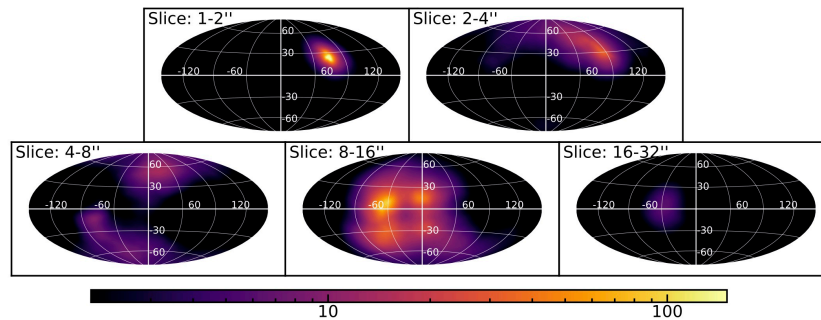


Figure 1: Significance (σ_{pixel}) of the overdensity of the angular momentum distribution in logarithmic scale as function of projected radius slice, computed using the isotropic cluster prior.

Angular momentum in the Galactic Center

The initial conditions of a test particle in a fixed gravitational potential have six degrees of freedom, corresponding to the initial position and velocity of the particle which can be expressed in terms of the classical orbital elements: the semi-major axis a , the eccentricity e , the inclination i , the longitude of the pericenter ω , the position angle of the ascending node Ω , and the epoch of pericenter passage t_p . In order to determine these six numbers, one needs to measure six dynamical quantities. From multi-epoch astrometry in the GC, one can determine the on-sky position $(x; y)$ and proper motion $(v_x; v_y)$ of the object. Thus, one needs two more dynamical quantities in order to determine an orbit. From spectroscopy one can get the radial velocity of a star (v_z). The missing z -coordinate is not accessible directly at the GC distance of ~ 8.28 kpc [10]. If only five dynamical quantities are known, in almost all cases one lacks an acceleration measurement, i.e. information on z . Yet, some constraints on the orbital parameters can be constructed. For example the angular momentum vector direction can be limited to lie within a one-dimensional half large circle across the sphere of possible orientations [2, 9]. The key finding of earlier works was that one can find a specific direction of the orbital angular momentum vector, which is compatible with a large number of the 5D-constrained young stars in the GC, indicating a ration in a common disk. This interpretation was independently confirmed by stars for which full orbits have been determined [7, 8]. The probability distribution of the orbital angular momentum vector

for a given star depends on the assumptions one makes on the missing information, i.e. the z -coordinate. Hence the exact dynamical structure (and thus the significance of certain features such as disks and warps) of the young star sample depends on the choice of the z -prior.

Constraining the z -values and significance of observations Several priors have been used in the past, for instance the uniform acceleration prior [8], or the stellar cusp prior [3]. All of these prior have in common that they produce biased distributions when compared against a relaxed isotropic cluster. In this work we propose a new method, which tries to explicitly reproduce an isotropic cluster and removes this systematic bias from the observation. The general idea is to use the known probability distributions of orbital elements of an isotropic cluster and to convert them to probability distributions in phase space in which the observations take place. We refer the reader to the original publication for the rigorous motivation, derivation and extensive numerical tests of the method.

Distribution of the Young Stars in the Galactic Center

Figure 1 shows the overdensity of angular momentum for six projected radius slices. We bin our young star samples in six bins with increasing projected distance from the black hole.

The inner region Our updated star sample confirms the presence of a warped clockwise disk for stars in a region ranging from $1''$ to $4''$ (middle and right plot of top panel in Figure 1). In this inner most region, most stars

^{||}This text is based on [1], its text and figures are reproduced with permission of ApJL

are aligned coherently. We call this the inner part of the clockwise disk, abbreviated CW1. For the radial bin ranging from $2''$ to $4''$, CW1 is less dominant and starts to change smoothly to the outer part of the clockwise disk (CW2). The member stars of CW1 and disk are plotted in Figure 2.

The intermediate region For the radial bin ranging from $4''$ to $8''$ (bottom left panel in Figure 1), no single disk structure dominates the density map. [3] found an overdensity for their sample of 30 stars in the range $3''.5$ to $7''$. They interpret this as a warped extension of the clockwise disk, here called CW2. We confirm the CW2 disk (p-value $\sim 99.2\%$, Figure 5).

The outer region For projected distances larger than $8''$ we find three prominent features (bottom middle panel in Figure 1). First, we confirm an overdensity of angular momentum, called the outer filament 2 (F2). Second, we find the outer continuation of the CCW/F1 feature. Most prominently, we find a previously un-reported feature at very high significance, called the second outer filament F3.

We find five significant different kinematic features compared to an isotropic cluster. Further, we have found that the vast majority (75%) of stars can be attributed to one of these five features. The angular momentum distribution in the GC is therefore very rich, and significantly different from the old star population. We demonstrate that the young stars reside in a warped-disk and several outer filaments. Such a rich structure has been proposed by several simulations of in-situ star formation in an in-falling gas cloud scenario. [12] demonstrated that stars can form in massive gas clouds around a massive black hole like Sgr A* and speculated that multiple young star rings may be present in the GC. [13] have demonstrated that in the presence of two separate disk systems (like the clockwise and the counter-clockwise system), the disks tidally interact with one another causing a warping of the disks. Further, [14] show a warping of the disk naturally arises from the interaction of the disk with the potential of the embedding old star cluster.

Conclusions

The set of simulations by [15] in which two giant molecular clouds collide and subsequently accrete show intriguingly comparable features to the ones observed: A small, medium eccentric disk in close proximity of Sgr A*; several remnant star streamers at larger separation which have substantially different angular momenta directions; and higher eccentricities at larger separations. Further, the simulations show differences in the distribution of O and WR type stars, with the most heavy stars found in the inner disk – consistent with the apparent distribution

of O and WR type stars in the Galactic Center. We thus argue that the simultaneous formation of all young stars in the Galactic Center remains a feasible scenario, consistent with the latest analysis of the age distribution of the S-star cluster [16]. However, the dramatically different kinematic distribution of the B-stars in the central arc-second remains serious challenge [7] for such a common formation scenario, and more detailed analysis of the age distribution of the young stars are required to confirm or rule out a single star formation event some ~ 6 Myr ago.

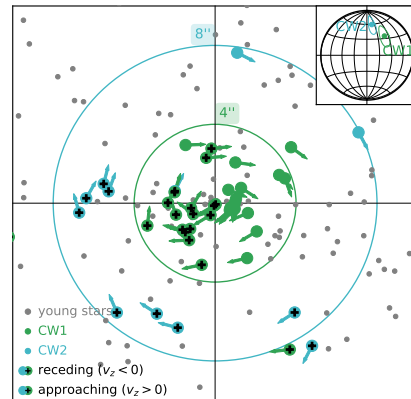


Figure 2: Comparison of stars belonging to the CW1 (green) and CW2 (blue) disk. Stars that do not belong to either feature are plotted in gray. The inset shows the prior width and direction of the feature prior L_{feat} based on which the colored stars are selected. Stars marked with a “plus” have positive radial velocity, unmarked stars have a negative radial velocity. The arrows indicate the direction of the projected velocity. In both cases we evaluate the disk membership probability for all young stars, i.e. no radial binning has been applied.

References

- [1] von Fellenberg, S. D., 2022, ApJL, 932, L6
- [2] Paumard, T., 2006, ApJ, 643, 1011
- [3] Bartko, H., 2009, ApJ, 297, 1741
- [4] Bartko, H., 2010, ApJ, 708, 834
- [5] Pfuhl, O., 2011, ApJ, 741, 108
- [6] Pfuhl, O., 2014, ApJ, 782, 101
- [7] Gillessen, S., 2017, ApJ, 837, 30
- [8] Yelda, S., 2014, ApJ, 783, 131
- [9] Lu, J., 2009, ApJ, 764, 155
- [10] Gravity Collaboration, 2022, A&A, 657, L12
- [11] Genzel, R., 2003, ApJ, 594, 812
- [12] Bonnel, I.A., 2008, Science, 321, 1060
- [13] Löffelmann, U., 2009, MNRAS, 394, 1841
- [14] Kocsis, B., 2011, MNRAS, 412, 187
- [15] Hobbs, A., 2009, MNRAS, 394, 191
- [16] Habibi, M., 2017, ApJ, 847, 120

Short CV



- 2017: Master in Physics, Technical University of Munich, Munich, Germany
- 2017–2021: PhD in Astronomy, Max Planck Institute for Extraterrestrial Physics, Garching, Germany
- 2022–present: Postdoc, Max Planck Institute for Radio Astronomy, Bonn, Germany



Reach New Heights

Fellowships in Germany or Chile

Develop your scientific profile
Become an independent researcher
Prepare for future responsibilities



eso.org/fellowship

STELLAR POPULATIONS AND EVOLUTION, AND TECHNOLOGY

First light of the FIRST visible fibered interferometer upgrade at the Subaru telescope

Kevin Barjot

LESIA, Observatoire de Paris, Université PSL, CNRS, Sorbonne Université, Université de Paris, 5 place Jules Janssen, 92195 Meudon, France

Since the mid-nineties, five thousands exoplanets have been discovered, mainly by space missions using indirect detection methods. The existing ground-based 8-m class telescopes and the forthcoming 30-m class telescope offer high angular resolution imaging of planetary system. On the one hand the advantage of such a direct detection is obtaining a spectrum of the planet which permits the study of its atmosphere if it exists and seek for a possible presence of life. On the other hand the caveat is that the atmosphere of the Earth corrugates the light coming from the target thus an (Extreme) Adaptive Optic (ExAO) system is mandatory to correct for these perturbations and perform direct imaging at the diffraction limit regime of the telescope. The pupil masking technique [1] consists in placing a non-redundant mask on the telescope pupil such that each spatial frequency in the image is sampled by a unique pair of sub-pupils. The angular resolution limit is divided by two and the effects of atmospheric perturbations on the fringes are limited. The caveat of this technique is that only a fraction of the flux of the telescope is utilized. It can be coped using the pupil remapping technique [2] which rearrange non-redundantly the sub-pupils using optical fibers and allows to use the flux of the entire pupil. These fibers are single-mode and filter the speckles remaining across each sub-aperture.

The Fibered Imager foR a Single Telescope

The upgraded version of the FIRST instrument [3] is currently installed on the Subaru Coronagraphic Extreme Adaptive Optic (SCEAO) platform [4, 5], a second-stage ExAO system providing light corrected from the atmospheric turbulence. As illustrated on the scheme of the two versions of FIRST on the figure 1 the telescope pupil is sampled thanks to an array of 250 μm pitched microlenses (2) that focus light into single-mode optical fibers (4). This injection is optimized via a segmented mirror (1) paved with 37 hexagonal segments of about 600 μm of circumscribed diameter that can be controlled in piston, tip and tilt. Afterwards, optical delay lines (ODL) (3) were added during the upgrade of the first version to correct for optical fiber length mismatch in order to equalize the optical path differences (OPD) between the incoming beams. The integrated optic (IO) chip (5) combines the light of the sub-pupils pair-wisely as opposed to the first version where the optical fibers were mounted non-redundantly on a V-Groove to make the light beams interfere at the focus of a lens. The chip was tested in laboratory [6, 7] prior to its integration in the instrument in 2021. Finally, the chip outputs are imaged on the camera (7) and spectrally dispersed by a grism spectrometer (with a spectral resolution of 4000 @700nm) (6). Polarizations are split by a Wollaston prism in order to avoid

contrast loss due to the birefringence of the polarization maintaining fibers and of the chip. FIRSTv2 would ultimately utilize all the sub-pupils to maximize the overall throughput and the spatial frequency coverage of the instrument.

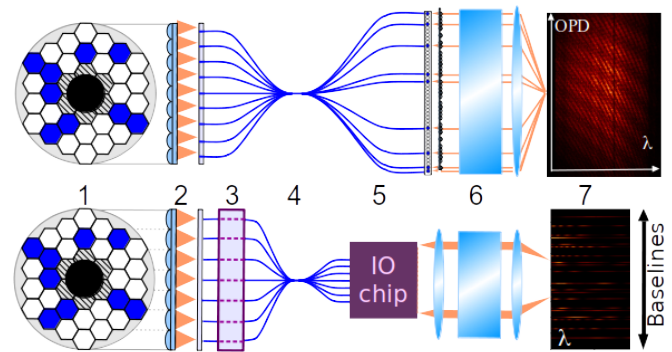


Figure 1: Schematic of the pupil remapping technique implemented in the FIRST instrument. Top: original version. Bottom: version 2 with the IO chip.

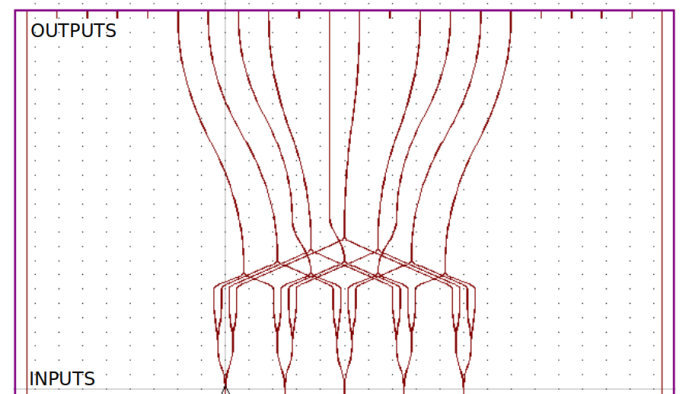


Figure 2: Photonic chip schematic. The five inputs are interferometrically recombined by pairs. Each of the 10 outputs corresponds to one pair.

Data acquisition and processing

The key part of the FIRSTv2 instrument is the photonic chip which consists in a block of glass with engraved optical waveguides. As depicted in the schematic of the figure 2 it has five inputs (bottom) that are split in four guides to be recombined thanks to Y-junction couplers giving ten outputs (top). With such a device each of the spatial frequencies that corresponds to each pair is imaged on a few pixels on the camera as a fringe pattern spectrally dispersed. Hence, one frame encodes the interferometric flux for a specific OPD on several spectral channels.

In order to obtain the full interferogram the sub-apertures need to be modulated to sample the fringes as a function of the OPD.

Data analysis aims at reconstructing the interferogram from a series of images. A Pixel-To-Visibility Matrix (P2VM) [8] is calculated prior to observations and is used to fit the fringes and to retrieve the complex coherence terms for each baseline and each spectral channel:

$$\mu_{nn'} = |V_{nn'}| e^{i\psi_{nn'}} A_n A_{n'} e^{i\Delta\Phi_{nn'}} \quad (1)$$

With $|V_{nn'}|$ and $\psi_{nn'}$ the object's complex visibility modulus and phase, A_n the flux of sub-pupil n and $\Delta\Phi_{nn'}$ the differential piston (due to different fiber lengths, Adaptive Optics (AO) residuals and instrumental aberrations).

The phase of this term has two contributions in the context of a binary system observation: the continuum on the whole range of wavelength and the companion on a narrow band range. To obtain the companion contribution $\psi_{compnn'}$ the spectral differential phase is computed subtracting the phase of the continuum $\psi_{contnn'}$ (avoiding the spectral band of the companion) to the phase on the whole spectrum $\psi_{nn'}$, following:

$$\begin{aligned} \varphi_{diffnn'}(\sigma) &= \psi_{nn'} + \Delta\Phi_{nn'} - (\psi_{contnn'} + \Delta\Phi_{nn'}) \quad (2) \\ &= \psi_{compnn'} \quad (3) \end{aligned}$$

Moreover, this variable has the advantage of being self-calibrated by canceling out the differential piston part of the complex coherence terms.

Lab and on-sky results

In the lab two sources were injected on the FIRST testbed to simulate a binary source which spectrum is presented on the bottom left of the figure 3. The wide band continuum and the peak respectively simulate the central star and a companion with a narrow band emission with a contrast of 1.96 (the companion is 1.96 times brighter than the central star).

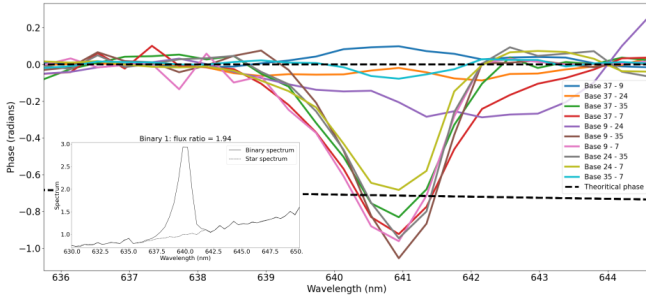


Figure 3: Differential phase measured on the FIRST test bench for a simulated binary system.

The figure 3 is the spectral differential phase of each baseline averaged over 4000 frames of 300 ms integration time. The black dashed lines indicate the theoretical phase amplitude expected for such a source. Four of them (37 – 9, 37 – 24, 9 – 24 and 35 – 7) show a value of zero because their baseline is orthogonal to the orientation of the binary system. The peak appearing around 641nm for all other baselines show that the companion is detected.

The figure 4 shows the first light of the upgraded FIRST instrument on Spica at the Subaru telescope, in 2021. It shows the fringes of the ten outputs of the photonic chip spectrally dispersed on the vertical axis, for an exposure time of 80ms and a gain factor of 300.

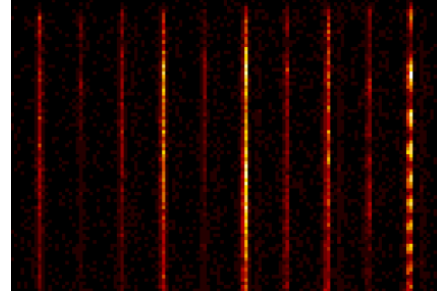


Figure 4: Image of fringes during observations of Spica. Each vertical line corresponds to one baseline. The vertical axis is the direction of the spectral dispersion (from 750nm to 800nm).

Conclusion

FIRST is an instrument for high angular and high contrast imaging of binary systems which was upgraded with an integrated optics chip to improve its performances in terms of stability and sensitivity. In 2021 we obtained the first light of the upgraded instrument on the SCEXAO platform at the Subaru Telescope. Data processing is still in progress.

References

- [1] Tuthill, P. G., et al. 2000, The Publications of the Astronomical Society of the Pacific, Volume 112, Issue 770
- [2] Perrin, G., et al. 2006, Monthly Notices of the Royal Astronomical Society, 373, 747
- [3] Huby, E., et al. 2013, Astronomy & Astrophysics, Volume 560, id.A113
- [4] Jovanovic, N., et al. 2015, Publications of the Astronomical Society of the Pacific, 127, 890
- [5] Vievard, S., et al. 2022, in preparation
- [6] Barjot, K., et al. 2020, Proc. of the SPIE, Volume 11446
- [7] Martin, G., et al. 2020, Proc. of the SPIE, Volume 11446
- [8] Millour, F., et al. 2004, Proc. of the SPIE, Volume 5491

Short CV



2017: BSc in Physics, Paris Cité University, France
 2019: MSc in Physics and astronomy, Paris Cité University, France
 2019–present: PhD in astronomy, Paris Observatory, France

The impact of realistic red supergiant mass-loss on stellar evolution

Emma R. Beasor

NSF's NOIRLab 950 N. Cherry Ave., Tucson, AZ 85719, USA

Mass-loss in stellar models

Directly linking massive stars to their explosive endpoints is a fundamental aim in stellar astronomy. Stars with initial masses (M_{ini}) between $8 - 30M_{\odot}$ are expected to evolve to become red supergiants (RSGs) before exploding as hydrogen-rich Type II-P supernovae (SNe). However, the apparent lack of Type II SN progenitors with initial masses above $\sim 17M_{\odot}$ [1] has led many studies to speculate on possible alternative fates for the more massive objects, including whether or not these stars undergo strong enough mass-loss that they peel away their own hydrogen envelope, causing them to die as stripped-stars and produce hydrogen-poor (or Type Ibc) SNe.

Stellar evolutionary models have demonstrated that mass-loss during the cool supergiant (CSG) phase ($T_{\text{eff}} < 10,000\text{K}$) can have a major effect on where on the Hertzsprung-Russel diagram (HRD) a star will end its life [2]. If a star has a strong enough wind it can self-strip its H-envelope and return to the blue side of the HRD, no longer producing a Type II SNe upon death. Instead, it will produce a stripped Type I SNe (e.g. Type Ib/c). This has been touted as a potential explanation

It is important to note that unlike hot star mass-loss, mass-loss rates (\dot{M}) during the CSGs, and in particular RSGs, phases are poorly understood and currently cannot be reliably determined from first principles. Instead, stellar models rely on purely empirical \dot{M} - L_{bol} relationships. The most widely used of these prescriptions is that of de Jager et al. (1988, hereafter dJ88 [3]), a literature review in which the authors collated all available \dot{M} measurements in the literature for stars of spectral types O through M, though it is no longer used for hot stars. The prescription itself contains only a handful of RSGs (15), and has a high level of internal scatter (around a factor of 10, see e.g. [4]), likely due to the lack of constraints on initial mass and metallicity [5]. This high level of uncertainty could be the difference between a star losing all of its H-envelope, or none of it at all.

To better understand the pre-SN evolution of massive stars we re-appraised the mass-loss rates of RSGs in 4 young local group clusters of different ages (hence containing RSGs of different initial masses) using modern data sets. By doing this, we were able to observe how \dot{M} changes as a star evolves up the RSG branch, as well as how the \dot{M} - L_{bol} relation changes as a function of initial mass. From this, we were able to derive an initial-mass dependent mass-loss rate prescription (hereafter B20) for use in stellar models [6]. An initial back of the envelope comparison demonstrated that compared to the \dot{M} implementation in the Geneva evolutionary models,

Input in evolutionary models

Using our new prescription we performed a comparative

study to the MESA-MIST stellar isochrones [7] which use the dJ88 prescription during the RSG phase. To directly compare the effects of using our updated prescription derived with cluster RSGs, we simply changed only the mass-loss rate implementation during these phases, swapping the dJ88 prescription for B20, while leaving all other parameters unchanged, and computed a new grid of stellar models with initial masses between $12 - 27M_{\odot}$.

While the final position on the Hertzsprung-Russel diagram did not change for these stars, there was a significant difference in the amount of H-envelope retained at core-collapse. In Figure 1 we show the H-rich envelope mass at CC as a function of the initial mass of the star, for both the standard MIST models and for the new models incorporating the B20 prescription. For the models using the dJ88 prescription the final H-envelope mass appears to plateau at $\sim 8M_{\odot}$, whereas for the models including the B20 prescription we see a positive correlation between H-rich envelope mass and initial mass. This means that in progenitor models, the majority of which use the dJ88 prescription, the parameter of H-envelope mass has effectively been held as a constant.

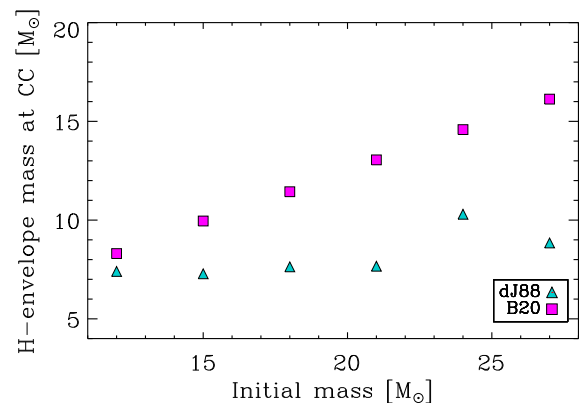


Figure 1: H-envelope mass at core-collapse as a function of initial mass, where the blue triangles represent models using standard dJ88 \dot{M} and the pink squares represent models using the B20 prescription.

Could an extreme mass-loss phase affect evolution?

Quiescent mass-loss throughout the RSG phase has been shown to be significantly lower than previous prescriptions have suggested. Implementing a new prescription in evolutionary models has shown that quiescent winds are incapable of removing a significant fraction of H-envelope, and as such stars in the $20-40M_{\odot}$ range would be unable to form stripped type stars via single star evolution. However, it has been suggested that dust-enshrouded RSGs (DE-RSGs) may represent a short-

lived, high mass-loss phase with the ability to peel away a large fraction of H-envelope in a short space of time. Indeed, some models do adopt enhanced mass-loss for at least a fraction of the RSG phase (e.g. Geneva), motivated by the van Loon et al. 2005 prescription (hereafter vL05 [8]), which was derived from a sample of DE-RSGs identified in the Large Magellanic Cloud (LMC).

The vL05 sample were selected based on their large mid-IR excess and, in some cases, strong maser emission, both indicative of strong mass-loss. Despite their rarity ([9] find that above a luminosity of $\log L/L_{\odot} = 5.0$ only 9 out of 73 cool supergiants are DE-RSGs), the \dot{M} of the vL05 DE-RSG sample are claimed to be more than a factor of 10 higher than the quiescent mass-loss seen in the cluster RSGs [5, 6], which could potentially allow a significant fraction of H-envelope to be removed in a short amount of time.

However, the definition of a DE-RSG is somewhat subjective. Quiescent mass-loss throughout the RSG phase is only able to remove $\sim 1M_{\odot}$ of material. As such, we define the DE-RSG phase by quantifying how strong the mass-loss would need to be to remove a large enough fraction of H-envelope and force an RSG to evolve back to the blue of the HRD. To achieve this a star would need to be experiencing mass-loss rates of $1 \times 10^{-4}M_{\odot} \text{ yr}^{-1}$ for around 10% of the $\sim 10^6$ yr RSG phase. This would strip $10M_{\odot}$ of material, and allow the star to return to the blue of the HRD and die as a H-poor supernova. The high mass loss would result in high extinction ($A_V > 2$ mag) and a large infrared excess (see Figure 1 in [10]).

Using an updated photometric catalogue of RSGs in the LMC we take another look at the purported DE-RSGs, and find that in colour-magnitude space they *do not stand out as a unique group*, in conflict with the suggestion they represent a specific phase of evolution for all RSGs (see Figure 2). Instead, we find that only 1 object in the entire LMC, WOH G64, fits the necessary criteria to be classified as a bona-fide DE-RSG, having a high optical extinction (> 8 mag) and a high mass-loss rate ($> 10^{-4}M_{\odot} \text{ yr}^{-1}$).

If DE-RSGs *do* represent a short lived phase of massive star evolution it is extremely short lived (lasting less than 3% of the RSG lifetime), and likely only able to remove $\leq 2M_{\odot}$ of material. This is *not enough* to drive a

single star back to the blue of the HRD.

Overall, this means that low-luminosity Wolf-Rayet stars, blue supergiants, and luminous blue variables are unlikely to arise from post-RSG evolutionary phases in single stars. It also means that the relatively low initial mass progenitors of Type Ibc and Type IIb SNe ($M_{ZAMS} \leq 40M_{\odot}$) cannot form via a single-star pathway. Crucially, since above $40M_{\odot}$ most stars exist in binaries [11], we can effectively rule out the single star evolutionary pathway for the formation of stripped stars and supernovae entirely. Instead, we suggest that the ratio of stripped and unstripped SNe is driven by binarity.

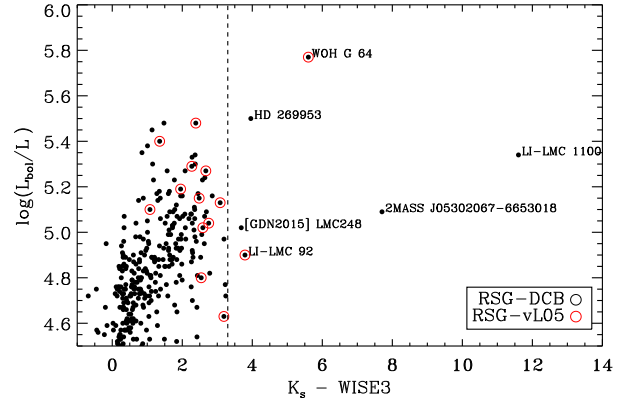


Figure 2: Colour-magnitude diagram for cool supergiants in the LMC. Red circled objects represent the original DE-RSG sample. Taken from [10].

References

- [1] Smartt, S., 2009, MNRAS, 395, 1409
- [2] Georgy, C., 2012, A&A, 538, L8
- [3] de Jager, C., et al., 1988, A&AS, 72, 295
- [4] Maun & Josselin, 2011, A&A, 526, A156
- [5] Beasor, E., & Davies, B., 2018, MNRAS, 475, 55
- [6] Beasor, E., et al., 2020, MNRAS, 492, 5994
- [7] Choi, J., et al., 2016, ApJ, 823, 102
- [8] van Loon, J. Th., et al., 2005, A&A, 442, 597
- [9] Davies, B., et al. 2018, MNRAS, 478, 3138
- [10] Beasor, E., & Smith, N., 2022, ApJ, 933, 41
- [11] Sana, H., et al., 2012, Science, 337, 444

Short CV



2015: Master in Astrophysics, University of Liverpool, UK
 2015–2019: PhD in Astronomy, Liverpool John Moores University, UK
 2019–2022: NASA Hubble Fellow, NSF’s NOIRLab, USA
 2022–present: Bok Fellow, University of Arizona, USA

A molecular window into the mass loss history of Luminous Blue Variables

Cristobal Bordiu

INAF, Osservatorio Astrofisico di Catania, Catania, IT, 95123, Italy

When massive stars ($M > 8 M_{\odot}$) leave the Main Sequence, they undergo a series of transitional stages before meeting their fate as core-collapse supernovae. In this interlude, massive stars lose a significant fraction of their initial mass, heavily altering their surroundings from a chemical and dynamical perspective. A proper characterization of this transition is thus crucial to better constrain stellar evolution and measure the impact of these evolved sources at a Galactic scale. Among these post-Main Sequence stages, the Luminous Blue Variable phase (hereafter LBV) is perhaps the most challenging one: a brief ($t \sim 10^4$ yr) episode in which the stars become unstable and exhibit the highest mass loss rates, produced by the combination of dense and steady winds, and sporadic outbursts or *eruptions*, able to expel up to a 10–20% of the stellar mass in very short timescales. These processes leave an unmistakable footprint in the surrounding ISM, triggering the formation of massive nebulae of dust and gas with strong hints of CNO processing. The study of such structures is a powerful diagnostic tool that sheds light on the elusive nature of LBV stars, allowing for an accurate reconstruction of their mass-loss record and disentangling their complex, time-dependent interaction with the ISM. For years, this work has mostly involved a synergistic approach that combines far-infrared and radio continuum observations, tracing the dust and ionised gas content of the nebulae [1, 2, 3]. While these studies have played an invaluable role to better understand the mass-loss processes of LBV stars, the global picture is still unclear, and many questions remain unanswered: the mechanisms behind the eruptions, the factors determining the shaping of the ejecta, and the total mass-loss budget are still uncertain.

The missing piece of the puzzle

The possible existence of a molecular component associated with LBV nebulae was long overlooked due to the unsuitable conditions found in the outskirts of these stars (e.g., very high temperatures, intense UV radiation beyond the Lyman limit). However, in the last two decades, a few molecular spectroscopy works challenged the accepted vision of LBV mass-loss as a two-piece puzzle. The detection of H_2 in the Homunculus Nebula around η Car [4] constituted a remarkable milestone, followed by the discovery of conspicuous circumstellar shells and hot clumps of CO [9] and NH_3 [10] around G79.29+0.46. These findings, along with a handful of loosely related structures in other sources, hinted at a non-negligible, unseen mass component that must be considered to properly characterize the interplay between LBVs –and, more generally, evolved massive stars– and the ISM. Even so, disentangling a putative circumstellar molecular gas component from nearby molecular clouds, e.g.,

telling apart compressed ISM material and molecular gas formed *in situ* out of ejecta, is only possible by the combination of indirect morpho-kinematic, physical and chemical criteria. In this respect, the detection of less abundant molecules towards the waist of the Homunculus, including N- and O-bearing species with extremely low $[^{12}C/^{13}C]$ isotopic ratios [6], set a valuable precedent, underlining the potential of LBVs as molecular polluters and paving the ground for further in-depth studies.

Spurred on by the possibility of this molecular component being a widespread feature among the LBV population, we initiated an observational campaign to search for molecular gas towards a sample of Galactic LBV stars that exhibit signposts of eruptive mass loss (i.e., circumstellar dusty nebulae).

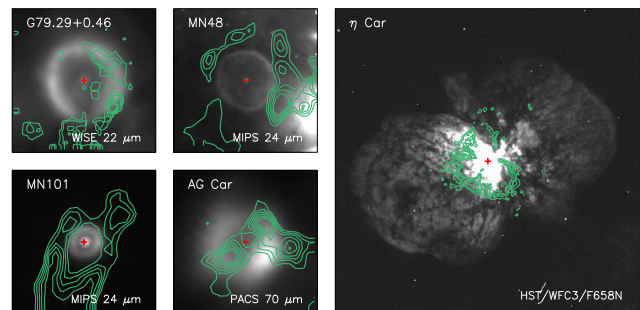


Figure 1: Shells and rings of CO around LBV stars.

A story of shells and rings

The main outcome of this campaign is the detection of a new type of structure associated with LBV stars: large, slowly expanding CO rings, found around the sources MN101 [11] and AG Car [12] –observed with the IRAM-30m telescope, and with APEX and ALMA, respectively. The rings, depicted in Figure 1, bottom panels, have sizes of 0.2 and 0.4 pc, and show strikingly low expansion velocities, of less than 5 km s^{-1} . This value, barely supersonic, is extremely puzzling, falling below the typical expansion velocities of LBV nebulae (~ 1 dex). Employing non-LTE radiative transfer modelling, we estimated the physical conditions of the rings. The molecular gas is relatively diffuse ($n_{H_2} \sim 10^3 \text{ cm}^{-3}$), warm ($T_k \sim 50 \text{ K}$) and moderately optically-thick ($\tau \sim 1$), showing notable differences with respect to nearby interstellar clouds. The rings seem to be aligned with the equatorial plane of the stars –which has been confirmed for AG Car–, thereby tracing some sort of equatorial density enhancement. However, pinpointing the exact origin of the molecules is tricky. As discussed above, they could have arisen from interstellar material piled up by the stellar wind, or from stellar ejecta. The $[^{12}C/^{13}C]$ ratios measured in the two rings –using $[^{12}CO/^{13}CO]$ as a proxy–, lower than

the standard ISM value and hence suggesting a moderate degree of CNO processing, may support the ejection scenario. Moreover, the masses of the rings are also consistent with a stellar origin, being 0.6 ± 0.1 and $2.7 \pm 0.9 M_{\odot}$ for MN101 and AG Car, respectively. As thoroughly discussed in [13], binarity and fast rotation seem to favour the formation of these rings. While MN101 is an almost unexplored object, AG Car is a well characterized LBV, known to be a fast rotator. Changes in the wind properties at low latitudes due to the nearly critical rotation and subsequent gravity darkening may induce a slower and denser wind near the equator, in which molecules could form and survive more efficiently. Similarly, the presence of a companion, as recently proposed following VLT observations [15], could result in non-conservative mass transfer episodes that would lead to the formation of an expanding ring. Nevertheless, these hypotheses need further observations and modelling work to be confirmed.

In contrast to these equatorial rings, we also found molecular structures that follow a remarkably isotropic distribution. Using APEX, we identified several shells of CO around MN48, a LBV that constitutes the best analogue of G79.29+0.46: the central star is surrounded by a shallow dusty shell, allegedly interacting with a nearby HII region (Figure 1, top panels). As in G79.29+0.46, the molecular shells, with a mass of $\sim 10 M_{\odot}$, show dynamical signatures of interaction towards the SW [14].

The uniqueness of η Car

η Car is a special object, a massive binary system composed of a $\sim 100 M_{\odot}$ LBV, and a less massive ($\sim 30 M_{\odot}$) companion. The LBV underwent a violent outburst in the mid 19th century, nicknamed the Great Eruption, perhaps triggered by a merger in a triple system. This cataclysmic event gave birth to the Homunculus Nebula, a massive bipolar nebula expanding at very high speeds. Sitting in the waist of the Homunculus, there is a partially disrupted circumstellar torus ($r \sim 4000$ au), resolved in CO [5, 12] (Figure 1, right panel). This torus, dynamically linked to the Great Eruption ($v_{\text{exp}} \sim 120 \text{ km s}^{-1}$) is the main molecular reservoir of η Car [7]. Analysing ALMA band 7 archival observations, we disclosed the HCN and HCO⁺ counterpart of the CO torus, along with molecular emission in the region of the so-called inner ejecta, debris expelled in a lesser eruption in the 1890s. As shown in [12], this emission arises from "hot bullets" of HCN -detected also in their vibrationally-excited transitions-, located extremely close to the central stars, a hostile region where other molecules have been reported [8].

Implications and prospects

Our results consolidate the evidence that survival of molecules in the outskirts of LBV stars is the norm rather than the exception. Molecular gas is a key ingredient of

the CSM around LBV stars, and more importantly, it conveys an essential side of their mass-loss history. From shells to rings, the study of this component opens a path to disclose the complex interplay between evolved massive stars and their surroundings. In those cases where molecular gas can be confidently linked to stellar ejecta, we proved that it may represent a substantial fraction of the total mass loss budget ($\geq 30\%$), thus having important repercussions on stellar evolution models, very sensitive to the adopted mass-loss rates. Finally, regarding the intriguing rings of MN101 and AG Car, and their much younger "relative" in η Car, we combined our results with literature data of other (dusty) rings around LBV-like objects, finding an empirical relation that suggests a common dynamical scenario, in which the same type of structure evolves in similar environments (see Figure 2).

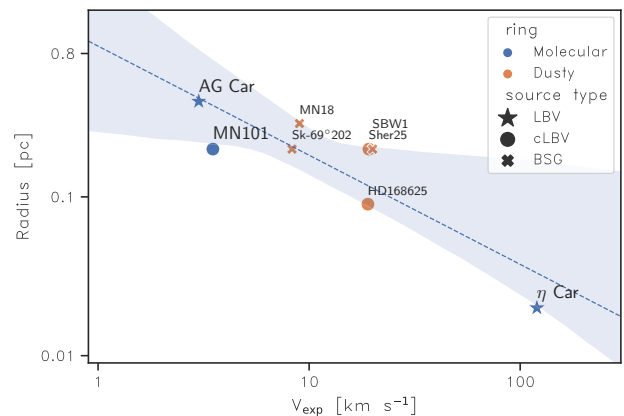


Figure 2: Radius versus expansion velocity of LBV rings.

Taken altogether, these results highlight the important role of mm/sub-mm spectroscopy in building an accurate portrait of the CSM around evolved massive stars. This has profound astrophysical implications, reframing the role of evolved massive stars as molecular factories, and improving the current understanding of the environment where core-collapse supernovae take place.

References

- [1] Duncan, R. A., & White S. M., 2002, MNRAS, 330, 63
- [2] Umana, G., et al., 2005, A&A, 437, L1
- [3] Buemi, C. S., et al., 2010, ApJ, 721, 1404.
- [4] Smith, N., & Davidson, K., 2001, ApJL, 551, L101
- [5] Smith, N., et al., 2018, MNRAS, 474, 4988
- [6] Loinard, L., et al., 2012, ApJL, 749, L4
- [7] Gull, T. R., et al., 2020, MNRAS, 499, 5269
- [8] Morris, P. W., et al., 2020, ApJL, 892, L23
- [9] Rizzo, J. R., et al., 2008, ApJ, 681, 355
- [10] Rizzo, J. R., et al., 2014, A&A, 564, A21
- [11] Bordiu, C., et al., 2019, MNRAS, 482, 1651
- [12] Bordiu, C., & Rizzo, J. R., 2019, MNRAS, 490, 1570
- [13] Bordiu, C., et al., 2021, MNRAS, 500, 5500
- [14] Bordiu, C., et al., in prep.
- [15] Mahy, L., et al., 2022, A&A, 657, A4

Short CV



2008–2014: BSc in Telecommunication Engineering, Universidad de Oviedo, Spain
 2014–2015: MSc in Astrophysics, Universidad Internacional de Valencia, Spain
 2016–2021: PhD in Astrophysics, Universidad Complutense de Madrid, Spain
 2020–present: Research Fellow, INAF Osservatorio Astrofisico di Catania, Italy

Gaia keeps on delivering: expanding the open cluster population with EDR3

Alfred Castro-Ginard

Leiden Observatory, Leiden University. Niels Bohrweg 2, 2333 CA Leiden, The Netherlands.

The improvements in the precision of the astrometric data, particularly of the parallax and proper motion measurements, of *Gaia* EDR3 with respect to *Gaia* DR2 provides the opportunity to search for farther and fainter open clusters (OCs) that have so far been undetected. This will allow us to have a more complete view of the OC population in the Milky Way, enabling studies about the structure and the evolution of our Galaxy.

The OCfinder method

In order to blindly search for OCs in *Gaia* data, we have developed the method `OCfinder` [see 2, for a detailed explanation]. The method, devised in [2] and successfully applied to find hundreds of new open clusters in [3, 4, 6], consists in two well-known machine learning algorithms. First, we apply a density-based clustering method, DBSCAN [7], to find statistical stellar overdensities in the five astrometric dimensions (*i.e.* position, parallax and proper motion). Second, we classify these overdensities into random statistical or real open clusters using an artificial neural network [ANN, 8] trained to identify isochrones in a color-magnitude diagram (CMD).

We apply the methodology to 232 463 114 stars in the Galactic disc, defined as $|b| < 20^\circ$, up to magnitude $G = 18$. We enable the analysis of such a large number of stars thanks to the deployment of the methodology in a Big Data environment [4], *i.e.* the MareNostrum Supercomputer located in the Barcelona Supercomputing Centre**.

New open clusters in EDR3

The application of `OCfinder` to *Gaia* EDR3 data results in the discovery of 628 new open clusters, together with the re-detection of about 80% of the open clusters characterised with *Gaia* DR2 data [1]. As shown in Figure 1, the OCs found in *Gaia* EDR3 are in general more compact in both proper motion and parallax. This is due to i) the improvements on the astrometric precision of *Gaia* EDR3 with respect to *Gaia* DR2, and ii) the fact that we expand the search up to $G = 18$ (compared to our previous searches up to $G = 17$), which allow us to detect farther objects. In fact, out of the 628 new OC, only three objects are closer than 1 kpc, and 75 objects are located within 1 and 2 kpc. This is due to a better completeness of previous surveys in these regions, together with the aforementioned methodological effects.

The Table with the new UBC clusters can be found online at the CDS^{††}. It contains, for each cluster, information about the mean astrometric parameters (including radial velocity when available), together with the number of members of each cluster and an estimation of the age,

distance and line-of-sight extinction. The clusters are divided into class A, class B and class C, according to their reliability which we assess by inspecting the distributions of the member stars in the astrometric dimensions and the CMD, aided with the radial velocity measurements when available.

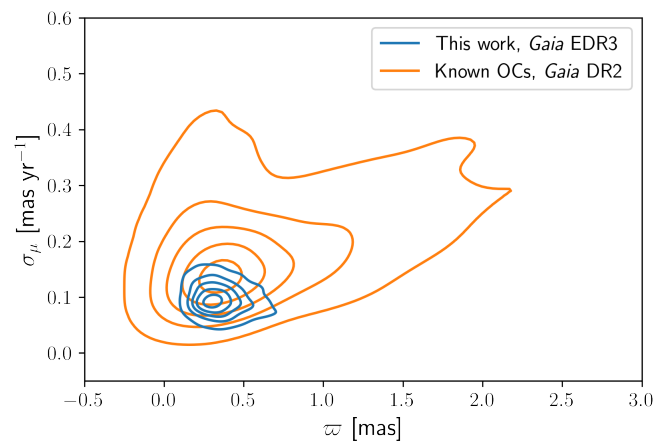


Figure 1: Total proper motion dispersion as a function of parallax for the OC characterised in DR2 (orange) and EDR3 (blue).

Ages, distances and line-of-sight extinctions

For each of the newly detected OCs, we estimate their age, distance and line-of-sight extinction. The estimation is done using an ANN trained on well-characterised open clusters [see 1, for details on the ANN]. The ANN takes the CMD of the OC member stars, together with the OC mean parallax and two additional quantities derived from the CMD to aid the estimation. By comparing their results with the reported values of the well-characterised OC in the training set, [1] report the uncertainties of their estimation of log age to be in the range from 0.15 to 0.25 dex for young clusters (≤ 8.5 dex), and from 0.1 to 0.2 dex for older OCs. The uncertainties for the extinctions range from 0.1 to 0.2 dex in A_v , and in the case of the distance modulus the uncertainties are also within 0.1 and 0.2 dex, which correspond to a 5% to 10% uncertainty in distance.

Figure 2 shows a heliocentric spatial distribution of the known previous to *Gaia* EDR3 and newly detected OCs in different age bins. The increase in the OC population in the different age bins is seen when comparing known OC (triangles) and newly detected in *Gaia* EDR3 (crosses): (i) 703 and 276 known and new OC younger than 100 Myr, (ii) 675 and 248 known and new OCs from 100 to 500 Myr, (iii) 229 and 58 known and new OCs with ages within 500 Myr and 1 Gyr, and (iv) 260 and 46 known

**<https://www.bsc.es/marenostrum>

††<http://cdsarc.u-strasbg.fr/viz-bin/cat/J/A+A/661/A118>

and new OCs older than 1 Gyr. Moreover, in the younger bin, we find clear overdensities that trace the spiral arms [5]. These young overdensities are dispersed in the following older age intervals.

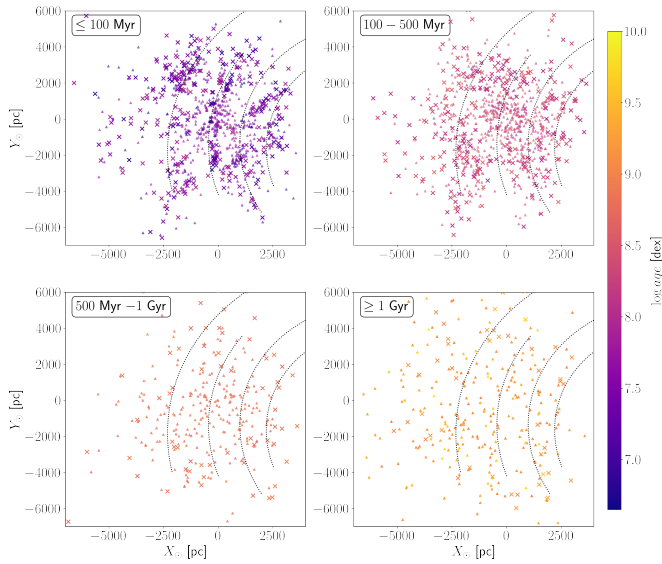


Figure 2: X_{\odot} vs Y_{\odot} distribution of the newly found OC (crosses) and OC characterised with DR2 data (triangles), for different age bins: younger than 100 Myr (top left), 100 – 500 Myr (top right), 500 Myr - 1 Gyr (bottom left) and older than 1 Gyr (bottom right). The dotted lines show the spiral arms fitted in [5].

OCs as tracers of the Milky Way spiral arms

As already seen in Figure 2 (top left panel), overdensities of young OCs trace the present-day locations of spiral arms. We used Gaussian mixture models to detect these overdensities and relate them to the Perseus, Local, Sagittarius and Scutum spiral arms [see 5, for a description of the method and a summary of the main results]. Once the present-day spiral arms are described, we trace back the OCs associated with the each spiral arm to their birth position [using radial velocities compiled in 9] to find the evolution of these spiral arms for the last 80 Myr [5].

We find that each spiral arm has its own pattern speed, discarding a common pattern speed for all the spiral arms explored. Moreover, the different spiral pattern speeds decrease as their Galactocentric radius in-

crease, closely following the Galactic rotation curve. This behaviour of the Galactic spiral arms allow us to disfavour classical density waves as the main mechanism for the formation of the Milky Way spiral arms, favouring short-lived transient spirals.

Summary and outlook

This contribution presented the OCfinder method, devised to automatically search for OC in *Gaia* data, and its application to *Gaia* EDR3. So far, about 1300 OCs have been detected with OCfinder, representing almost 50% of the currently known OC population. This shows the importance of using machine-learning aided methodologies to extract knowledge and better understand the high-quality data provided by surveys as *Gaia*.

We also showed how an improved OC census, both in terms of quantity of OCs and quality of their estimated parameters, can improve the science we derive from this population. By tracing the Milky Way spiral arms with OCs, we found that the mechanisms driving the formation of the spiral arms in our Galaxy are in better agreement with simulation-based approaches that tend to favour a transient nature.

The next *Gaia* DR3 release, will provide more complete information about the Solar neighbourhood. In particular, and relevant for OCfinder, *Gaia* DR3 will add radial velocity measurements for 33 million stars with $G_{RVS} < 14$, adding an extra dimension to not only help the search for new OCs but also to improve the characterisation of the known OC population. The volume of available high-quality data will only increase with future *Gaia* data releases, as well as with future photometric and spectroscopic surveys, therefore the need for improved and more robust data-driven machine-learning methodologies.

References

- [1] Cantat-Gaudin, T., et al. 2020, A&A, 640, 1.
- [2] Castro-Ginard, A., et al. 2018, A&A, 618, 59.
- [3] Castro-Ginard, A., et al. 2019, A&A, 627, 35.
- [4] Castro-Ginard, A., et al. 2020, A&A, 635, 45.
- [5] Castro-Ginard, A., et al. 2021, A&A, 652, 162.
- [6] Castro-Ginard, A., et al. 2022, A&A, 661, 118.
- [7] Ester, M., et al. 1996, Proceedings of the Second International Conference on Knowledge Discovery and Data Mining KDD'96 (AAAI Press) 226.
- [8] Hinton, G., 1989, Artif. Intell., 40, 185.
- [9] Tarricq, Y., et al. 2021, A&A, 647, 19.

Short CV



2016–2017: MSc in Astronomy, University of the Balearic Islands, Spain
 2017–2021: PhD in Astronomy, University of Barcelona, Spain
 2021–present: Postdoctoral researcher, Leiden Observatory, The Netherlands

Unveiling the mass assembly history of the Milky Way via its stellar halo

Danny Horta

Astrophysics Research Institute, Liverpool John Moores University, 146 Brownlow Hill, Liverpool, UK

Stellar haloes are important galactic components that retain vital clues towards deciphering how galaxies assemble their mass and evolve over time. It is in these regions where the debris from disrupted satellite galaxies resulting from the hierarchical formation of galaxies – a fundamental prediction of Lambda Cold Dark Matter – are found, as well as the debris from dissolved/evaporated globular clusters (GC). Therefore, albeit it only amounting to $\sim 1\%$ of the total stellar mass in the Milky Way, the Galactic stellar halo is a pivotal region to study encoding many clues about our Galaxy formed and evolved.

The advent of large-scale stellar surveys, and specifically the *Gaia* mission, has revolutionised how we study the Galaxy. The ability to chemo-dynamically mark millions of stars in the Milky Way has enabled the characterisation of stellar populations in every region of the Galaxy. Of particular importance has been the discovery of phase space substructure in the Galactic stellar halo [1, 2, 3, 4], conjectured to be the remnants of past encounters between cannibalised satellite galaxies and/or disrupted GCs with the Milky Way. While such discoveries have helped tremendously in the efforts to disentangling how the Milky Way formed and evolved, there still remains a debate of how many past accretions the Galaxy encountered, and how much mass is comprised from accreted galaxies and/or disrupted GCs.

Accretion history of the Milky Way: Heracles

The central few kpc of the Galactic halo are obviously extremely important when it comes to retelling the early accretion history of the Milky Way and discerning the contribution of in situ formation to the stellar halo mass. This is because: *i*) it is within the central $\sim 3\text{-}4\text{ kpc}$ that approximately 50% of the mass of the stellar halo is contained; *ii*) it is the region one would expect to find the debris from massive and/or early accreted systems; *iii*) it is also the region one would expect to host most of the early in situ halo star formation, including the oldest stars in the Galaxy. However, observational access to inner halo populations is quite difficult due to dust extinction and overcrowding.

Here, we use the combination of APOGEE spectroscopy and *Gaia* astrometry to chemo-dynamically characterise stellar halo populations in the innermost regions of the Galaxy. Utilising a chemical dissection in the $[\text{Mg}/\text{Mn}]\text{-}[\text{Al}/\text{Fe}]$ plane, we split stellar populations likely formed in/ex-situ and then study their integrals of motion (IoM). Upon identifying a new overdensity in the "accreted" group, we set out to analyse its chemo-dynamical properties by comparing the chemical compositions and IoM with its co-spatial in-situ counterpart populations. We find that this new substructure (dubbed Heracles) presents chemo-dynamical properties that are consistent

with an accretion origin. Additionally, we perform several tests to assess the reality of Heracles, such as examining if it statistically can be modelled and as independent component in multiple 2D chemical planes, and contrasting its properties to expectations from the EAGLE cosmological simulations; we find that Heracles survives these tests, reinforcing our initial accreted scenario hypothesis. In summary, the properties of Heracles suggest it is the remnant of an early accreted and massive disrupted satellite galaxy [5].

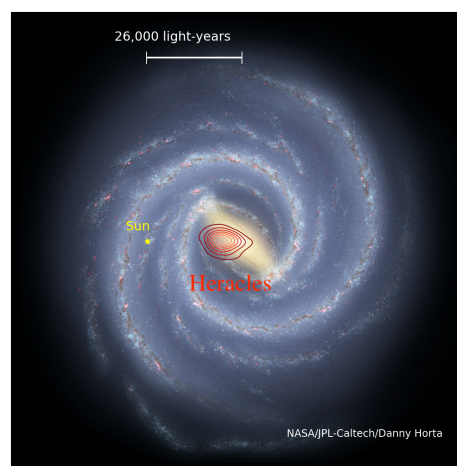


Figure 1: An artist's impression of what the Milky Way might look like seen from above. The red rings show the rough extent of the fossil galaxy known as Heracles. The yellow dot shows the position of the Sun.

Revealing the reality and nature of halo substructures

In the past few years, several distinct satellite accretions have been suggested by various groups [1, 2, 3, 6, 7, 8]. While the identification of these substructures is helping constrain our understanding of the mass assembly history of the Milky Way, their association with any particular accretion event still needs to be clarified. Along those lines, predictions from numerical simulations suggest that a single accretion event can lead to multiple substructures in phase space [9, 10]. Therefore, in order to ascertain the reality and/or distinction of these accretion events, one must resort to additional chemical composition information for large samples.

Here, we perform a detailed chemical composition comparison of halo substructure in the Milky Way (identified using selection techniques from previous work) using a homogeneous catalogue obtained by cross-matching the latest APOGEE and *Gaia* data [11]. By performing first a qualitative, and then second a quantitative comparison, we further disentangle the reality and nature of the following halo substructures: *Gaia*-

Enceladus/Sausage (GES), Heracles, Sagittarius dSph, Sequoia, Helmi stream, Thamnos, Aleph, LMS-1, Arjuna, l'itoi, Nyx, Icarus, and Pontus. A summary of our findings is shown in 2. In short, our results show that many halo substructures conjectured to be debris from individual accretions likely belong to either the omnipresent GES or to in situ populations, and that the Milky Way likely underwent three major mergers so far: Heracles, GES, Sagittarius dSph.

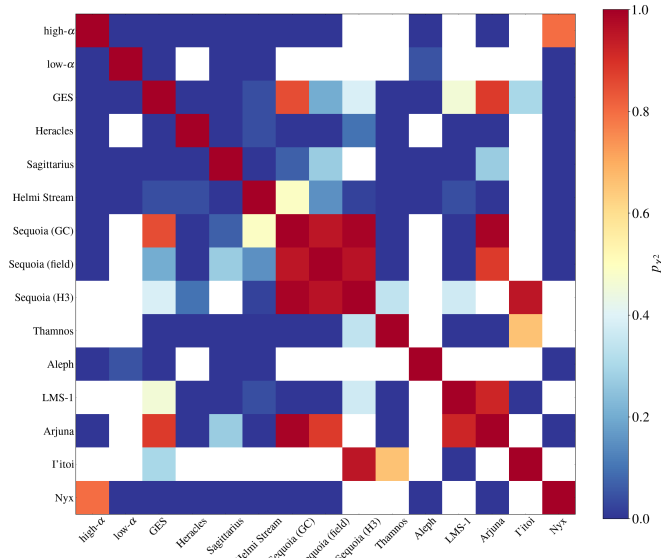


Figure 2: Confusion matrix of the χ^2 probability values obtained when comparing the chemical compositions of all the halo substructures with each other and with a high-/low- α discs. Here, each substructure is compared with its counterpart using a $[\text{Fe}/\text{H}]$ value that is well covered by the data, where red(blue) signifies a high(low) probability of two systems being statistically equal given their chemical compositions. Comparisons with blank values are due to the two substructures being compared not having any overlap in $[\text{Fe}/\text{H}]$.

The mass contribution from globular clusters to the Galaxy

The contribution of dissolved and/or evaporated globular clusters (GC) to the stellar content of the Galaxy is a key constraint on models of GC formation and the mass assembly history of the Milky Way. Earlier results from APOGEE pointed to a large contribution of destroyed GCs to the stellar content of the inner halo [4], by as much as 25 per cent per cent, which is an order of magnitude larger than previous estimates for more distant regions [12]. We set out to measure the ratio between nitrogen-rich (N-rich, namely second population GC stars

now in the halo field) and normal halo field stars, as a function of distance, by performing density modelling of halo field populations in APOGEE DR16, accounting for the survey selection function effects. Our results show that at 1.5 kpc from the Galactic Centre, N-rich stars contribute a much higher $16.8^{+10}_{-7}\%$ fraction to the total stellar halo mass budget than the $2.7^{+1}_{-0.8}\%$ ratio contributed at 10 kpc [13]. Under the assumption that N-rich stars are former GC members that now reside in the stellar halo field, and assuming the ratio between first and second population GC stars being 1:2, we estimate a total contribution from disrupted GC stars of the order of $27.5^{+15.4}_{-11.5}\%$ at $r = 1.5$ kpc and $4.2^{+1.5}_{-1.3}\%$ at $r = 10$ kpc. Furthermore, we integrate such density within a spherical shell from 1.5 to 15 kpc in radius, and find a total stellar mass arising from dissolved and/or evaporated GCs of $M_{\text{GC, total}} = 9.6^{+4.0}_{-2.6} \times 10^7 M_{\odot}$.

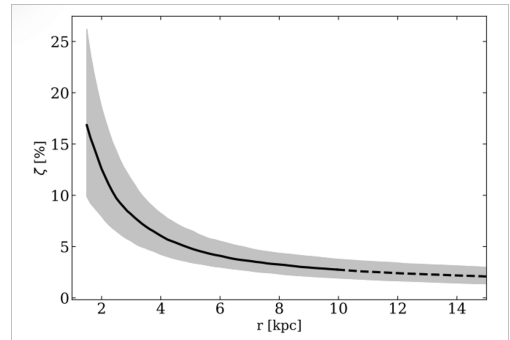


Figure 3: Mass density percentage ratio of N-rich stars and halo field stars as a function of spherical radius, where black(grey) are the median($1\text{-}\sigma$) values; the dashed line indicates the Galactocentric distance range where the density is not well constrained due to low numbers of N-rich stars. See text for details.

References

- [1] Belokurov, V., et al. 2018, MNRAS, 478, 1
- [2] Helmi, A., et al. 2018, Nature, 563, 7729
- [3] Ibata, R., et al. 1994, Nature, 370, 6486
- [4] Schiavon R. P., et al. 2017, MNRAS, 465, 1
- [5] Horta D., et al. 2021, MNRAS, 500, 1
- [6] Myeong G., et al. 2019, MNRAS, 488, 1
- [7] Naidu, R., et al. 2020, ApJ, 901, 1
- [8] Koppelman, H., et al. 2019, A&A, 631
- [9] Jean-Baptiste, I., et al. 2017, A&A, 604
- [10] Koppelman, H., et al., 2021, A&A, 642
- [11] Horta, D., et al., 2022, eprint, arXiv:2204.04233
- [12] Martell, S. L., Grebel, E. K., 2010, A&A, 519
- [13] Horta, D., et al. 2021, MNRAS, 500, 4

Short CV



2017: Bachelors in Physics with Astrophysics, Northumbria University, Newcastle, UK
 2018: Masters in Physics with Astrophysics, Northumbria University, Newcastle, UK
 2022: PhD in Astrophysics, Liverpool John Moores University, Liverpool, UK

Tomography of evolved star atmospheres

Kateryna Kravchenko

Max Planck Institute for extraterrestrial Physics, Giessenbachstraße 1, 85748, Garching, Germany

Cool giant (AGB) and supergiant (RSG) stars are among the largest and most luminous stars in the Universe. They were extensively studied during last few decades, however their relevant properties like photometric variability and mass loss are still poorly constrained. Understanding these properties is crucial in the context of a broad range of astrophysical questions including chemical enrichment of the Universe, supernova progenitors, and the extragalactic distance scale.

Atmospheres of AGBs and RSGs are characterized by complex dynamics due to different interacting processes, such as convection, pulsation, formation of molecules and dust, and the development of mass loss. The state-of-the-art 3D radiative-hydrodynamics (RHD) simulations of AGBs and RSGs [1] are able to simulate some of those processes and produce a good agreement with the observed spectral features. However, the models lack constraints and need to be confronted to observables. A recently established tomographic method is an ideal technique for this purpose.

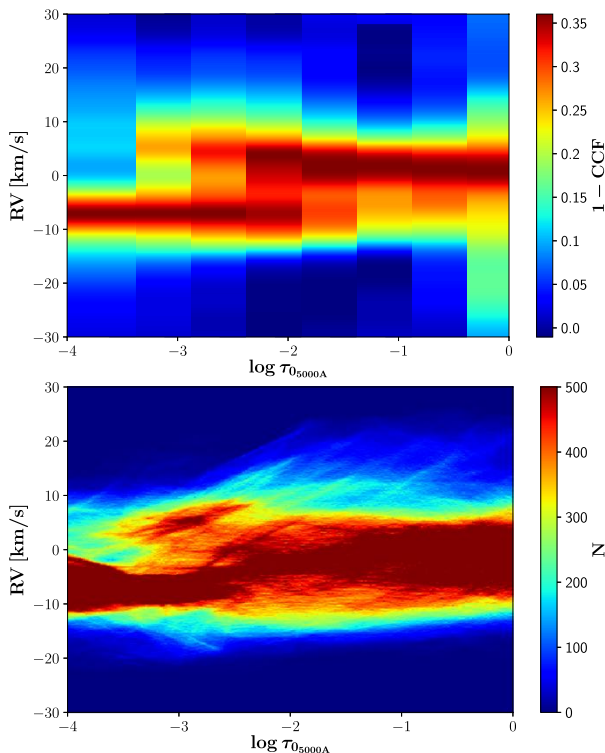


Figure 1: Reconstruction of velocity field as function of optical depth in the atmosphere. Top: cross-correlation of a 3D snapshot spectrum with the tomographic masks. Bottom: 3D snapshot velocity distribution.

Tomographic method

The tomographic method [2, 3] is based on cross-sectioning the stellar atmosphere in order to reconstruct the velocity field for each atmospheric layer. The method relies on the design of spectral templates (or

masks) containing lines forming at given, pre-specified ranges of optical depths. In order to correctly assess the depth of formation of spectral lines, the computation of a contribution-function was implemented by [3] in 1D radiative transfer code TURBOSPECTRUM [4], which performs spectrum synthesis from 1D static model atmospheres. The cross-correlation of the masks with observed or synthetic stellar spectra provides the velocity at different atmospheric depths. The tomographic technique was fully validated by cross-correlating a synthetic spectrum computed from a snapshot of a 3D RHD simulation [3] with a set of tomographic masks. The distribution of the line-of-sight velocity field throughout the atmosphere (known from the input model atmosphere) was nicely recovered (Figure 1). The following sections describe some of our applications of the tomographic method.

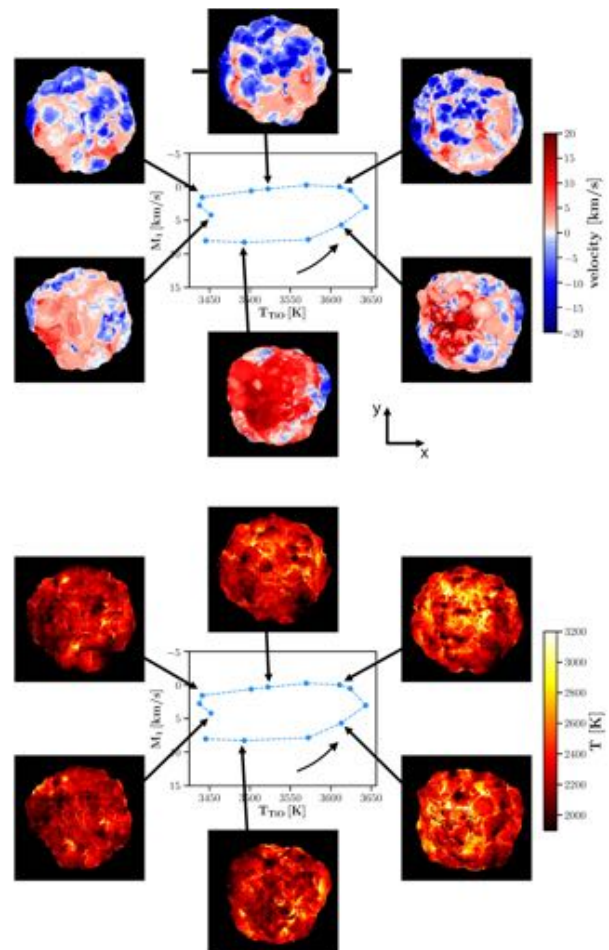


Figure 2: Evolution of velocity (top) and temperature (bottom) of the 3D simulation during a single photometric cycle represented by the hysteresis loop (center of each panel).

Interpretation of photometric variability in RSG stars

RSG stars are characterized by irregular photometric variations on timescales of hundreds of days. This ob-

served variability can correspond to a broad range of processes: atmospheric pulsations and/or convective motions, magnetic activity, binarity. In order to identify the responsible mechanism, the tomographic method was applied to time-series of high-resolution (HR) optical spectra of two RSG stars: μ Cep [5] and Betelgeuse [6]. A phase shift was detected between the radial velocity (RV) and photometric (as well as effective temperature) variations. This phase shift results in hysteresis loops in the temperature-velocity plane with timescales similar to the photometric ones. The application of the tomographic method to snapshots from 3D RHD simulations of a RSG atmosphere revealed similar hysteresis-like behavior in the temperature-velocity plane (Figure 2) with the lifetime consistent with the photometric timescales. The temporal variation of simulated velocity and temperature structures along a hysteresis loop (Figure 2) is indicative of atmospheric convective motions. The appearance of bright warm regions on the surface is followed by the rising material at same locations, which accounts for the phase lag between velocity and photometric variations and, thus, hysteresis loops. Therefore, convection plays a major role in the photometric variability of RSG stars.

Link between optical and geometrical depth scales

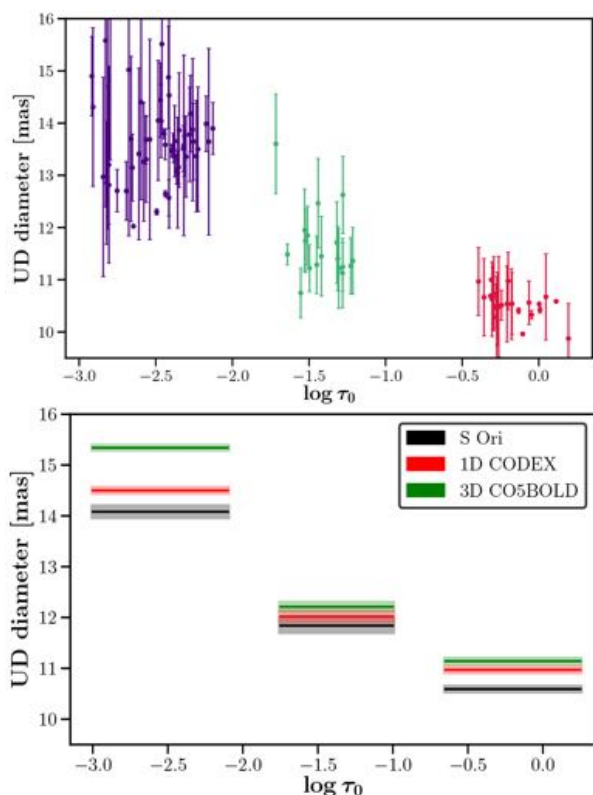


Figure 3: Relation between optical (x-axis) and geometrical (y-axis) depth scales for S Ori. Top: uniform disk (UD) fit of interferometric visibilities for each line of the three tomographic masks (different colors). Bottom: comparison with 1D and 3D dynamical models.

Current stellar atmosphere models of AGB and RSG stars provide a relation between optical and geometrical depth scales. However, this relation is sensitive to the stellar mass, which is ill-defined since these stars are undergoing a substantial mass loss. In addition, the models experience several limitations. For example, 3D RHD simulations are able to represent convection and pulsation processes, but they do not yet include wind, radiation pressure, and magnetic field, all of which may affect the structure and dynamics of the atmosphere. Thus, the knowledge of the relation between optical and geometrical depth scales from observations would open a way to test and constrain the models.

The observed relation between optical and geometrical depth scales can be derived by applying the tomographic method to HR spectro-interferometric (e.g. VLT/AMBER or VLT/GRAVITY) observations. By extracting visibilities (i.e. the contrast of interferometric fringes) at wavelengths contributing to the tomographic masks, we can measure the extension of different atmospheric layers [7]. Figure 3 illustrates our pilot study of the Mira-type AGB star S Ori [7] where the link between optical (provided by the tomographic masks) and geometrical (provided by fitting the interferometric visibilities) depth scales is nicely recovered and compared to dynamical model atmospheres.

Conclusions

The tomographic method is a powerful and precise technique to probe different depths in stellar atmospheres. So far, its application to AGB and RSG stars allowed to interpret their photometric variability and recover a quantitative relation between optical and geometrical depth scales. The future prospects of the tomographic method include its application to a broader range of astrophysical objects, such as Cepheid variables and exoplanets, to reveal detailed structure and dynamics of their atmospheres.

References

- [1] Freytag, B., et al. 2012, *Journal of Computational Physics*, 231, 919
- [2] Alvarez R., et al. 2001, *A&A*, 379, 288
- [3] Kravchenko K., et al. 2018, *A&A*, 610, A29
- [4] Plez, B., 2012, *Astrophysics Source Code Library*. ascl:1205.004
- [5] Kravchenko K., et al. 2019, *A&A*, 632, A28
- [6] Kravchenko K., et al., 2021, *A&A*, 650, L17
- [7] Kravchenko K., et al., 2020, *A&A*, 642, A235

Short CV



2013–2014: Master in Astrophysics, Kharkiv, Ukraine
 2015–2019: PhD in Science, Brussels, Belgium
 2019–2020: ESO Fellow, Santiago, Chile
 2020–present: Post-doctoral researcher, MPE, Garching, Germany

A close look at young intermediate mass giant stars: clues of rotation and mixing

Linda Lombardo

GEPI, Observatoire de Paris, Université PSL, CNRS,
5 place Jules Janssen 92195 Meudon, France

In the search of a sample of metal-poor bright giant stars using Strömgren photometry, we serendipitously found a sample of 26 young (ages younger than 1 Gyr) metal-rich giants, with masses between 2.5 and 6 solar masses. Ten of these stars also rotate rapidly ($v \sin i > 10$ km/s). The high stellar masses imply that these stars were of spectral type A to B when on the main sequence. This evolutionary stage is not very well characterised by observations so far, because of the short time spent by stars in this phase. This sample of giant stars allows us a close look at this rapid evolution. It is an opportunity for testing the predictions of theoretical stellar tracks on the evolution of chemical abundances and rotational velocities.

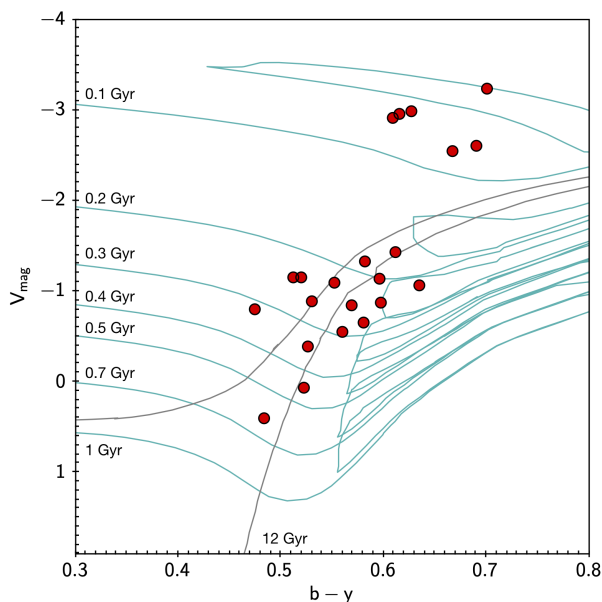


Figure 1: Strömgren colour-magnitude diagram of the observed stars. Cyan lines represent Parsec isochrones with solar metallicity and ages between 0.1 and 1 Gyr, while grey lines represent Parsec isochrones with $[\text{Fe}/\text{H}] = -2.0$ dex and age 12 Gyr.

Target selection

The stars in our sample were selected by chance, as our initial intention was to select stars with a metallicity estimated by photometry in the range $-2.5 \leq [\text{Fe}/\text{H}] \leq -1.5$. For the target selection we used the Strömgren photometry from the Paunzen [1] catalogue and the metallicity calibration for giants of Casagrande et al. [2]. Our sample stars appeared to have a photometric metallicity in the metal-poor range, however, the analysis revealed that they are actually metal-rich, with metallicities around solar, and some of them are rotating rapidly. The reason for this discrepancy is essentially due to age-metallicity

degeneracy in the colour-magnitude diagram. Young isochrones with solar metallicity overlap with old metal-poor isochrones in the region of the colour-magnitude diagram where the stars in our sample are located (Figure 1). We suspect that the Casagrande et al. [2] calibration performs poorly on young metal-rich stars because these stars were not used to define the calibration. However we are not sure if the degeneracy could be broken, even if these calibrators were used, without introducing some age-sensitive quantity in the calibration.

Potentially binary stars

Two stars in our sample (HD 195375 and HD 278) are listed in the Washington Double Star Catalogue [3]. We checked the Gaia astrometric parameters of these two binary systems, and we found that HD 195375 and its companion have consistent parallaxes, so they are in a physical binary system, while HD 278 and its companion have different parallaxes, which implies that these stars are probably not in a binary system. We looked for other possible binary stars in our sample by comparing our measured radial velocities with those of Gaia Data Release 2 (DR2) [4]. In particular, we looked for stars with Gaia DR2 radial velocity that differs by more than 5σ from our measured velocity, and Gaia DR2 radial velocity errors above 1 km/s. Ten stars in our sample have also been identified as probable binary stars by Kervella et al. [5] by comparing HIPPARCOS [6] and Gaia DR2 proper motions. We found that two stars (HD 192045 and HD 213036) show all the above mentioned properties. This suggests that they are likely binary stars.

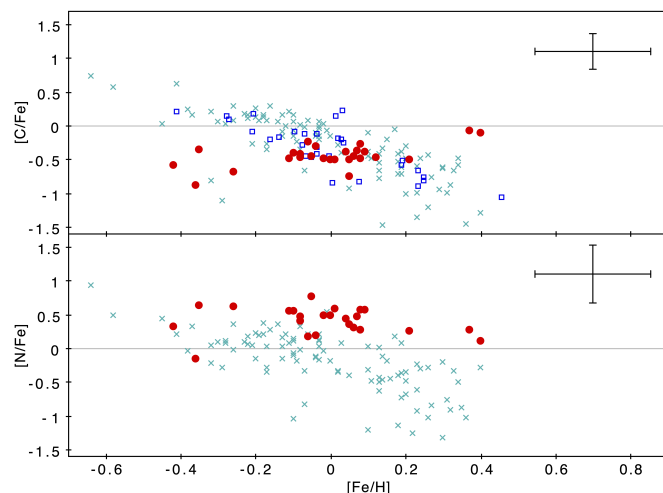


Figure 2: $[\text{C}/\text{Fe}]$ and $[\text{N}/\text{Fe}]$ abundance ratios as a function of $[\text{Fe}/\text{H}]$. Comparison with targets from Takeda et al. [7] (cyan crosses), and Royer et al. [8] (blue squares).

Chemical composition

We determined chemical abundances of 16 elements (C, N, O, Mg, Al, Ca, Fe, Sr, Y, Ba, La, Ce, Pr, Nd, Sm, and Eu) and rotational velocities of the stars using a set of high-resolution and high signal-to-noise spectra obtained with different spectrographs. The chemical analysis shows that all but two of the stars in the sample have low $[C/Fe]$ and high $[N/Fe]$ ratios (Figure 2). The $[(C+N+O)/Fe]$ ratio for these stars is almost constant and close to the solar value within the error bars. This pattern suggests that the material in the photosphere of the sample stars with sub-solar $[C/Fe]$ has been mixed with material that has experienced nuclear hydrogen burning through the CNO cycle. This interpretation is supported by the super-solar $[N/Fe]$ ratios and the constant $[(C+N+O)/Fe]$ ratio. The stars do not show any chemical peculiarities, except for the Ba abundance. The majority of the stars in the sample show a Ba abundance higher than solar, but solar neutron capture (n-capture) elemental abundances (Figure 3). The NLTE corrections for Ba lines are not sufficient to match the observed Ba abundances with the other n-capture abundances.

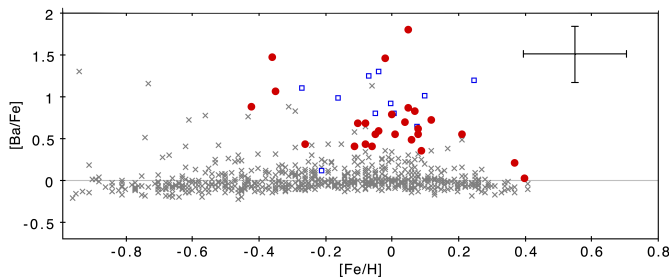


Figure 3: $[Ba/Fe]$ abundance ratios as a function of $[Fe/H]$. Comparison with targets from Bensby et al. [9] (grey crosses) and Royer et al. [8] (blue squares).

Because of the high Ba abundances, the stars in our sample might be Ba stars. According to de Castro et al. [10], the lower limit for Ba stars is $[s/Fe]=0.25$ dex, where $[s/Fe]=[Y/Fe]+[La/Fe]+[Ce/Fe]+[Nd/Fe]$. Only three stars in our sample have $[s/Fe]>0.25$, and only one star has $[s/Fe]=0.38$ (see Figure 4). These values are compatible with those of mild Ba stars. On the other hand, the other stars have $[s/Fe]$ values compatible with those of normal stars. In conclusion, the high $[Ba/Fe]$ ratios are puzzling and unexplained.

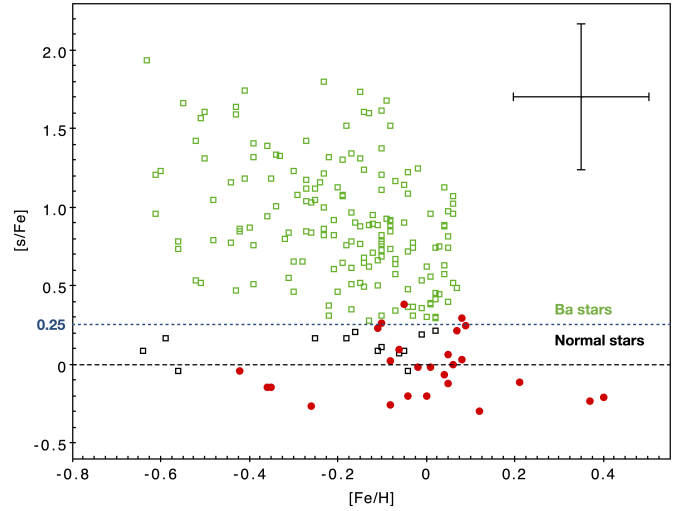


Figure 4: Mean $[s/Fe]$ abundance ratios as a function of $[Fe/H]$. Red circles represent $[s/Fe]$ ratio for the stars analysed in this work. Green squares represent Ba stars analysed in de Castro et al. [10]. Black squares represent the targets rejected as Ba stars in de Castro et al. [10].

Comparison with stellar evolution models

We measured the rotational velocities ($v \sin i$) of our sample stars and compared the results with theoretical models with rotation. We found a good agreement between the observed and predicted quantities. The $v \sin i$ we obtained for stars with $3.5 < M/M_{\odot} < 4$ and $-0.1 < [Fe/H] < 0.1$ ($5 < v \sin i < 22$ km/s) are compatible with the values of rotational velocity predicted by the Georgy et al. [11] models with $0.3 < \omega < 0.6$ ($\omega = \Omega_{in}/\Omega_{crit}$) at solar metallicity for stars in the corresponding region of the log T_{eff} versus log g diagram. We also found that the $[N/C]$ abundance ratios of our stars are compatible with the values predicted by rotational models for clump stars (the clump, or blue loop, is the region of the color-magnitude diagram where stars are located when they undergo central He-burning).

References

- [1] Paunzen, E., 2015, A&A, 580, A23
- [2] Casagrande, L., et al. 2014, ApJ, 787, 110
- [3] Mason, B. D., et al. 2001, AJ, 122, 3466
- [4] Brown, A. G. A., et al. 2018, A&A, 616, A1
- [5] Kervella, P., et al. 2019, A&A, 623, A72
- [6] ESA 1997, ESA Special Publication, 1200
- [7] Takeda, Y., et al. 2018, PASJ, 70, 91
- [8] Royer, F., et al. 2014, A&A, 562, A84
- [9] Bensby, T., et al. 2014, A&A, 562, A71
- [10] de Castro, D. B., et al. 2016, MNRAS, 459, 4299
- [11] Georgy, C., et al. 2013, A&A, 553, A24

Short CV



2016: BSc in Physics, Università di Pisa, Italy
 2019: MSc in Astrophysics and Cosmology, Università di Bologna, Italy
 2019–present: PhD student in Astrophysics, Observatoire de Paris - PSL University, France

Determination of polarimetric capabilities of the Thirty Meter Telescope

Ramya M Anche

Steward Observatory, University of Arizona, 933 North Cherry Avenue, Tucson, AZ 85721-0065, USA

Polarimetry is an important observational technique in astronomy in addition to photometry and spectroscopy. Polarization arises as a consequence of asymmetry; such as the presence of magnetic fields, interstellar dust, distribution of scattered radiation, etc. Polarization observations enable us to understand the nature and composition of dust, strength of magnetic fields, asymmetry in the structure of the source [1]. Currently, imaging/Spectropolarimeter has been an important instrument at many 1-10m class telescopes[2]. The polarimetric capability will be a crucial add-on to the imaging/spectroscopic instruments for the next-generation Extremely Large Telescopes (ELTs).

One potential problem for accurate polarimetry is the polarization introduced/modified by the telescope and instrument optics due to non-normal incidences on the optical surface. Non-zero polarization measured at the telescope focus for the unpolarized light, incident on the telescope, is Instrumental polarization (IP). The loss of input polarization is called depolarization (DP), and the conversion of linear to circular polarization (or vice versa) is crosstalk (CT) [3]. In addition to IP, CT, and DP, there may be polarization-induced aberrations; ex., coating-induced astigmatism, tilt, defocus, and chromatic aberrations [4, 5]. Polarization aberrations can cause ghost PSF during the high-contrast imaging of planets/disks. So estimation of these aberrations before the instrument design through modeling is crucial to ascertain their effect on the scientific observations.

Polarization is measured using Stokes parameters [6] which describe the polarization of light in terms of intensity measurements (I, Q, U, V). The 4×4 matrix representation which is used to study the interaction of polarized (or unpolarized) light with elements that modify the polarization is **Mueller matrix** given by Mueller [7].

The polarization effects introduced by telescope and instrument optics are usually corrected by polarization modeling and observations of standard polarized and unpolarized stars [8]. Here, We describe an analytical model (based on polarization ray tracing) developed to estimate the polarization effects for one of the next-generation large telescopes, the Thirty Meter Telescope (TMT).

Thirty meter Telescope

The Thirty Meter Telescope (TMT) is one of the large segmented mirror telescopes, proposed to be located in Mauna Kea, Hawaii, USA. It is a consortium between the USA, Canada, India, China, and Japan. The telescope is expected to have its first light in 2028 [9] The primary mirror is 30 m in diameter and made of 492 hexagonal segments, each measuring 1.44m across. An elliptical-

shaped Nasmyth mirror rotates and tilts to feed light to different instruments on the Nasmyth platform [10]. ††

[Polarization ray tracing algorithm for TMT](#)

In our model (Figure 1), we use Gemini coating[11] for all the three mirrors, and estimate instrumental polarization, crosstalk, and depolarization at the Nasmyth focus of TMT for $\lambda=0.4-2.5\mu m$ and field of view of $10'$. IP, CT, and DP are found to increase with the field angle due to the asymmetry and reduce with the wavelength due to the nature of the coating as shown in Figure 2. Nasmyth/fold mirror is the main source for the polarization effects in TMT[12].

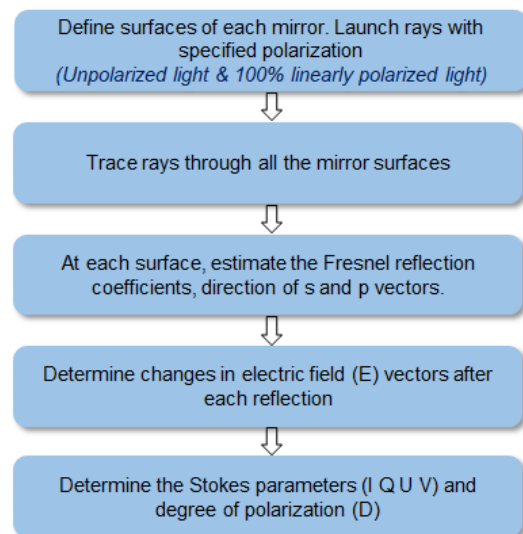


Figure 1: Algorithm for polarization ray tracing developed for TMT[13]

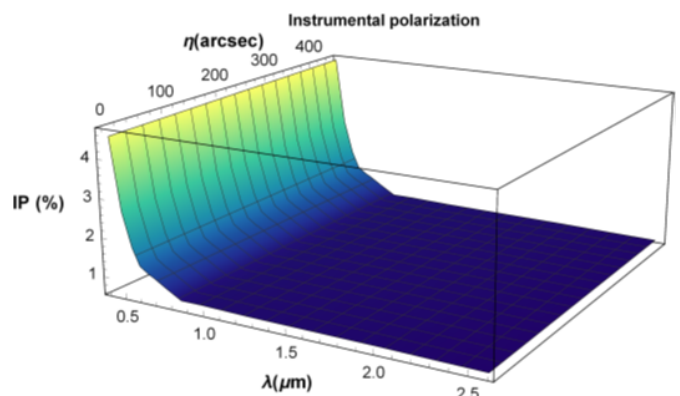


Figure 2: The variation of IP for semi field angle of $10'$ with the wavelength range of $0.4 \mu m$ to $2.5 \mu m$

The Mueller matrices are estimated for different in-

††<https://www.tmt.org/>

strument ports on the Nasmyth platform for different zenith angles of the telescope. The IP, CT, and DP are found to vary with the zenith angle of the telescope at all the instrument ports except at the Wide-field Optical Spectrograph (WFOS) port [10, 12].

Crossed mirror configuration for TMT for polarization cancellation

To reduce/cancel the polarization effects introduced by the Nasmyth mirror, another fold mirror can be added in the crossed configuration. This has been implemented successfully in the VLT telescope for SPHERE. Using a similar configuration shown in Figure 3, we have achieved polarization cancellation up to 10^{-3} (0.1%) from 4% and Linear to circular cross talk reduced to 4% from 70% in the blue region[14].

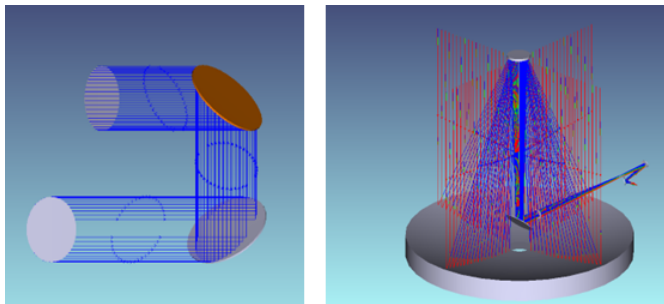


Figure 3: Crossed fold mirror configuration for TMT for polarization cancellation

To increase the accuracy of our estimation of IP, CT, and DP, we included the segments of the primary mirror in our model using optical design software Zemax. We analyzed the following effects with a segmented model: 1. Refractive index of silver and silicon nitride variation from segment to segment 2. Re-coating sequence of segments. 3. Tilt and Piston variation of segments.

Estimation of polarization aberrations

We have used the above ray tracing algorithm to estimate the polarization aberrations in the TMT in terms of Jones pupil maps. These aberrations give rise to the ghost PSF, which leads to ellipticity of the Airy disk. Polarization-induced aberrations in TMT are found to be coating-induced astigmatism ($\lambda/70$), tilt ($\lambda/12$ at $0.6\mu\text{m}$),

and chromatic aberration. The intensity of the ghost PSF generated due to polarization aberrations has also been estimated for the Narrow Field Infrared Adaptive Optics System (NFIRAOS) of TMT in Anche et al. [15].

Summary and Conclusions

We have modeled the polarization effects from the telescope optics of the Thirty Meter Telescope. Instrumental polarization varies from 4-0.6%, crosstalk varies from 70-10%, and depolarization varies from 2.5-0.8% in the wavelength range of $0.4\text{-}2.5\mu\text{m}$ for field angle zero. The polarization effect varies with the field angle and zenith angle of the telescope and, reduces with the wavelength (near/mid-infrared region). A mid-infrared instrument, MICH (Mid- Infrared Camera, High-disperser, and Integral field unit) could be a possible second-generation instrument with the polarimetric capability[16] for TMT.

References

- [1] Leroy, J.-L., 2000, Gordon Breach Science, c2000 (Advances in astronomy and astrophysics ; v.4)
- [2] Goldstein, D. H., 2003, CRC press
- [3] Sanchez Almeida, J., & Martinez Pillet, V. 1992, A&A, 260, 543
- [4] Chipman, R.A. 1987, The University of Arizona.
- [5] Breckinridge, J. B., et al. 2015, Pub. Astron. Soc. Pac, 127, 445
- [6] Stokes, G.G., 1852, *Philosophical transactions of the Royal Society of London*, 142, 463
- [7] Mueller, H. 1948, *Journal of optical society of America*, 38,661
- [8] Tinbergen, J., 2005, *Astronomical Polarimetry*, by Jaap Tinbergen, Cambridge, UK: Cambridge University Press, 2005
- [9] Sanders, G. H., 2013, *Journal of Astrophysics and Astronomy*, 34, 81
- [10] TMT Group., 2013, TMT. OPT. DRD 7, no. 006.
- [11] Vucina, T., et al., 2006, *Proceedings SPIE*, 6273, 62730W
- [12] Anche, R.M., et al. 2018, *Journal of Astronomical Telescopes, Instruments, and Systems* 4.1 (2018): 018003.
- [13] Anche, R.M., et al. 2015, *International Conference on Optics and Photonics 2015*. Vol. 9654. SPIE, 2015.
- [14] Anche, R.M.et al. 2018, *Journal of Optics* 47.2 (2018): 166-173.
- [15] Anche, R.M., et al. 2018, *Adaptive Optics Systems VI*. Vol. 10703. SPIE, 2018.
- [16] Anche, R.M., et al. 2018, *Ground-based and Airborne Instrumentation for Astronomy VII*. Vol. 10702. SPIE, 2018.

Short CV



- 2014: Master in Astronomical Instrumentation, IIA, India
- 2015–2019: PhD in Astronomical Instrumentation, University of Calcutta & IIA, India
- 2019–2020: Research Engineer, NAO, Beijing, China
- 2020–2021: WALOP Postdoctoral fellow, IUCAA, Pune, India
- 2021–present: Postdoctoral Research Associate, University of Arizona, USA

General Relativity with the two Galileo satellites DORESA and MILENA

Feliciano Sapio

Department of Physics, University of Roma 'Sapienza', Piazzale Aldo Moro, 2, 00185 Roma, Italy
Istituto di Astrofisica e Planetologia Spaziali (IAPS), Via del Fosso del Cavaliere, 100, 00133 Roma, Italy

The Galileo for Science (G4S_2.0) project, funded by the Italian Space Agency (ASI), aims to perform a set of gravitational measurements with the two Galileo satellites GSAT-0201 (Doresa) and GSAT-0202 (Milena) exploiting the relatively high eccentricity of their orbits with respect to that of the other satellites of the Full Operational Capability (FOC) constellation. The elliptic orbit induces a periodic modulation of the on-board atomic clocks frequency with respect to on-ground clocks, the so-called gravitational redshift (GRS). These two satellites have already been used in 2018 by SYRTE [1] and ZARM [2] for a new measurement of the GRS that has improved the previous measurement by Gravity Probe-A [3]. GRS, which is a local position-invariance test, is only one among the predictions of General Relativity (GR) that can be tested with the Galileo constellation. In particular, the main G4S_2.0 goals include, in addition to a new measurement of the GRS, the measurements of the main relativistic precessions of the orbits. Three Italian research institutes are involved: the Center for Space Geodesy (CGS-ASI) in Matera, Istituto di Astrofisica e Planetologia Spaziali (IAPS-INAF) in Roma and Politecnico di Torino (POLITO).

Mathematical framework

The physical-mathematical context on which G4S_2.0 is set up is the one of GR, in the Weak Field and Slow-Motion Limit. This linear approximation can be applied in the case of the Earth as its gravitational field is weak^{§§} and its rotation is not relativistic. In this regime, the metric tensor of spacetime $g_{\mu\nu}$ is treated as the sum of the Minkowski spacetime $\eta_{\mu\nu}$ and a small perturbation $h_{\mu\nu}$, with $|h_{\mu\nu}| \ll 1$. Defining $x^\mu = (ct, \mathbf{x})$ as the coordinates of an inertial frame, G as the gravitational constant, c as the speed of light in the vacuum, $T_{\mu\nu}$ as the stress-energy tensor and $\bar{h}_{\mu\nu} = h_{\mu\nu} - \frac{1}{2}\eta_{\mu\nu}h$ with $h = \eta^{\mu\nu}h_{\mu\nu}$, the linearized Einstein's field equations are:

$$\square \bar{h}_{\mu\nu} = -\frac{16\pi G}{c^4} T_{\mu\nu}, \quad (1)$$

after imposing the gauge condition $\bar{h}^{\mu\nu}_{;\nu} = 0$. The solution is the so-called "tensor potential" (because of the analogy of equations (1) with Maxwell equations):

$$\bar{h}_{\mu\nu} = 4\frac{G}{c^4} \int \frac{T_{\mu\nu}(ct - |\mathbf{x} - \mathbf{x}'|, \mathbf{x}')}{|\mathbf{x} - \mathbf{x}'|} d^3x' \quad (2)$$

with

$$\bar{h}^{00} = \frac{4\Phi}{c^2}, \quad \bar{h}^{0i} = -2\frac{A_i}{c^2} \quad (3)$$

where Φ is the Newtonian or gravitoelectric potential and \mathbf{A} is the gravitomagnetic vector potential in terms of the

angular momentum of the system \mathbf{J}

$$\Phi \sim \frac{GM}{|\mathbf{x}|}, \quad \mathbf{A} \sim \frac{G}{c} \frac{\mathbf{J} \times \mathbf{x}}{|\mathbf{x}|^3}. \quad (4)$$

Following this approach, we have a gravitoelectric field produced by masses, analogous to the electric field produced by charges, and a gravitomagnetic field produced by mass currents, analogous to the magnetic field produced by electric currents. These two fields are responsible for two relativistic precessions on a satellite. Given an orbiting object around a non-rotating central mass, GR predicts a precession effect on its orbit. This precession is the so-called Schwarzschild or Einstein precession [4]. If the central mass is rotating, the Lense-Thirring (LT) effect (or "frame dragging") occurs [5]. Another effect must be taken into account, which is the De Sitter precession (or geodetic precession) due to the motion of the Earth-Moon system in the Sun gravitational field [6]. The signature of these relativistic precessions is in the secular effects on the argument of pericenter ω (in the case of Einstein and LT precessions) and on the right ascension of the ascending node, Ω , which is subject to the LT and De Sitter precessions. Measuring these effects is fundamental to study possible deviations from GR as we can compare its prediction with those of alternative theories of gravitation. Moreover, relativistic precessions play a fundamental role in the field of relativistic astrophysics, as in binary systems of pulsars and in active galactic nuclei (AGN).

Implications in the field of Fundamental Physics and Cosmology

An accurate and reliable measurement of Earth gravitomagnetic field can be useful also to investigate the following issues:

- intrinsic gravitomagnetism. It describes the spacetime curvature effects related with mass-energy currents, and not simply the corresponding effects that depend on the motion of a body on a static background field;
- strong field and compact objects. Gravitomagnetism (together with magnetohydrodynamic phenomena) can explain the mechanisms at the basis of the accretion of matter around compact objects and those of acceleration of charged particles with the simultaneous emission of powerful radio jets. Indeed, the relativistic effects, produced by the gravitomagnetic field of the rotating compact object, exert a dragging of the accretion disk and the alignment of the radio jets with the spin of the compact

^{§§} $GM/Rc^2 \ll 1$, where M and R represent, respectively, Earth's mass and radius.

object [7]. Moreover, gravitomagnetism can be useful also to determine the internal structure of neutron stars. From a direct measurement of the angular momentum of a ms-pulsar and consequently of its moment of inertia, the mass-radius relationship can be derived with possible constraint on the equation of state of the neutron star [8].

- Mach's Principle. Mach's idea "inertia here arises from mass-energy there" summarizes very well the meaning of gravitomagnetism. We can interpret the Lense-Thirring effect as a weak GR formulation of the Mach's Principle. Cosmological implications of Mach's Principle are complex and still debated.
- constraints on Dark Matter (DM). Gravitomagnetism measurements can be employed to constrain the presence of DM within our Galaxy. Building a model for the metric tensor including the gravitomagnetic terms [9], it is possible to explain the observed flatness of Milky Way rotation curves.

Furthermore, the Galileo constellation can be employed as a DM detector, with a size of several thousand km, to search for DM candidates, like topological defects. This kind of study was carried out in 2017 [10] by using the GPS constellation. Now, in the G4S_2.0 project, the new challenge is to exploit the higher sensitivity of Galileo atomic clocks.

Methods

A fundamental point in our analysis is to perform an accurate Precise Orbit Determination (POD). This is the procedure for determining the orbit of a satellite with high accuracy by fitting the tracking data with a suitable set of dynamical models for the different effects (including the Non-Gravitational Perturbations (NGPs)). NGPs arise from different sources (the Sun, the Earth and the spacecraft itself) and they are the most difficult to model because of the complex shape of the Galileo satellites and their attitude law. In this context, we want to take a step forward, compared to the state of the art, in the reliability of the dynamical model used for satellites orbits. As a consequence, an enhancement of the NGPs models is required, in particular for the direct solar radiation pressure which is the main one ($\approx 10^{-7}$ m/s²). Our final goal is to build a Finite Element Model of the Galileo FOC spacecraft, as refined as possible. Then, we plan to apply a dedicated Ray-Tracing technique to take into account mutual shadowing effects and multiple reflections. This task will allow us to compute, as accurately as possible, the effect of the interaction of each surface element with the external (or even internal) radiation sources. The corresponding perturbing accelerations will be used in the POD to provide Fundamental Physics measurements

(i.e. GRS, relativistic precessions). As a first step, a 3D-CAD of the satellite has been developed as well as a Box-Wing (BW) model. The BW model simplifies the satellite structure to the central bus (box) and two rectangular solar panels (wing). The geometry and the optical properties provided by ESA's Galileo-Metadata have been used to characterize the satellite surfaces. One of our preliminary POD, in the case of the Galileo GSAT-0208 in nominal orbit, is shown in Figure(1) and compared with a corresponding POD from ESA.

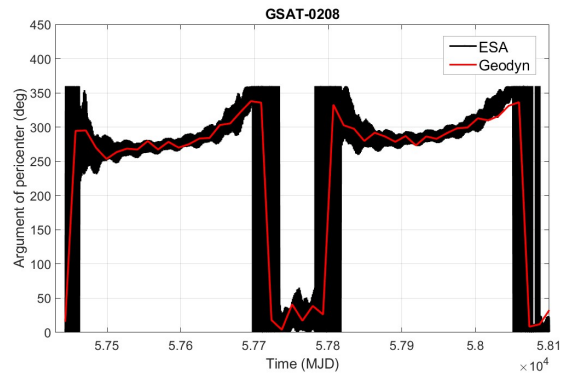


Figure 1: The plot shows our preliminary POD for the GSAT-0208 satellite in nominal orbit with the ESA POD as comparison. Our POD was performed with the software GEODYN (NASA/GSFC) by using only the satellite laser ranging data.

Conclusions

We presented the main goals of G4S_2.0 project related to Gravitation and Cosmology. Both the measurements of the GRS and of relativistic precessions are fundamental to study possible alternative theories of gravitation. Furthermore, the possible presence of DM in the form of topological defects would constitute a significant result in Cosmology. These measurements can be obtained by exploiting, mainly, two Galileo satellites on elliptical orbits and by enhancing the dynamical model at the basis of the POD, improving the NGPs effects estimates.

References

- [1] Delva, P., et al. 2018, in Phys. Rev. Lett., 121, 231101.
- [2] Herrmann, S., et al. 2018, in Phys. Rev. Lett., 121, 231102.
- [3] Vessot, R. F. C., et al. 1980, in Phys. Rev. Lett., 45, 2081.
- [4] Einstein, A., 1916, in Ann. Phys., 354, 769.
- [5] Lense, J., & Thirring, H., 1918, in Zeit. Phys., 19, 156.
- [6] De Sitter, W., 1916, in Mon. Not. R. Astron. Soc., 76, 699.
- [7] Thorne, K. S., et al. 1988, in Near Zero: New Frontiers of Physics, 573-586.
- [8] Kramer, M., et al. 2006, in Science, 314, 97-102.
- [9] Crosta, M., et al. 2020, in Mon. Not. R. Astron. Soc., 496, 2, 2107-2122.
- [10] Roberts, B. M., et al. 2017, in Nat. Commun., 8, 1195.

Short CV



2018: BSc in Physics, Naples University Federico II, Italy
 2020: MSc in Physics-Astrophysics, Naples University Federico II, Italy
 2020–present: PhD student in Astronomy, Astrophysics and Space Science, Rome University Sapienza & Istituto di Astrofisica e Planetologia Spaziali (IAPS-INAF), Rome, Italy

GW Vir instability strip in the light of new observations of PG 1159 stars

Paulina Sowicka

Nicolaus Copernicus Astronomical Center, Polish Academy of Sciences, ul. Bartycka 18, PL-00-716, Warszawa, Poland

White dwarfs, stars at the latest stages of evolution of low- to intermediate-mass stars, show a diversity of pulsation properties. There are three classical groups of white dwarf pulsators along the white dwarf cooling track: H-deficient GW Vir pre-white dwarf stars, He-rich DBVs, and H-rich DAVs [see e.g., 1]. GW Vir stars lie in the first instability strip entered by a post-asymptotic giant branch (AGB) star. White dwarf stars residing in the GW Vir domain span a large range of effective temperatures (≈ 75 -250 kK) and surface gravities ($\log g \approx 5.5$ -8). Most GW Vir pulsators are of the PG 1159 spectral type but there are also [WC]-types (central stars of planetary nebulae with Wolf-Rayet spectra of carbon sequence). The main spectral feature of the PG 1159 class is the absorption trough made up by the He II $\lambda 4686 \text{ \AA}$ and adjacent C IV lines. PG 1159 stars exhibit He-, C-, and O-rich surface abundances with strong variations of the He/C/O ratio from star to star and, in some cases, traces of heavier elements.

Some stars show photometrically detectable low-amplitude, multiperiodic pulsations with periods as short as a few minutes, that are due to nonradial gravity modes driven by the κ mechanism associated with the partial ionization of the K-shell electrons of carbon and/or oxygen in the envelope [2, 3]. A theoretically predicted ϵ mechanism, that is connected with the changes in the nuclear energy generation rate in the stars with He burning shells, was also proposed as an additional mechanism responsible for the highest frequency modes. In theoretical calculations both mechanisms form overlapping regions in the H-R diagram but despite a number of stars lying in this region, the ϵ mechanism has still not been observed to operate in any star [4].

PG 1159 stars are thought to be formed as a result of a “born-again” episode - a very late thermal pulse (VLTP) experienced by a hot white dwarf during its early cooling phase or a late thermal pulse (LTP) that occurs during the post-AGB evolution when H-burning is still active [e.g., 5]. This evolutionary history is reflected in their chemical abundances; especially elements like H and N are imprints of the prior evolution as they are tracers of when the progenitor experienced the final thermal pulse. That makes these stars important to study from the evolutionary point of view, as they are supposed to be the main progenitors of H-deficient white dwarf stars.

The impurity of GW Vir instability strip

The striking difference between the GW Vir instability strip and the domains of DBVs and DAVs is that the GW Vir one is not pure, i.e. not all stars in that section of the H-R diagram show pulsations, in contrast to the two others. Thus their interiors that can be studied using aster-

oseismology do not necessarily represent the interiors of all PG 1159 stars. According to the literature, only about 50% of them pulsate [6]. Why is that the case? What separates the pulsators from the nonpulsators?

The role of nitrogen

The existence of both pulsating and nonpulsating stars within the GW Vir instability strip was a real challenge to pulsation theory. Firstly, a nitrogen dichotomy was observed, meaning that all N-rich (about 1% in mass) stars are pulsators, whereas N-poor (below 0.01% in mass) stars are all nonpulsators. Therefore the hypothesis was put forward that nitrogen, despite its rather small abundance even in N-rich stars, is essential for pulsation driving [7]. On the other hand, [8] argued that predominantly a high oxygen abundance is responsible for that. The whole picture is complicated by the variety of surface abundances in PG 1159 stars (basically each star has its own unique composition), the role of metallicity, and the admixture of helium “poisoning” the development of pulsations [6]. That was until the calculations showed that only the stars with the most oxygen and carbon (depending on their configuration) can pulsate, and a pulsator and nonpulsator with the same carbon and oxygen abundance, but different amount of nitrogen, were studied, confirming the first findings [9].

The final piece to the puzzle

The part played by nitrogen as a tracer of the previous evolutionary history is therefore interesting in this context. Is N essential for pulsation driving? Are there surface patterns that are indicative of driving? Is a VLTP a necessity for destabilizing a star to develop pulsations? If yes, this would allow the important conclusion that the GW Vir stars have a fundamentally different evolutionary history than the non-pulsators. However, the only culprit in this view of the excitation theory and abundance patterns of these stars remained - PG 1144+005, the only known N-rich PG 1159 star that was not previously shown to pulsate.

A number of authors observed PG 1144+005 in search for the elusive pulsations. Starting with the pioneering work of Grauer and collaborators in the 1980’s, through more recent and extensive studies by Schuh and Steiner and collaborators, none of their efforts bore fruit. Only the latter [10] provided observational data and detection threshold. Their data showed a light curve with no visible variability and a semi-amplitude of about 0.02 mag. The lack of variability was then reflected in the Fourier amplitude spectrum, where no peak exceeded an amplitude of 4 mmag. We revisited the object and observed it in 2018 with the 10-m GTC telescope to de-

tect photometric variability in 1.1 hr of observations with a semi-amplitude of about 5 mmag and preliminary pulsation frequencies in the range $\approx 80\text{--}120$ [d⁻¹]. This was confirmed in 2021 with a follow-up observing run with the 1-m Lesedi telescope. Fourier amplitude spectra of five nights of observations showed four main groups of pulsation modes with varying amplitudes over the course of the observing run. Highly variable amplitudes and/or frequencies, and even a complete disappearance of the pulsations for a period of time are often observed in GW Vir stars. The detected frequencies were consistent with g-mode pulsations excited by the κ mechanism operating in PG 1159 stars. [11].

This provided the final piece of evidence that there is a clear separation, namely all known N-rich PG 1159 stars pulsate and the N-poor ones do not. The important conclusion follows: the pulsating and non-pulsating PG 1159 stars have different evolutionary history, and it seems necessary that a star undergoes a VLTP to develop pulsations, while nitrogen is a tracer of this evolutionary history. Does it mean that the picture is now complete? Or will we find more N-rich nonpulsators and N-poor pulsators if we push the detection limit down to further challenge the current theory?

The search for more

Even though the evolutionary link to the nitrogen abundance appears to hold, it is based on a small sample of objects for which we have full information. Out of 58 known PG 1159 stars, only 15 have their nitrogen abundance assessed, still statistically a small number considering the total number of known PG 1159 stars. A detailed assessment of elemental abundances for a large sample of these stars is therefore highly demanded.

Because the information about variability is available for only a handful of PG 1159 stars, we carry out a survey for variability with a set of telescopes of different sizes ranging from 1-m to 10-m, to cover both the brightest and faintest targets with good temporal resolution in at least 1-hr long observing blocks (Sowicka et al. 2022, in prep.). The goal is to discover new pulsators, especially among those not checked for variability, and re-observe known nonpulsating PG 1159 stars to improve the previous detection limits for non-variability. Figure 1 shows exemplary 30 amplitude spectra from the survey. What is evident even among this sample is that the majority of those stars don't show variability even with a lower detection threshold. The true pulsator occurrence in the GW Vir instability strip might therefore be lower than the previously reported 50%.

Take away points

Pulsators and nonpulsators can be found within the

boundaries of GW Vir instability strip - the true fraction might be even lower than previously reported 50%. This discrepancy has been explained by different evolutionary histories of pre-white dwarf progenitors in the AGB phase, then reflected in the surface abundance with nitrogen and hydrogen being the trace elements. With the discovery of pulsations in the only remaining N-rich PG 1159 star, PG 1144+005, we provided the last missing piece to the current theory. We also proved that it is worth re-observing known non-pulsating PG 1159 stars with better detection thresholds together with those never photometrically checked. For a complete picture spectroscopic observations aiming at deriving surface abundances of all crucial elements including nitrogen are needed. Our ultimate goal is to obtain the first statistically significant sample of well-studied PG 1159 stars with information on their evolutionary history and excitation of pulsations.

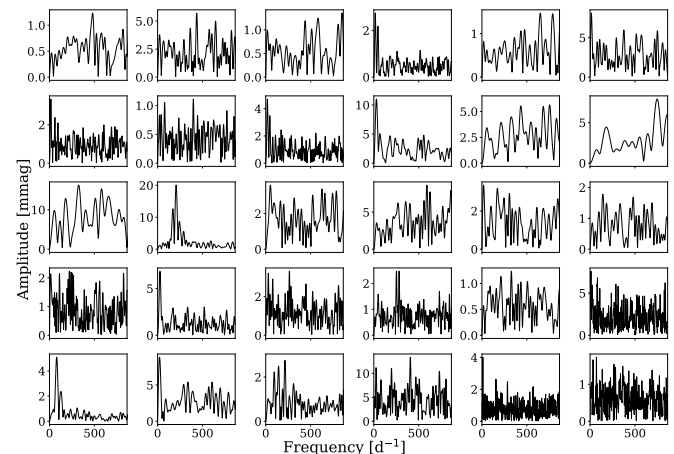


Figure 1: Exemplary amplitude spectra from our survey for variability in PG 1159 stars. One previously known pulsator (middle row 2nd from the left), PG 1144+005 (bottom row 1st from the left), and a candidate that still needs confirmation (2nd row from the bottom, 4th from the left).

References

- [1] Winget, D. E., & Kepler, S. O. 2008, *ARA&A*, 46, 157
- [2] Starrfield, S. G., et al. 1983, *ApJL*, 268, L27
- [3] Starrfield, S., et al. 1984, *ApJ*, 281, 800
- [4] Sowicka, P., et al. 2018, *MNRAS*, 479, 2476
- [5] Miller Bertolami, M. M., & Althaus, L. G. 2006, *A&A*, 454, 845
- [6] Quirion, P.-O., et al. 2004, *ApJ*, 610, 436
- [7] Dreizler, S., & Heber, U. 1998, *A&A*, 334, 618
- [8] Quirion, P.-O., et al. 2007, *ApJS*, 171, 219
- [9] Werner, K., & Rauch, T. 2014, *A&A*, 569, A99
- [10] Steininger, B., et al. 2003, *Interplay of Periodic, Cyclic and Stochastic Variability in Selected Areas of the H-R Diagram*, 292, 237
- [11] Sowicka, P., et al. 2021, *ApJL*, 918, L1

Short CV



2008–2012: BSc in Astronomy, Jagiellonian University, Cracow, Poland
 2012–2014: MSc in Astronomy, Jagiellonian University, Cracow, Poland
 2015–2016: Student Support Astronomer, ING, La Palma, Spain
 2014–present: PhD in Astronomy, NCAC of the PAS, Warsaw, Poland

Hypatia

Wikipedia

Hypatia (born c. 350–370; died 415 AD) was a Greek Neoplatonist philosopher, astronomer, and mathematician, who lived in Alexandria, Egypt, then part of the Eastern Roman Empire. She was a prominent thinker of the Neoplatonic school in Alexandria where she taught philosophy and astronomy. Although preceded by Pandrosion, another Alexandrine female mathematician, she is the first female mathematician whose life is reasonably well recorded. Hypatia was renowned in her own lifetime as a great teacher and a wise counselor. She wrote a commentary on Diophantus's thirteen-volume *Arithmetica*, which may survive in part, having been interpolated into Diophantus's original text, and another commentary on Apollonius of Perga's treatise on conic sections, which has not survived. Many modern scholars also believe that Hypatia may have edited the surviving text of Ptolemy's *Almagest*, based on the title of her father Theon's commentary on Book III of the *Almagest*.

Hypatia constructed astrolabes and hydrometers, but did not invent either of these, which were both in use long before she was born. Although she herself was a pagan, she was tolerant towards Christians and taught many Christian students, including Synesius, the future bishop of Ptolemais. Ancient sources record that Hypatia was widely beloved by pagans and Christians alike and that she established great influence with the political elite in Alexandria. Towards the end of her life, Hypatia advised Orestes, the Roman prefect of Alexandria, who was in the midst of a political feud with Cyril, the bishop of Alexandria. Rumors spread accusing her of preventing Orestes from reconciling with Cyril and, in March 415 AD, she was murdered by a mob of Christians led by a lector named Peter.

Hypatia's murder shocked the empire and transformed her into a "martyr for philosophy". [Around the end of the nineteenth century,] European philosophers and scientists described Hypatia as the last representative of science and free inquiry before a "long medieval decline". In the twentieth century, Hypatia became seen as an icon for women's rights and a precursor to the feminist movement.



Figure 1: This fictional portrait of Hypatia by Jules Maurice Gaspard, originally the illustration for Elbert Hubbard's 1908 fictional biography, has now become, by far, the most iconic and widely reproduced image of her.

Hypatia was honored as an astronomer when 238 Hypatia, a main belt asteroid discovered in 1884, was named for her. The lunar crater Hypatia was also named for her, in addition to craters named for her father Theon. The 180 km Rimae Hypatia are located north of the crater, one degree south of the equator, along the *Mare Tranquillitatis*.

